Dynamics of the Formation of Rings of Protein Filaments

Pablo González de Prado Salas

Supervisor: Pedro Tarazona Lafarga

Universidad Autónoma de Madrid

September 2014

Para Anita

Acknowledgements

First of all I have to express my most sincere gratitude to my advisor, Pedro Tarazona, for always having time for me during the easy and difficult times.

Biophysics is nothing without biology, so I have to thank Marisela Vélez and her students for their hard work. Without them, our models could not be always one step behind.

I want to thank Teresa and Pau, for their valuable discussions on whether the Romans or the Greeks were cooler. Obviously the Romans though. Then again... but I digress. I would like to extend my gratitude to the rest of my office colleagues; there have been quite a lot of them over the years! Special thanks to Teresa, for being my guiding spirit in academia.

I do not know most of the people in my department half as well as I should, but they have all been an important part of my PhD experience, so I thank them for that, and for the many times they have helped me in different ways.

I cannot forget about my friends from physics, for we walk the same path together.

I fear I may be kicked out of my thesis manuscript like Almodóvar from The Oscars ceremony (1999), but I have to give special thanks to my many friends from Antares Astronomy club, because there is more to academia than research. I hope Friday's Games Evening—the single most brilliant idea from my PhD—will live on for many years.

Special appreciation to my family and childhood friends. Though space and time may drift us apart you are still at the core of my life.

My most sincere thanks to those I have forgotten to mention.

And finally, a big thank you for Ana ~~because she asked me to include her here~~; she does not need words to know why.

Contents

1 Presentación **6**

2 A brief introduction to FtsZ **8**

2.1 FtsZ 8

2.2 Force generation mechanisms 10

3 Fine-grained modelling of FtsZ filaments on a flat substrate **15**

3.1 The model 15

3.2 Strong Lateral Bond 18

3.2.1 Straight aggregates 22

3.2.2 More aggregates with SLB 24

3.2.3 Relevance of the initial state 27

3.2.4 Some remarks on the SLB study 30

4 A dynamic model for comparison with FRET experiments **32**

4.1 Square-lattice model 33

4.2 Simulations 38

4.2.1 Evolution of filament rings 44

4.3 Discusion 46

5 Effects of torsion in single FtsZ filaments **48**

5.1 Analytical study of filaments with anchoring and torsion 50

5.2 MD and ideal filaments 55

5.2.1 Filaments on a surface: mathematical description 63

5.2.2 Simulations 70

5.2.3 Experimental contrast 75

5.2.4 Discussion 77

6 Collective effects of torsion in FtsZ filaments **81**

6.1 Fine-grained model with torsion-I: simulations for open and closed filaments 81

6.1.1 Single filament simulations 82

6.2 Fine-grained model with torsion-II 91

6.2.1 First results—the question of the torsion potential 95

6.3 Some remarks on torsion and anchoring 106

7 Lipid-lipid interaction **110**

7.1 Fine-grained model with lipid-lipid interaction 111

7.1.1 Phase separation in a mixed lipid bilayer 114

7.1.2 Collective behaviour of the system with protein-lipid interaction 116

7.1.3 Protein filaments in presence of small lipid domains, relaxation and memory effects 119

7.1.4 Who is leading whom? 123

7.1.5 Discussion 128

8 Overview and conclusions **131**

9 Conclusiones **135**

1

Presentación

This short overview of the thesis work is written in Spanish as required by the Spanish Government for thesis manuscripts in a foreign language.

FtsZ fue la primera proteína que se identificó como parte del citoesqueleto en procariotas. Desde su descubrimiento su papel en la vida celular ha estado ligado a la división, un proceso evidentemente esencial que aún estamos lejos de comprender. En células eucariotas la división está asistida por motores moleculares que «tiran» de filamentos de proteínas para conseguir fuerzas de constricción. Sin embargo en procariotas no se han identificado este tipo de motores moleculares en relación a la división. ¿De dónde procede pues la fuerza necesaria para el proceso? Ésta es aún una cuestión abierta sobre la que no hay más que débiles conjeturas.

Las células procariotas son en promedio mucho más pequeñas que las eucariotas, lo que dificulta los trabajos experimentales en células vivas. Para complicar más las cosas, FtsZ no es la única responsable del proceso de división, sino que es parte de un gran complejo de proteínas y moléculas que colaboran en una delicada orquestación cuyos detalles aún son un misterio.

La filosofía que motiva este trabajo es la de acercarse a este tipo de situaciones complejas a través de la simplificación. En primer lugar, el grupo experimental liderado por la profesora Marisela Vélez comenzó a realizar estudios de microscopía de fuerzas con FtsZ aislada. De este modo es imposible responder a todas las preguntas relacionadas con la división de células vivas, pero se puede conseguir información más clara y fiable sobre FtsZ en diferentes condiciones.

Este conocimiento puede ser después extrapolado a situaciones más complejas que no son fáciles de interpretar mediante aproximaciones clásicas.

Sin embargo, ni siquiera estos experimentos con FtsZ aislada resultan triviales de interpretar. FtsZ es una proteína relativamente sencilla, no obstante, las interacciones colectivas de cientos o miles de ellas y el sustrato de trabajo pueden resultar en comportamientos complejos que exigen nuevas herramientas para su estudio. Este es el problema al que se ha enfrentado el profesor Pedro Tarazona junto a sus estudiantes y colaboradores. La principal herramienta—pero no la única—utilizada en este trabajo ha sido la simulación de modelos de red con dinámica de Montecarlo. En estos modelos se intenta incluir la mínima información estructural y el mínimo detalle en las interacciones como sea posible. Esto no es por falta de información, sino un nuevo ejemplo de la filosofía de trabajo a través de la simplificación.

El objeto es diseñar un sistema tan sencillo como sea posible que, sin embargo, sea capaz de explicar los resultados experimentales. De esta forma, los detalles que no se hayan podido eliminar del modelo serán de forma lógica los elementos verdaderamente esenciales del problema. Cualquier detalle que haya quedado fuera será no esencial al nivel de precisión con el que se esté describiendo el problema. Y precisamente esto, identificar qué fenómenos son los que de verdad caracterizan el problema, tiene un gran valor si queremos ser capaces de comprender el sistema global, y ese es el principal objetivo del trabajo recogido en esta memoria.

2

A brief introduction to FtsZ

2.1 FtsZ

FtsZ is a protein found in nearly all prokaryotes. Its name stands for *Filamenting temperature-sensitive mutant Z* and it plays a key role in cell division, although the details of the process remain unknown. Despite emphasis often being made on bacteria, FtsZ also occurs in archaea [2] and, interestingly, it has also been found in chloroplasts and even in some mitochondria [3, 4, 5], which could be expected since these organelles are believed to have a prokaryotic origin.

The cytoskeleton is a complex of proteins responsible for much of the shape and structure of a cell, and it is also essential in the division of the cell. Before the decade of 1990 there was no direct proof that prokaryotic cells had cytoskeleton at all, FtsZ being its first protein to be identified. Therefore, bacterial division

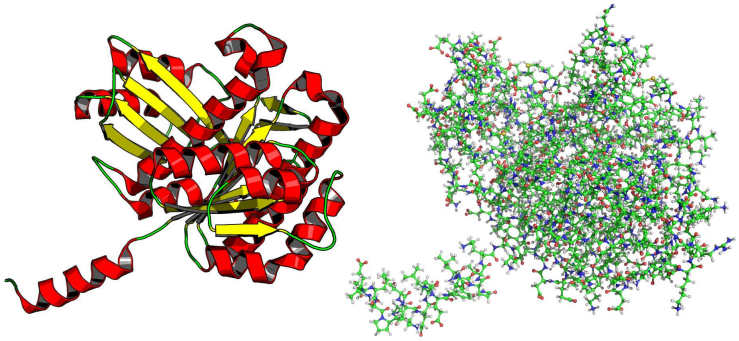

Figure 2.1: FtsZ secondary structure and atomic distribution [1].

is still a rather young field, where early hypotheses are yet to be proved right or wrong.

There are three main kinds of filaments in the eukaryotic cytoskeleton: microfilaments (actin filaments), intermediate filaments and microtubules (made of tubulin). The first prokaryotic homologue to actin to be discovered was MreB, which is found in all non-spherical bacteria, being involved in shape and structure maintenance. FtsZ, according to sequence, is an old homologue to tubulin, nevertheless, its role in cellular division is nearer to that of actin in eukaryotic cells, as will be explained later. So far there is only one homologue for intermediate filaments known in prokaryotes; crescentine. However, it is exclusive to *Caulobacter crecentus*, and this is suspected to be due to a case of recent horizontal gene transfer [6].

FtsZ monomers use the nucleotid GTP to bind head-to-tail and form protein filaments. Like in tubulin bonds, the resulting bond has GTP-ase activity, in fact, the catalytic site is the most similar region between tubulin and FtsZ proteins. However, the differences between tubulin and FtsZ are important. For example, the basic FtsZ subunit is a protein monomer, whereas in the case of tubulin it is an α and β tubulin dimer. On top of that, FtsZ is known to need the membrane for its biological function, while tubulin works in the cytoplasm. For these and other reasons, the interesting analogy between FtsZ and tubulin must be taken with caution [7].

The GDP mediated FtsZ bond is weaker than the GTP bond, and it is debated whether there are significant differences in the flexibility or bending angles of the two bonds. These filaments are strong enough to form aggregates, but weak enough to be dynamic. They are a good example of what in soft-matter physics is known as *living polymers*. The main function of the FtsZ filaments is to form the Z-ring. This structure assembles at the center of the cell and is essential for the production of a constriction force that will allow the cell to divide in two daughter cells.

FtsZ filaments cannot attach to the membrane by themselves. Attachment is mediated by either FtsA or ZipA proteins, both of which are needed for division [8]. It is important to note that in either case the link is quite flexible and well conserved [9, 10].

It has been mentioned that the Z-ring forms in the center of the cell. Of course, this will not happen by chance, so a regulatory system is required: the Min complex. This complex is formed by a family of proteins which prevent the

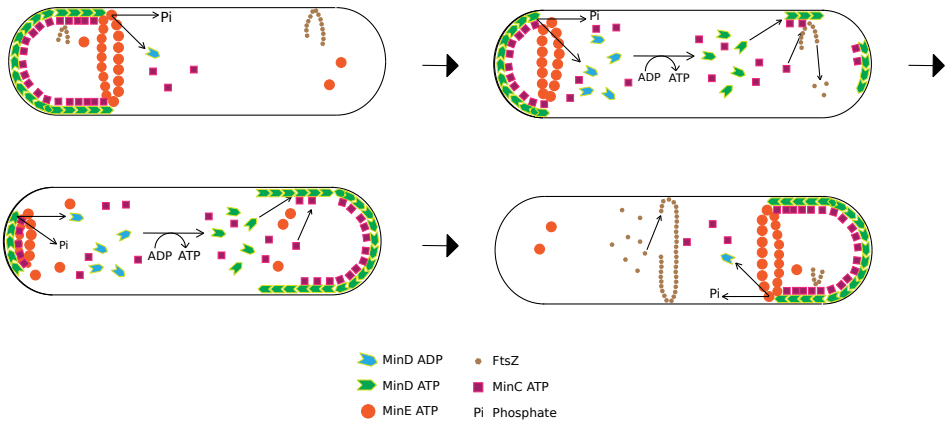

Figure 2.2: Schematic representation of the regulatory Min system (Wikipedia Commons, edited).

formation of the Z-ring near the cell poles. In Figure 2.2 we have an schematic representation of this regulation process: first, MinD attaches to the membrane and recruits FtsZ-inhibitor MinC. The last step is the arrival of MinE, which disrupts MinDC complexes. This interaction results in waves of the Min system, with MinDC "running away" from MinE, as observed *in vitro* [11]. In bacteria, where the waves cannot propagate without bounds, an oscillating behaviour arises [12]. These oscillations occur along the longer axis of the structure. (This means that, in a rectangle, they would take place along the diagonal.) On average, the middle of the cell is the place where MinC is less likely to be found, so FtsZ anchors there.

2.2 Force generation mechanisms

FtsZ is perhaps the most important protein in the Z-ring complex [14], which is necessary to create the constriction force needed for division. But how is this force exactly generated? In animal cells the process of division (cytokinesis) is well understood. Much bigger than prokaryotes, the process is visible with a light microscope. During the anaphase a ring of actin filaments and myosin II assembles in the middle of the cell and will progressively contract forming the cleavage furrow until the daughter cells are fully separated. The force required for the process is obtained via the molecular motor myosin II, which uses ATP hydrolysis energy to "walk" along the actin filaments, bringing them together and thus narrowing the cleavage furrow.

In contrast to the previous process, no molecular motors have been identified in relation to the Z-ring and prokaryotic division. What is more, experiments found that division in *E. coli* was possible introducing FtsZ from *Mycoplasma pulmonis* and *Bacillus subtilis*, quite divergent from *E. coli* FstZ and thus unlikely to interact with *E. coli*'s molecular motors should it have any [15]. In addition, *in vitro* experiments in liposomes have found that FtsZ alone (with FtsA as a linker) is capable of producing some deformation—although no complete division [16]. However, if we interpret this as the filaments adapting the surface to their natural curvature, then the force will stop at that point and a new source of constriction force is needed.

As research progresses the picture gets more complicated, with new agents and seemingly contradictory data, for example, Söderström et al. have presented evidence that FtsZ dissociates from the Z-ring complex before division is complete. This evidence is not definitive, for instance, it could be that, because the ring decreases in size as division progresses and part of the FtsZ is incorporated to the cytoplasm, FtsZ scapes detection while still being present through the process. This fact might even favour some hypotheses—as will be explained below, if the curvature of FtsZ filaments is the origin of the constriction force, this would be a problem for diameters with greater curvature during the end of division. Be it as it may, we need to consider the fact that other proteins and factors will probably be as important as FtsZ during cell division, and that it is unlikely that we will ever identify a simple, unique explanation for the constriction force mechanism. Bearing that in mind, we will try to sum up the main hypotheses which are currently being discussed as the origin of this force.

Hydrolysis

This was a natural hypothesis given the parallelism with tubuline, where GTP hydrolysis is key to its dynamics. The idea is that GTP-bond FtsZ filaments with small curvature will form the Z-ring. Subsequently the bonds will hydrolyse and increase their curvature, thus producing the constriction force. Since hydrolysis is consuming energy during the delicate process of cellular division and this catalytitc property is conserved through all FtsZ proteins, it is also natural to assume that hydrolysis is playing an important role.

The main drawback to this model is the lack of solid experimental evidence. Experimental results related to bending angles and hydrolysis are far from con-

sistent, and different crystal structures yield different results. Packing effects could have an impact on bending and twist angles in crystal protofilaments as well. Significantly, even research groups that strongly defend this hypothesis find contradictory results, like GDP bonds stabilizing in a closed (straight) state [17], GDP-bond crystals for straight protofilaments or an energy potential for the GTP bond clearly showing a preference for a curved state, very closemathnormallue for GDP [18].

In some cases division has been observed to take place with impaired GTPase activity [19, 20]. The process was faulty, but it suggests the force generating mechanism cannot fully depend on GPTase activity to take place. In addition, Erikson and Osawa observed in a recent article [21] the formation of the Z-ring and initial constriction in the absence of hydrolysis. They conclude that hydrolysis cannot be responsible for at least most of the constriction force, and speculate that, instead, it could be essential for allowing monomer turnover and a dynamic Z-ring which would "freeze" otherwise.

This hypothesis should also address the fact that the experimental GDP/GTP ratio has been measured from zero to 50%, perhaps too low should hydrolysis be indeed the force generating mechanism in prokaryotic division.

However, the lack of strong data also means it is too soon to discard the hypothesis. Even if some experiments suggest hydrolysis cannot be the main source of constriction force, they could turn out to be wrong or incomplete. All elements considered, hydrolysis could be an important or even necessary contribution in the complete process.

Lateral contacts

This hypothesis assumes some weaker, unspecific lateral interaction between FtsZ monomers. This interaction would help small filaments to gather in bundles as seen experimentally and perhaps stabilize the Z-ring itself. There is strong evidence that this lateral interaction does indeed exist [22]. The hypothesis claims that filaments will slide along each other in order to maximize the number of this lateral interactions, which are individually weak but summed along the length of the filaments should be very representative. The effect of this reptation of the filaments is a tightening of the Z-ring, which implies a constriction force [22, 23].

One problem this hypothesis has to face is the event of having a set of nearly perfect protein rings with few to no gaps after packing driven by the maximization

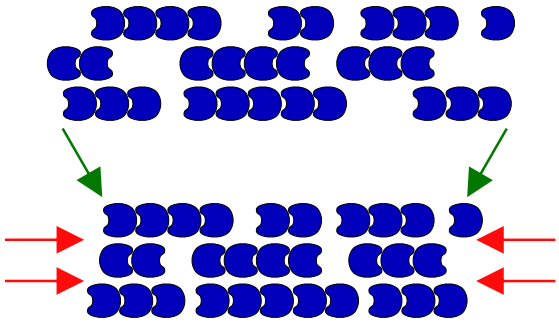

Figure 2.3: Schematic representation of the force generation mechanism driven by the maximization of lateral contacts.

of lateral contacts. If the filaments adopt an spiral configuration rather than a set of rings the problem would banish [22]. Alternatively, the filaments could prove too weak to form complete rings, specially after hydrolysis, which would also explain the value of GTP hydrolysis in the division process [21].

Even if this lateral contact maximization effect exists, it could turn out to be too weak to be fully responsible for the constriction force mechanism, nevertheless, there is no reason why there should be one unique source for this force.

Filament curvature

According to this hypothesis, FtsZ filaments have a natural curvature, either with a GTP mediated bond or with GDP. If this curvature is higher than that of the cellular membrane, then the filaments will try to bend the surface as they attach there. This hypothesis is rather simple, but it also has its difficulties:

In the first place, bending should stop once the membrane matches the natural curvature of the filament, and another mechanism is needed to complete the division.

There is also the question of the role of hydrolysis if it is not to create a constriction force. A plausible alternative, already mentioned above, was given by Osawa and Erikson [21], who propose the role of hydrolysis is to create gaps that will prevent constriction to stall.

Although this problem is seldom mentioned in the literature, it is important to explain why the filaments will try to attach to the membrane with their natural curvature perpendicular with respect to the surface, specially considering the fact that anchoring is rather flexible [9, 10]. If the filaments do have a higher

curvature than the membrane and, as it seems, they attach to it in a flexible way, it would be natural to expect small rings to form on the membrane instead of having filaments trying to bend the membrane until it matches their natural curvature.

3

Fine-grained modelling of FtsZ filaments on a flat substrate

As has just been described in the previous chapter, FtsZ driven division is a complex process. Even the largely simplified experiments of FtsZ filaments on a mica surface are too complex to understand by direct inspection. However, it is a setup where the statistical physics perspective can be useful. The relatively simple interactions between monomers are amplified through the collective behaviour of the system, resulting in the complex structures that can be observed. This process can be modeled in an attempt to identify the essential interactions that are governing the process. This approach allows to roughly explore the interactions between monomers using images where individual filaments—let alone monomers—are slightly under the resolution available.

It was this idea that motivated this study by Páez et al. [22]. Since most of the work in this dissertation is the natural continuation to the article by Páez et al., we shall explain it to some detail.

3.1 The model

The model considers a triangular, periodic, fine-grained lattice. FtsZ proteins can be at any lattice point, but they will exclude an area around them: that will represent the true size of the monomer, bigger than each lattice point to allow for fine movement of the proteins—for this reason it is called a fine-grained lattice model. Around this excluded circle there is a crown of sites where the protein

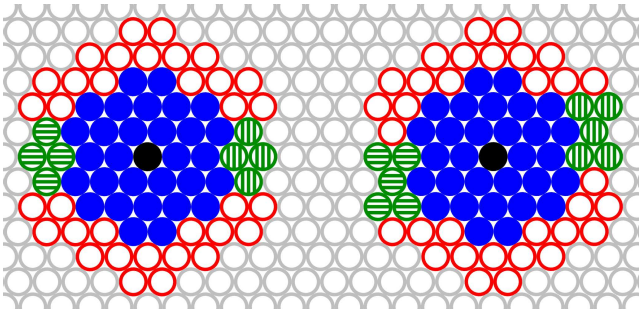

Figure 3.1: Triangular lattice used in [22]. It represents a small area of the lattice, with two monomers centered at the black circles, with orientation 0° and 15° respectively. The different areas of influence of the monomers are also shown: blue for the excluded area, red for the crown where lateral contacts are possible and green for the areas where longitudinal bonds are allowed.

will weakly interact with any other protein. This is the lateral interaction U_a that promotes filament condensation. Each protein on the lattice has an orientation, and for every different orientation there is a subset of points in the interaction crown where the protein can form strong longitudinal bonds with proteins of similar orientation.

This model considers 24 possible orientations with a 15° interval. If the second protein in the longitudinal bond has the same orientation as the first, then the energy of the bond is U_b. In order to have curved filaments (as opposed to noise in the direction of the filament) there are different energy penalties for longitudinal bonds with curvature: if the orientation of the second monomer is the same as that of the first +15° (counterclockwise) then the energy is $U_b - U_-$, ($U_- < 0$), but if the angle is the same –15°, then the energy will be $U_b - U_+$, ($U_+ > 0$), where $U_b - U_+$is usually taken to be $0\,k_BT$ or at least much weaker than $U_b - U_-$. Having $U_b - U_+ = U_b - U_-$ will produce filaments with no net curvature.

A standard Monte Carlo procedure is used for the dynamics of the model. A proteins is chosen at random and some change (random as well) in their position or orientation is attempted. Acceptance of such events is decided using the Metropolis algorithm—acceptance is proportional to the exponential of the energy change involved, which implies that every process energetically favourable is automatically accepted, and that the rest still have a chance.

It is important to realize the fact that this model allows for the movement and turning of monomers without having to break longitudinal bonds.

Figure 3.2 shows how every interaction included in the model is truly essential in order to reproduce the AFM images on mica, and also that for those experi-

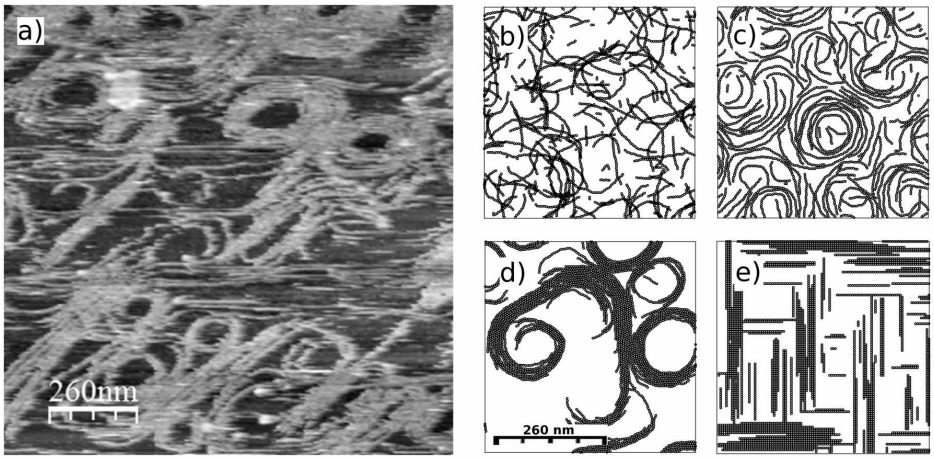

Figure 3.2: Figure 3 from reference [22]: "The AFM image (a) is compared with [...] MC simulations of the fine-grained lattice model with incomplete sets of interaction effects. Panel (b) shows filaments formed when the simulation does not include lateral interactions nor excluded volume effects (i.e. isodesmic ideal polymers). Panel (c) comes from a simulation without lateral interactions ($\beta U_a = 0$), to be compared with the snapshot in panel (d) using the complete set of model interactions. Panel (e) corresponds to the coarser square-lattice model presented by Lan et al. [23] at the same protein coverage of a planar surface as in all the other panels".

mental circumstances no extra interactions are required. In snapshot (b) there are neither lateral interactions nor excluded volume. The resulting filaments look nothing like the experimental images. In (c) excluded volume is recovered, and the results clearly improve. However, lateral interactions are needed to promote aggregation of the filaments (d). It is interesting to note that this interaction is quite weak (~1kT) when compared with the longitudinal bond—of the order of 10kT. This explains why the effect may not be evident using other experimental approaches. Finally, snapshot (e) shows a model with no curvature of the filaments, which does not provide enough detail in this context.

Depending on the parameters there will be three basic types of structures; **I**, **C** and **O** aggregates (see fig 3.3). **I** clusters are 2D nematic drops where the filaments align their long sides to form a rectangle. Having longer filaments takes advantage of the longitudinal bond, but in a stretched rectangle there will be fewer lateral interactions, so an equilibrium is reached. In a **C** aggregate the filaments can have curvature, which is advantageous from the energetic point of view. The trade-off is having to align the filaments, which can have any head-to-tail orientation in an **I** aggregate. Therefore, the energetic gain comes at a cost in entropy. Finally, an **O**

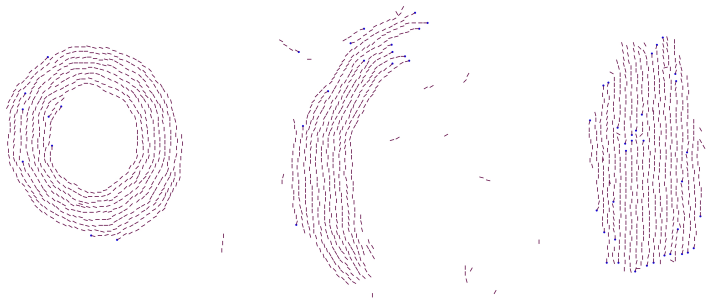

Figure 3.3: Basic **I**, **C**, **O** structures found with the fine-grained lattice model.

aggregate will further exploit longitudinal bonds, at the cost of having to force the ideal curvature of the filaments.

Experimental images show complex structures which can be understood as the interaction of these basic structures. Interestingly, only over a narrow region of the parametric space do these structures have similar free energies, so they can coexist. This fact was used to perform a coarse fit of the model parameters ($\beta U_b \simeq \beta U_+ \sim 10$, $\beta U_a \sim 0,5$, $\beta U_- \sim 0,5$).

3.2 Strong Lateral Bond

The introduction of a strong lateral bond (SLB) was motivated by new experiments on a different substrate. Instead of attaching the protein directly over a mica surface, a lipid bilayer was used this time. The experimental results show the importance of the intrinsic properties of the membrane—different mixes of phospholipids with different polarity result in different aggregates. The details of the anchoring of the monomers to the membrane also have a direct impact on the structures that arise. In this case we are interested in a new experimental approach: instead of attaching the protein with no control over the relative orientation with respect to the substrate as was the case of the mica experiments or, to a point, with the loose link provided by ZipA and FtsA, FtsZ mutants will be used. These mutants are designed to have a cysteine in some specific position of the molecule. It is with this reactive cysteine that the protein will strongly attach to the surface. Because we know the exact position of this amino acid, we also know the orientation of the protein with respect to the membrane. Cys2 mutant has a cysteine close to the amino terminal domain while for Cys255 it is near the carboxy domain, so they are approximately 180° degrees from each other. In Figure 3.4 ((a) and (c)) we can see an example of the structures that are formed

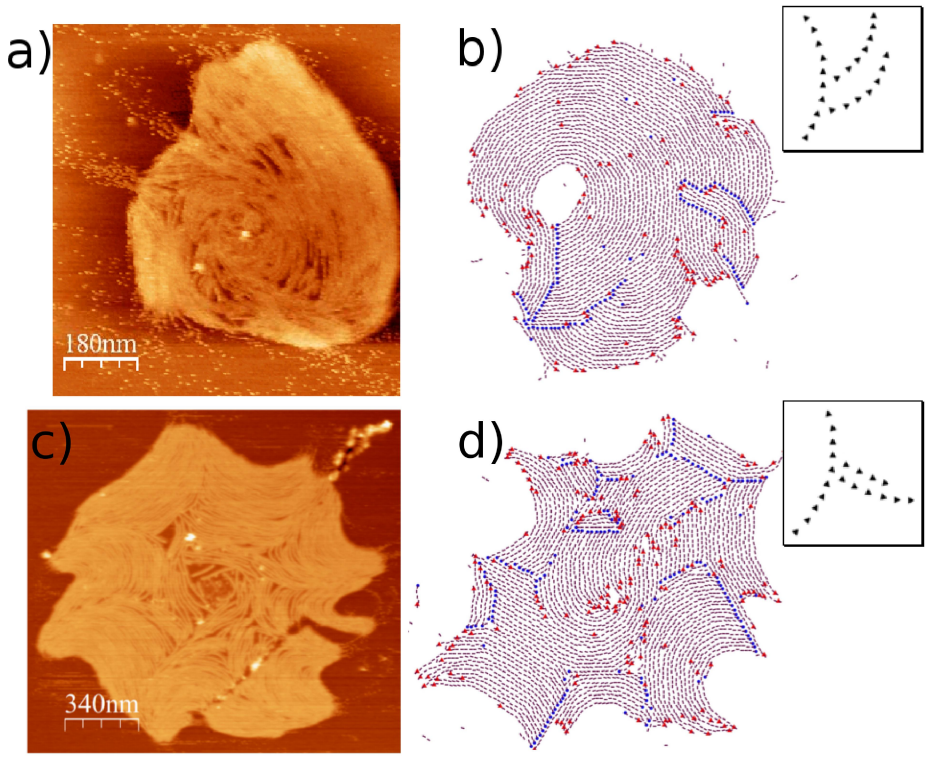

Figure 3.4: AFM images of FtsZ protein mutants Cys2 (a) and Cys255 (c), anchored on *E. coli* Polar Extract bilayer membranes, compared with snapshots of the lattice model (b–d) with the same interaction parameters, (U_b; U_{sl}; U_a; U_+; U_-) = (8; 5,5; 1,25; 6; 0) in k_BT units, and the two choices for the coupling between the spontaneous curvature and the strong lateral bond, illustrated in the respective insets (and in Fig. 3.5). The blue circles and red triangles give the extreme monomers for each filament [25].

with the two different mutants. It is interesting to note that the structures are qualitatively different from those observed in the experiments with mica [24], which suggests that having a fixed orientation of the monomers can enhance subtle interactions that will ultimately shape the aggregates.

To explore the new structures that are formed using FtsZ mutants on a lipid bilayer we developed an extension of the model introduced by Páez el al. [24, 25]. Both the aggregates in Figure 3.4 and the branching filaments observed in Figure 3.6 (b) suggest the presence of an specific, non isotropic and stronger lateral bond (SLB). The collective behaviour of the system enhances this interaction which could not be inferred from an atomistic perspective. The molecular origin and role of this new interaction is not clear; it could turn out that it does not play a part in the Z-ring dynamics, nevertheless, this work stresses how the shape of FtsZ aggregates can be tuned by weak interactions different than the longitudinal

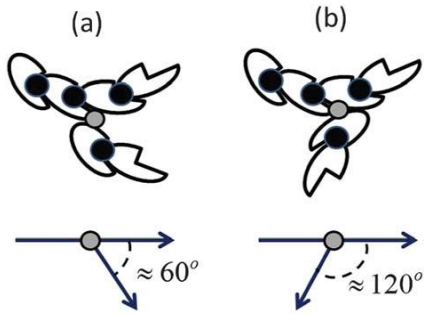

Figure 3.5: Sketches for the two alternative configurations of the strong lateral bonds (SLB). The bottom shows the angle between the heads of the two filaments. Monomers have an arbitrarily asymmetrical shape to show how the tail-to-head direction along a filament is associated with the spontaneous curvature. Black circles represent longitudinal bonds, while grey circles indicate the specific SLB in each case. From [25].

bond between monomers. It is possible that FtsZ binding proteins found *in vivo* could use this plasticity to regulate their function inside the cell.

The new SLB was introduced to reproduce the branching structures observed in AFM images, at about 60°. The SLB was included in the model as a new interaction of free energy $-U_{sl}$. This interaction will be possible only in an specific subset of the interaction crown, at a given angle. On top of that requisite, the neighbour monomer will need to have a certain relative orientation. However, because of the head-to-tail asymmetry the choice for the SLB is not unique. Figure 3.5 shows in detail the two alternatives explored in detail in this section. Both of them will produce 60° degree branching—so they would be very difficult to tell apart from low coverage and short filament images such as those in Figure 3.6 (b). In the first case (Fig. 3.5 (a)) the SLB is formed by contacts between the inner side of a monomer and the outer side of its neighbour, as opposed to (b), where it is an outer–outer contact. The FtsZ mutants Cys2 and Cys255 were selected to be anchored in nearly opposite orientations on the membrane, like turning the shapes up-side-down on the paper as shown in Figure 3.5. The complex three dimensional asymmetry of the protein monomers, and their interaction with the lipid membrane below them, may change the effective interactions between the monomers under that change of their orientation. As presented in Figure 3.4, the best qualitative representation of the experimental structures for the two mutants is obtained with two different choices for the SLB.

In order to fit the parameters we started with the values of reference from the experiments on mica ($\beta U_b \simeq \beta U_+ \sim 10$, $\beta U_a \sim 0{,}5$, $\beta U_- \sim 0{,}5$). The same

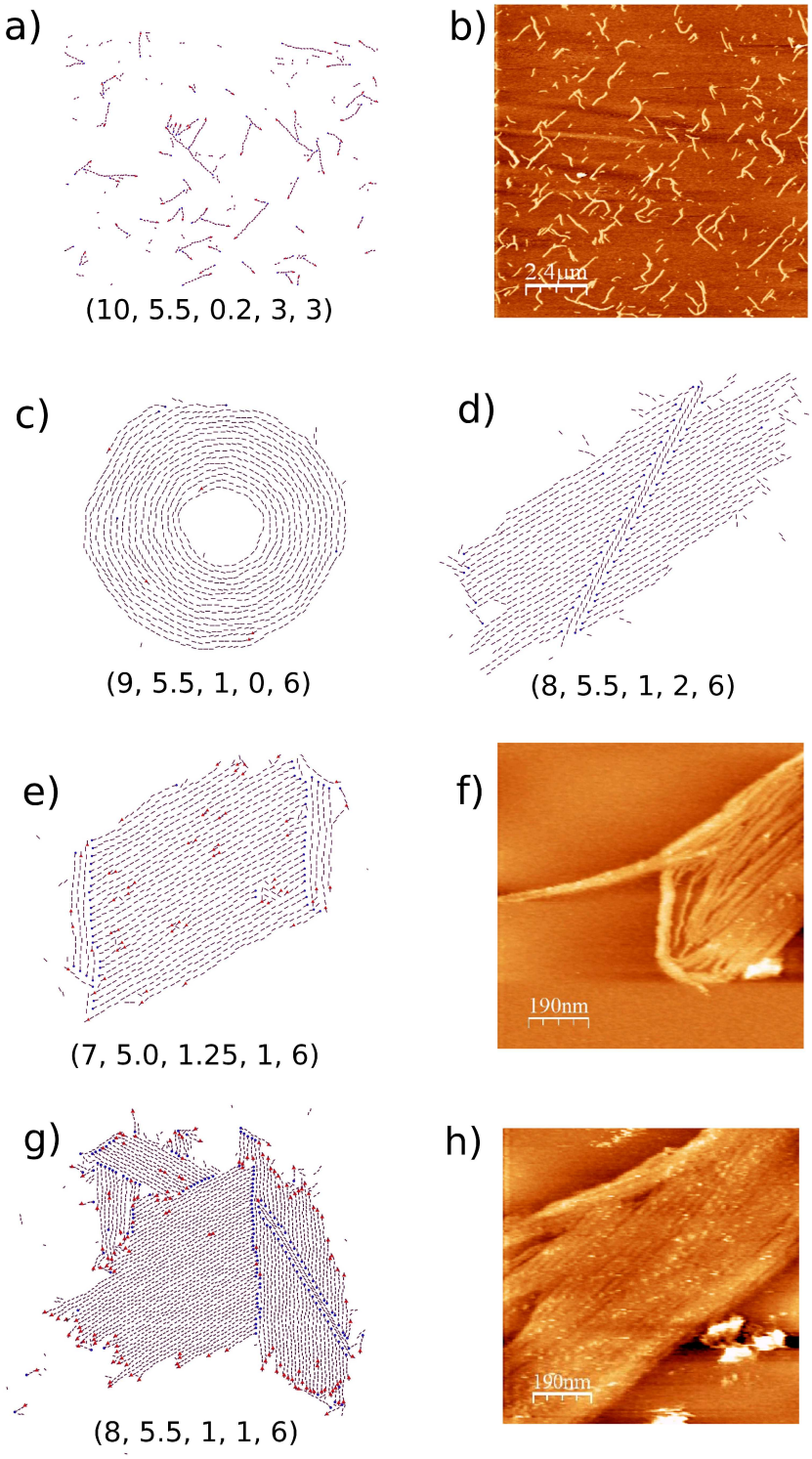

Figure 3.6: (a) Snapshot of the model and (b) experimental AFM image for low protein coverage, with similar branching of the short filaments. (c–e) and (g) are typical aggregates formed in the lattice model with several sets of interaction parameters (U_b; U_{sl}; U_a; U_+; U_-), in k_BT units. The blue circles and red triangles give the starting and ending monomers for each filament. The AFM images (f and h) are taken for FtsZ mutant Cys2 on DOPC bilayer membranes [25].

semi-qualitative exploration was used in this case. In Figure 3.4 we took $\beta U_b = 8$, at the lower limit of the previous range, thus getting somewhat shorter filaments. $\beta U_- = 0$ was the same as with the runs for mica, and βU_+could vary without any noticeable effect in the structures as long as $U_+ \gg U_-$. βU_a was increased from 0,5 to 1 or 1,25, resulting in very few isolated filaments. In these conditions we observe a first order transition with a dense protein monolayer and a rare vapour of monomers and short filaments. For the new interaction parameter, $\beta U_{SL} \sim 5,5$ was more than enough to have an important effect on the aggregates.

These values are only a reference, and tens of simulations were performed with different variations in the parameters, so as to truly explore the different aggregates that can be found using this model. A selection of these simulations gathering the most representative structures observed is presented in figures 3.6 and 3.9. We allowed up to 10^9 MC steps so as to sample even the rare events in which longitudinal bonds are broken ($e^{\beta U_b} \backsim 10^4$ trials).

The method we have described may seem a bit rough and even arbitrary, since we are considering the qualitative shape and texture of the aggregates without any attempt to quantify its geometrical aspects (size distribution of the filaments, number of different bonds, curvature, etc.). Obtaining this quantitative information would be straightforward for this model and it was in fact sometimes done in order to help explore the different aggregates and organize the different simulations (an example is given in Table 3.1), but the resolution of the AFM does not allow a useful comparison with the MC results.

Straight aggregates

During the simulations we observed structures with and without curvature. The most representative cases of aggregates without curvature can be found in Figure 3.6 (d), (e) and (g). All of these aggregates derive from the basic **I** aggregates described in the experiments on mica. As depicted in section 3.1 **I** clusters are 2D nematic drops in which there is a competence between the longitudinal bond (stretched rectangles) and lateral interactions (square-like rectangles). We can perform a very basic analytic study of these aggregates estimating the number of different bonds and the degrees of freedom of different structures.

Although aggregates are irregular and very dynamic structures, as a first order approach we can take 6 as the average number of neighbours for a monomer

inside of the aggregate. Monomers on the sides would be missing 2 of these neighbours. Let n_b be the length (measured in monomers) of the structure and let n_a be its width. Then we have

$$E = (n_b - 1)n_a U_b + [6n_b n_a - 2(2n_b + 2n_a)]\frac{U_a}{2} \tag{3.1}$$

This very rough estimate allows for a reasonable derivation of the width/length value.

When SLBs are included, the short ends of the rectangle in a **I** aggregate tend to be covered by a filament perpendicular to the others. In order to form SLBs (at ~60°) the rectangle is tilted to a rhombic shape. In this way n_a SLBs can be formed at the cost of losing only one longitudinal bond—we have now n_a filaments of longitude $n_b - 1$ ($n_b - 2$ longitudinal bonds) and one new filament of longitude n_a. But in order to form n_a SLBs the filaments now need to share head-to-tail orientation, with a cost in entropy. In the simulations this seldom happens. It is far more common to find both ends covered (losing two longitudinal bonds), thus respecting the head-to-tail orientation freedom. The approximate free energy of this structure is then

$$F = -n_a \ln 2 + n_a U_{sl} + [(n_b - 1)n_a - 2]U_b + [6n_b n_a - 2(2n_b + 2n_a)]\frac{U_a}{2} \tag{3.2}$$

We are disregarding here the fact that covering both ends restricts the freedom in length of the filaments—since having unequal lengths reduces lateral contacts, these differences where never very important.

This last arrangement is not unique. An alternative is to have well-ordered filaments with an origin at each end (Fig. 3.6 (e)). Of course, having two opposed origins implies that all filaments need to be broken somewhere along their length ($n_b - 2$ possibilities). The free energy is thus

$$\begin{aligned} F &= -n_a \ln(n_b - 2) + 2n_a U_{sl} + [(n_b - 1)n_a - n_a - 2]U_b \\ &\quad + [6n_b n_a - 2(2n_b + 2n_a)]\tfrac{U_a}{2} \end{aligned} \tag{3.3}$$

There is yet one more possible arrangement, which can be combined with the previous one in bigger meta-aggregates. In this aggregate the SLBs are within the structure (Fig. 3.6 (d)). It can be seen as a rearrangement of the previous case.

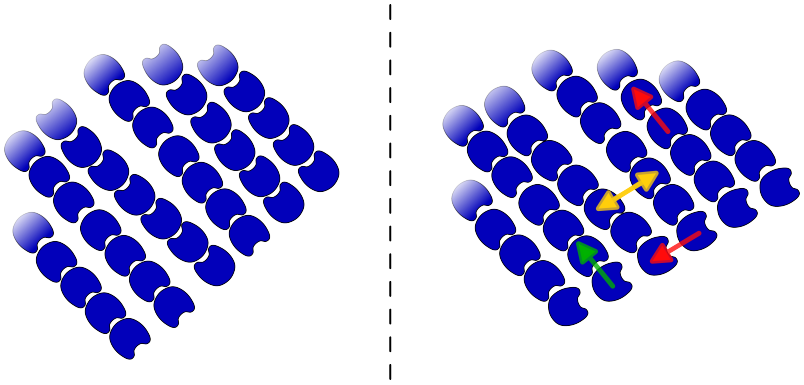

Figure 3.7: Sketch comparing an **I** aggregate with regular end and another where a filament is covering the end forming SLBs. Two longitudinal bonds have been marked in orange, a weak lateral interaction in yellow and one SLB in green. Note that in the first case filaments could have either direction while in the second case one orientation prevents SLB formation.

The only difference is that this one allows for some extra freedom at the ends of the filaments (they can vary slightly in length).

More aggregates with SLB

As has already been partially commented in the previous section, Figure 3.6 is a good example of the very different aggregates that the model will produce with small variations in the parameters. In snapshot (a) we have low protein coverage and weak lateral attraction, well below the condensation threshold. Filaments fluctuate in size and shape, and we can see the effects of the SLB in the Y junctions (at ~60°). These junctions are also easy to identify in the AFM images under low protein coverage of the membrane (b), however, the filaments are too short to tell which SLB configuration (see Figure 3.5) is closer to the experimental observation.

In snapshots (c) through (f) we see different MC simulations with 1200 monomers over a 473 x 507 lattice and different sets of parameters. The average protein coverage is about one monomer per 400 nm², but in all of these simulations we observe two very different phases: there is a condensed cluster (around 20 nm² per monomer) and a very rare vapour of monomers and short filaments. The **O** cluster in (c) is similar to those observed without SLB [24]. In this case the stronger longitudinal interaction dominates the system, leaving very few open ends to take advantage of the SLB which therefore has little effect in this case.

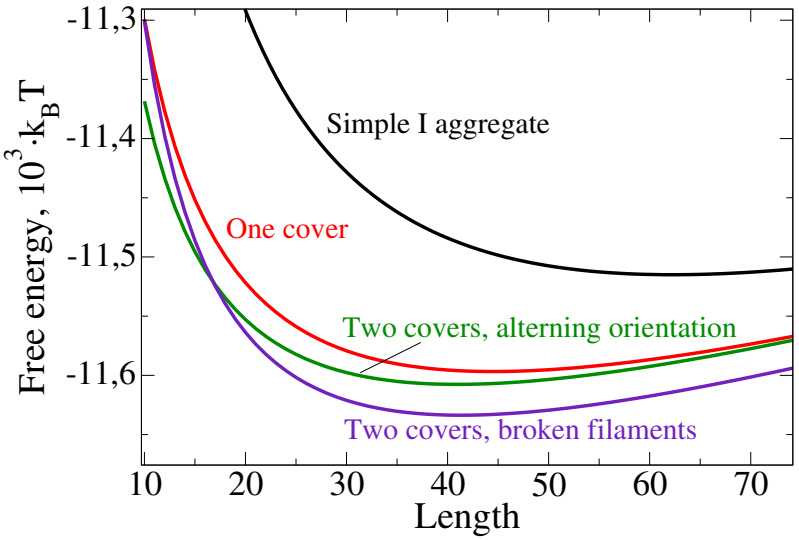

Figure 3.8: Free energy estimate for different variations of the **I** aggregate. U_b = 7; $U_a = 1,25$; $U_{SL} = 5$, all in $k_B T$.

Table 3.1: The number of filaments N_{fil}, their mean length L_{fil}, the number of strong lateral bonds N_{SL}, and the fraction of filaments with a strong lateral bond obtained in the lattice model with the interaction parameters used in the different frames of Figure 3.9. For the different SLB configuration refer to Figure 3.5.

Frame	**SLB**	$\boldsymbol{\beta U_a}$	$\boldsymbol{N_{fil}}$	$\boldsymbol{L_{fil}}$	$\boldsymbol{N_{SL}}$	$\boldsymbol{N_{SL}/N_{fil}}$
a1	(a) 60°	1,0	346	10,4	299	0,864
a2	(a) 60°	1,0	284	12,3	234	0,824
b1	(b) 120°	1,0	299	12,0	206	0,689
b2	(b) 120°	1,0	252	14,3	160	0,635
c1	(b) 120°	1,25	241	14,9	241	0,858
c2	(b) 120°	1,25	157	22,9	157	0,651

Snapshots (d) and (e) show structures derived from the simple **I** aggregate. As has been discussed in detail in 3.2.1, these structures take advantage of the SLB by covering the short ends of the rectangle with filaments and adopting a rhombic shape. As the size of the aggregate increases it is more convenient to form a set of smaller aggregates, which can be a tessellar combination of the different **I** variants, as seen in (g). The AFM images in Figure 3.6 (f) and (h) are taken with the FtsZ mutant Cys2 on a bilayer with 90% *E. coli* polar lipids and 10% DSPE-Mal. The image (f) shows a bundle covering the open ends of the filaments, as in the MC snapshot (e), while the AFM image (h) is qualitatively similar to the patched pattern in (g). Notice that in these clusters the filaments do not show their spontaneous curvature, so that we cannot infer from the AFM images whether the SLB for this FtsZ mutant is better described by (a) or (b) alternatives in Figure 3.5.

As in other *living polymers* systems [26], the specific branching induced by the SLB produces a still higher level of meta-aggregates and networks. Increasing the protein coverage, with 3598 monomers over the same lattice size, we found the structures presented in Figure 3.9, in which the spontaneous curvature of the filaments and the specific angles given by the SLBs induce a rich variety of meta-cluster structures. In this case we keep the interaction parameters near the choice used in Fig. 3.4, only with a small decrease in the isotropic attraction to $\beta U_a = 1$ in panels (a) and (b), which is reflected in the formation of some short filaments or small clusters separated from the main cluster. In panel (c), with the same value $\beta U_a = 1,25$ as used in Figure 3.4, the number of monomers away from the main cluster is marginal.

The shape of these clusters is determined by how the filament ends of the **C** aggregates may form SLBs with the external filaments in other **C** clusters, as shown in the snapshot (a1). Closed **O** shapes would be less effectively clustered, since they have less (or none) filament ends to form SLBs. The **O** clusters, which were often seen in the AFM images on mica [27], become rare when the protein is anchored to the bilayer membrane in a specific orientation. Instead, the FtsZ filaments form **C** metaclusters like those in Figure 3.4. Moreover, our MC simulation results show that the filaments may be aggregated in other possible forms, in particular, in (a2) we observe a SLB-closed spiral shape, as an hybrid between **C** and **O** clusters, and also strings of **O** aggregates, kept together by short external filaments (b2). That polymorphism induces a strong sensitivity to the details of the interactions in the model. Snapshots (a) correspond to the SLB

topology in Figure 3.5 (a), while those in (b) and (c) correspond to the SLB in Figure 3.5 (b).

Relevance of the initial state

The computer simulations based on this fine-grained model show long relaxation periods over different time scales for different structures (filaments, small clusters and meta aggregates), as is typical in *living polymers* networks. In Figure 3.9 we have an example of this evolution. The two columns show different times of the simulations, which started with a random distribution of monomers. After $32{\cdot}10^6$ MC steps, the first column should already be considered a rather late period of the evolution of the system (a long time past the simple short filaments forming very small clusters). The aggregation of these smaller filaments in **C** clusters and meta clusters enhances nucleation and eventually results in the complex aggregates we can see in the first column of Figure 3.9. The evolution of these complex structures takes much longer periods. The second column shows snapshots after $160{\cdot}10^6$ steps, and the structures are still evolving. The evolution of **C** and **O** clusters usually involves head-to-tail inversion of filaments, something that cannot be achieved by simple reptation. Fragmentation events are possible, but much less likely to occur, at a rate of about one event in $\backsim 10^4$ trials.

In the evolution of the experimental AFM images changes of similar characteristics appear over a time scale of hours, while the biological cycle for the formation of the Z-ring occurs in a scale of minutes, with a total number of protein monomers per cell similar to that used in our simulations (3598). Therefore, the typical shapes of the protein aggregates during their evolution may be more relevant than their truly equilibrated configurations, which would be observed only after times which are too long compared with the cell cycle.

As was discussed in 3.2 the computer simulations offer a level of information beyond the resolution of the AFM images. Some of this information was gathered in Table 3.1, for the results in Figure 3.9. As could be expected, even after $32{\cdot}10^6$ steps (first column) the number of filaments still decreases and their mean length increases, another proof that true equilibrium requires very long simulations. **O** aggregates have fewer open filaments, so when they are prevalent there are less SLBs—Figure 3.9 (b). In (a) we find the intermediate structure between **O**

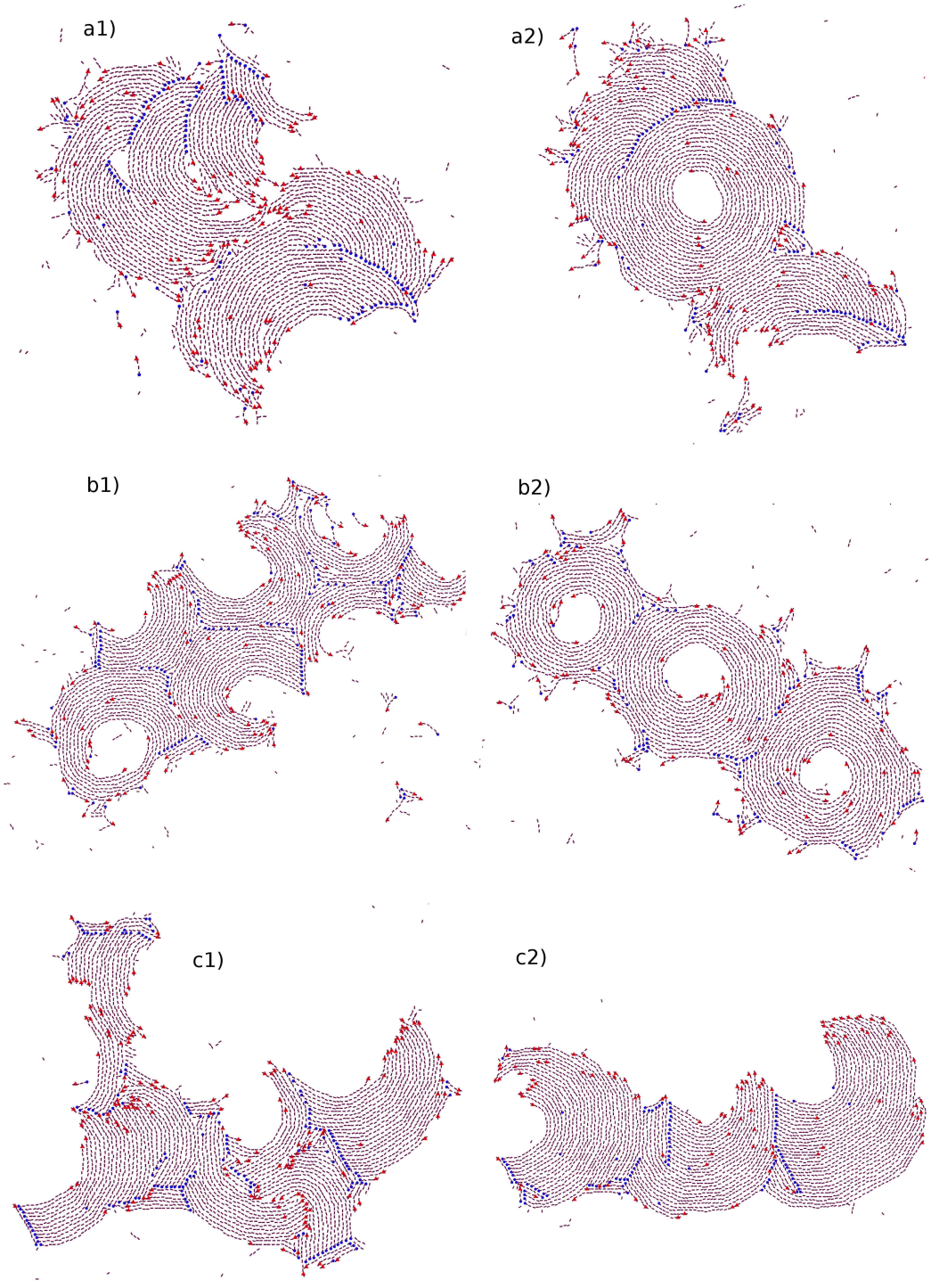

Figure 3.9: Three pairs of complex aggregates formed by curved filaments. The images at the left correspond to an earlier stage of the simulation. For (a1) and (a2), the neighbour was required a relative angle of 60 to form SLB, while for (b) and (c) this angle was 120, as depicted in Figure 3.5. For set (c) we used the model interaction parameters of Figure 3.4, while for sets (a) and (b) the isotropic lateral attraction was lowered to $\beta U_a = 1$ [25].

and **C** aggregates (spiral rings), which allows to keep a SLB in over 80% of the filaments. This new structure is possible because in (a) the SLB angle is that of Fig 3.5 (a), ~60°, in contrast to the 120° configuration (Fig 3.5 (b)) of snapshots (b) and (c). As has already been observed in the absence of SLBs [35], the balance between **O** and **C** clusters may be shifted towards the later by increasing the lateral interaction, as was done between the systems in Figure 3.9 (b) and (c).

It is relevant to note that, even though only 5 to 10% of the monomers are directly involved in the formation of SLBs, they are determinant for the global aspect of the meta-aggregates.

The evolution of the clusters is very sensitive to the initial state of the system. The simulations in Figure 3.9 evolved from a random distribution of monomers, and the result contrasts with the globally round shape of the experimental clusters in Figure 3.4. These images were obtained following a special procedure: first, a solution with FtsZ but no GTP is used on the membrane. FtsZ monomers attach to the surface and start to condensate, not to form filaments (since there is no GTP the bond is not possible or is at least very weak), but forming lateral interactions (which have no relation with GTP). In this way a 2D FtsZ drop condenses, and then GTP is added to the buffer. Filaments are very quickly formed within the protein drop and the final structure conserves the globally round shape of Figure 3.4.

It is possible to mimic this process in the simulation. To do so, the longitudinal interaction is not considered ($\beta U_b = 0$) for some MC equilibration runs. Lateral interactions promote the condensation of a 2D drop and afterwards the longitudinal interaction takes its usual value. In order to accelerate this process the isotropic lateral interaction can be slightly increased during the equilibrium runs. This procedure resulted in the simulations seen in Figure 3.4, quite different to those obtained from a random distribution of monomers in Figure 3.9.

This malleability of the condensed forms, so that small changes in the interaction parameters, or even in the initial conditions, may produce important changes in the global structure, was associated with a relatively narrow range of values. The biological tuning of FtsZ to get this malleability is probably associated with the biological function of the protein that has to be induced, through weak biochemical signals, to form (and to dissolve) the global structure of the septal ring, at the central position on the bacterial membrane, and at the correct time in the cell cycle.

Some remarks on the SLB study

We have shown how a small number of SLB's determine the complex struand perhapsctures analysed in this section. The specific topology of the SLB will either induce back-to-back aggregation of **C** clusters—Figure 3.4 (d) and 3.9 (b) and (c)—or nested **C** clusters as seen in Figure 3.4 (b) and 3.9 (a).

The experimental AFM image in Figure 3.4 (c), taken with FtsZ mutant Cys255 on 90% *E. coli* Polar Extract and 10% DSPE-Mal, presents smooth concavities in the perimeter of the cluster separated by pointed regions, and can be clearly associated with the SLB configuration (b) in Figure 3.5. The shape of the cluster in Figure. 3.4 (a), taken with the FtsZ mutant Cys2 on the same membrane, is very different to that with the Cys255 mutant, and it is much similar to the MC snapshot (b), obtained with the configuration (a) for the SLB in Figure 3.5. In this way we are able to discern details of the preferred branching in the interaction between monomers of different mutants, anchored to the membrane at different positions.

The branching effects that have been studied here are amplified through the collective behaviour of the system and, in this way, they influence the global shape of the aggregates. The statistical physics approach that we have used aims to identify in experimental images of relatively low resolution the most relevant interactions of the system, and should be nicely complemented by atomistic studies trying to explain the molecular origin of these interactions.

Notice that the experimental AFM images discussed in Figure 3.4 are very characteristic aggregates observed only under the new biomimetic conditions explored in the recent experiments [28], with specific anchoring of the protein on a lipid bilayer. The structures are very different from those observed when the protein is directly absorbed on mica, in which there is no evidence of branching filaments, probably because the preferential orientation of the protein monomers on the substrate is more loosely defined, and the specific interactions leading to the SLB observed here become smeared into the isotropic lateral attraction. It is also relevant that the experimental results with different mutants, with opposite orientations on the lipid bilayer, may be correlated with the patterns observed in MC simulations with the alternative configurations of the SLB in our model.

The SLB is a rather subtle effect that was not observed in mica experiments. It could turn out that the SLB plays no role in the division process *in vivo*, perhaps

lost in the isotropic interaction if the attachment of the monomers to the membrane is flexible as happened in the mica experiments. However, this study shows how weak interactions, even if few in number, can control and modify FtsZ aggregates. We know that the Z-ring complex involves many proteins which role is not yet clear [14], with this work in mind, even apparently weak and unimportant interactions among these proteins could have an important role in the regulation of the Z-ring.

This work also brings our attention to a neglected aspect in the Z-ring problem: the dramatic importance of the details of FtsZ anchoring. We have seen how switching from the unspecific mica anchoring to the very specific mutant attachment to a membrane produces entirely new structures. Furthermore, changes in the angle relative to the membrane (different mutants) also produces different results, which range from aggregates of straight bundles to collections of curved structures [28]. This new dimension of the problem will be further elaborated in chapter 5.

4

A dynamic model for comparison with FRET experiments

In the introduction it was mentioned that FtsZ is the bacterial homologue of tubulin. Both self-assemble in long filamentary structures, using a GTP nucleotide to form the longitudinal bond. They also present GTPase activity, meaning that the formation of the bond enclosing the GTP molecule catalyzes its hydrolysis to GDP. The cell metabolism regenerates GDP back into GTP form. Thus, the nucleotide is degraded inside the protein structures that it helps to assemble, and its consequent degradation induces their disassembly. The micro-tubules formed by tubulin have very peculiar dynamics, with periods of steady growth interrupted by sudden disassembling catastrophes produced by the assembly-hydrolysis-disassembly cycle of proteins and nucleotides. Eukaryotic cells can control this complex biochemical activity and they use microtubules as essential components of the cell machinery. Prokaryotic cells use FtsZ as the main component of the Z-ring, responsible for the production of constriction force during divison.

The structural homology of FtsZ and tubulin and their activity as self-assembled cytoskeletal GTPases point to a common ancestor, but there are crucial differences between them, both in the structure of their aggregates and in the kinetics of the GTP hydrolysis. The microtubules are ordered cylindrical structures made of 13 proto-filaments of tubulin, which may grow up to lengths of microns. In contrast, FtsZ structures are much more malleable and polymorphic. In chapter 3 we analysed the diverse aggregates formed by FtsZ on a planar substrate, from

rings and spirals to two-dimensional nematic drops and more complex patterns. FtsZ proto-filaments behave like *living-polymers*; their longitudinal bonds are strong enough to produce hierarchical organization (monomers into filaments, filaments into bundles, and bundles into larger structures) but weak enough for the filaments to be broken, shuffled and remade under thermal fluctuations at room temperature.

There is a second and crucial difference between FtsZ and tubulin. The rigid structure of the microtubules does not allow for nucleotide replacement without recycling the tubulin dimers from the bath. In contrast, the flexible FtsZ aggregates might be able to replace the hydrolyzed GDP in their bonds by fresh GTP from the bath without liberating the protein monomers from their aggregates. The rate of the GTPase activity has been reported to range between 0.6 and 6.1 GTP per minute and per FtsZ monomer, depending on the ionic composition of the buffer. In this chapter we will assume a typical reaction rate of 3 GTP molecules per minute and FtsZ monomer, i.e., $k_H \simeq 0.05\,\mathrm{s}^{-1}$.

We will try to analyse some of the results from the fluorescence and electron microscopy studies of Chen and Erickson [29], which provide insight into the cooperative (non-isodesmic) effects for the assembly, mixture and disassembly of FtsZ aggregates in bulk solution. A qualitative picture for the different processes linking nucleotide hydrolysis and protein exchange is given in Fig. 8 of that reference. In this chapter we will address the question of how to integrate the kinetics of nucleotide hydrolysis and the cooperative replacement of protein in a semi-quantitative model with the time scale and the structural information given by the experiments.

4.1 Square-lattice model

Since we cannot aim to more than a semi-quantitative comparison, we use a coarse-grained model based on that of Lan et al. [23]. Protein monomers are represented by particles with only four possible orientations on a square lattice. Only nearest-neighbour interactions are considered. Weak lateral bonds are considered in the model for every neighbour (aligned or otherwise) which does not form a longitudinal bond, with free energy $-U_a$. When monomers are aligned they may form a bond, although this is not a necessary requirement. Bonds can be mediated by either GTP or GDP, with free energy $-U_T$ and $-U_D$ respectively. The model also considers monomers linked to a GTP nucleotide that are unbonded

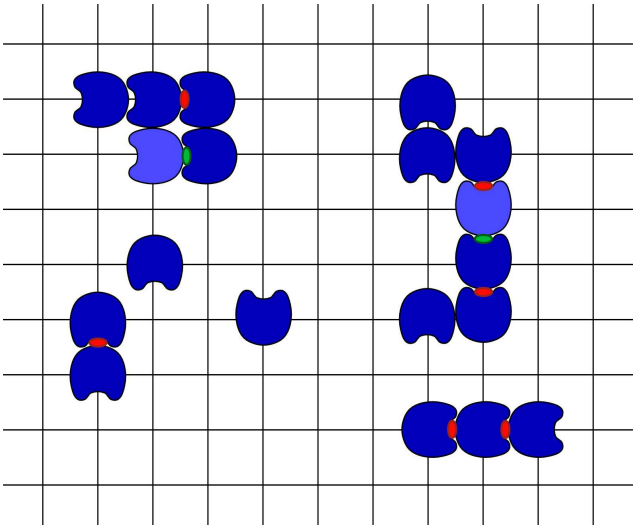

Figure 4.1: Schematic representation of the square-lattice model. Notice that not all the monomers that are aligned are necessarily bonded. GTP-bonds are represented in red, GDP-bonds in green.

(open-GTP) even though they are correctly aligned with a neighbour. Unbonded monomers with GDP are included in this model as well, although the process of recycling GDP (exchanging it for GTP) in an open bond is assumed to be very fast, so open-GDP states have been automatically turned into open-GTP.

These open states serve a double purpose. On the one hand, they are needed in order to respect the detailed balance principle, which states that *at equilibrium, each elementary process should be equilibrated by its reverse process.* On the other hand, they represent (at the coarse level of the model) what is observed in AFM images of FtsZ rings on mica in a buffer with high GTP concentration but depleted of protein (so that there is no polymerization) [35]. These FtsZ rings are observed for several minutes before experiencing fast depolymerization. Given the hydrolysis rate of about $k_H \simeq 0.05\,\mathrm{s}^{-1}$, each monomer must hydrolyse (and replace) its nucleotide over a 1000 times before the ring finally breaks. At the resolution of the AFM images the nucleotide exchange is not observed, either because it requires a very small change in the distance between the FtsZ monomers or because that gap is closed too rapidly, and it is rarely caught in the images unless the two ends of the filament are seen to move away from each other in the irreversible opening of the ring. Even the faster depolymerization is slow enough that every bond should hydrolise its nucleotide around 50 times before finally breaking.

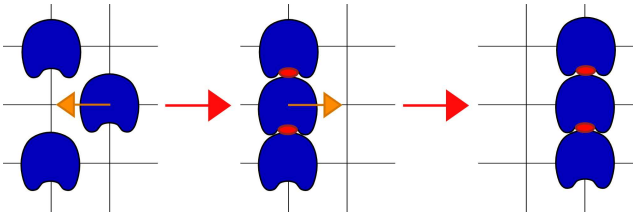

Figure 4.2: Detailed balance (*each elementary process should be equilibrated by its reverse process*) is broken if bonds are automatically formed.

The Monte Carlo dynamics of the model consider movement, rotation and bond dynamics. Bond dynamics consist of two different processes (see figure 4.3). The first process tries to change the state of the bond between *open* and *closed*, so that two unbonded monomers that are aligned can bond, and bonded filaments can break. This happens with frequency ν_0, but breaking events are accepted with frequency $\nu_0 e^{-\beta U_T}$ and $\nu_0 e^{-\beta U_D}$ when the Boltzmann factor for breaking a bond is taken into account. The second process—with frequency ν_h—checks the nucleotide that mediates the bond. If it is GTP, it is hydrolysed and transformed into GDP. (Open-GDP monomers are automatically transformed into open-GTP.) Notice how this implies that only the nucleotides inside of a bond can be hydrolysed. All of these changes are accepted or rejected according to the Metropolis algorithm.

Here we have introduced two variables, ν_0 and ν_h, but they are not independent, since the hydrolysis cycle rate is fixed:

$$\frac{1}{\nu_h} + \frac{1}{\nu_0 e^{-\beta U_D}} \simeq k_H. \tag{4.1}$$

On top of these *bond processes*, rotation and movement of the monomers is also considered. Stoke's law gives the diffusion constant for a spherical particle in a fluid. Because we know the size of the monomer (and thus the size of the lattice steps) we can correlate the simulation steps with real time increments. In particular, we find that the diffusion constant is equal to

$$D = \frac{\mathrm{k_B T}}{6\pi\eta r} \simeq 80\,\mu\mathrm{m}^2/\mathrm{s}, \tag{4.2}$$

where η is the viscosity of the fluid and r is the radius of the spherical particle. This value should be compared with the much slower time scale for the hydrolysis cycle observed in all the experiments, indicating that the protein exchange is not limited by the diffusion of the monomers.

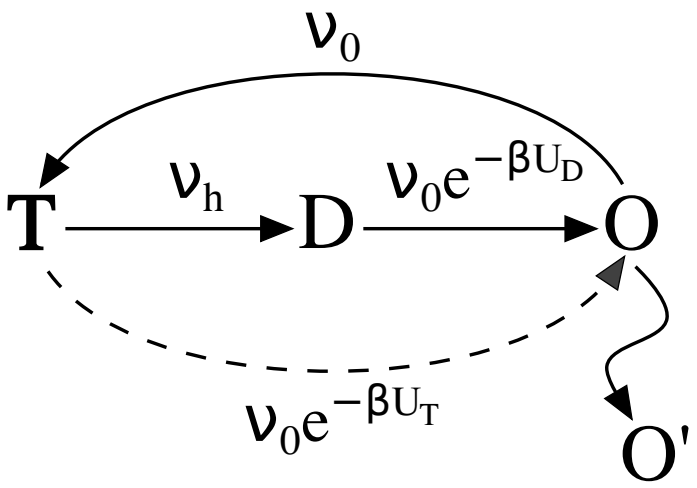

Figure 4.3: Bond dynamics of the model with the corresponding acceptance frequencies. GTP-bonds can be hydrolysed to GDP-bonds. Both of them may be broken. This process is tried with frequency ν_0 and implies a decrease in energy of either $-U_T$ or $-U_D$. Open bonds can bond (if there is a suitable neighbour) also with frequency ν_0. In the meantime, movements and rotations may affect the monomer and separate it from its former neighbours.

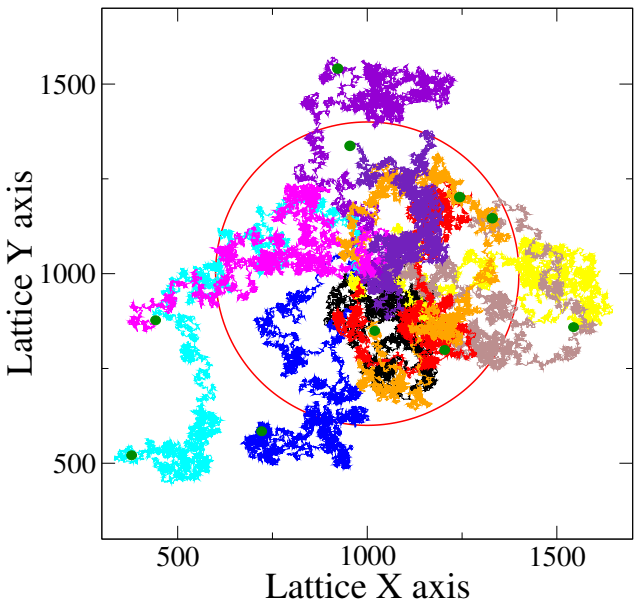

Figure 4.4: Simulations of diffusion for a single monomer. Ten different cases are shown. Green circles mark the ending points of the different trajectories, and the red circle is the expected average distance from the starting and ending points. The simulations cover around 0.01s.

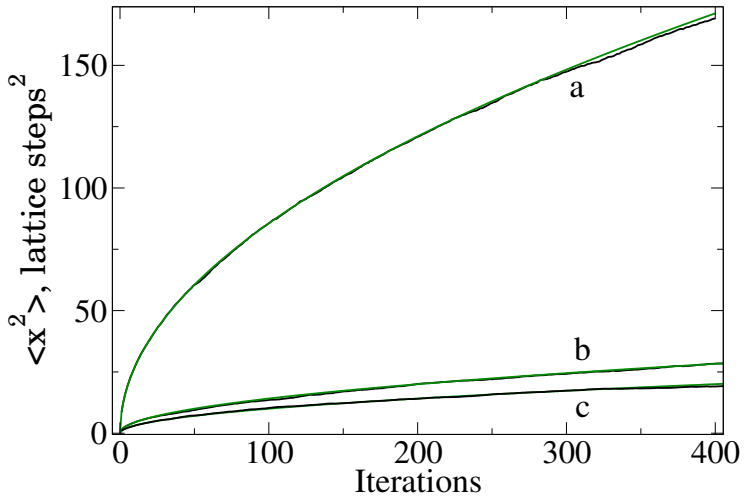

Figure 4.5: Average distance from the origin for random walks. **c** considers jumps of ±1 step in only one axis, in **b** there are ±1 step jumps in both axis, and in **a** the jumps are also simultaneous in both axis and up to ±10 steps. Black lines are simulations, green lines are the predicted behaviour.

For a random walk we know that the distance after i steps should be

$$\langle x^2 \rangle_{rw} = i \tag{4.3}$$

And for a particle in a fluid we have

$$\langle x^2 \rangle_{fl} = 2\mathrm{dim} D t \tag{4.4}$$

where dim is the dimension of the system. Using these two equations we find that over 10^7 iterations are needed to simulate the equivalent of one second *for a single monomer*. If we take into account that not all of the iterations are movement trials we will need even more. Therefore, if we want the simulation to cover the 20 s of an average hydrolysis cycle we end up with ~ 10^9 iterations even with a single monomer, which requires too much computer time. The work around this problem is to increase the step size of the monomer movements. We allowed up to 10-step jumps in the x and y axis, and gradually reduced the maximum step size for filaments down to a single lattice space for filaments longer than 9 monomers—since single monomers are expected to have higher mobility. With this increased mobility, 1 s of simulation for 500 monomers will only require a bit over 10^8 iterations.

In order to mimic the FRET experiments of reference [29] two different labels are assigned to the monomers, which are of kind 1 or 2. When a monomer of

kind 1 does not have any monomer of kind 2 as a neighbour, then it is considered to emit fluorescence of kind 1. If it has at least one neighbour of kind 2, then it emits fluorescence of kind 12.

4.2 Simulations

In the previous section it was mentioned that ν_0 and ν_h are linked by the relation

$$\frac{1}{\nu_h} + \frac{1}{\nu_0 e^{-\beta U_D}} \simeq k_H. \tag{4.1}$$

This means that ν_0 or ν_h are not independent, but a value for the pair still needs to be specified. In the following simulations we used mainly three different values (measured as the probabilities of an event happening each iteration of the simulation), although the first set is used when none is specified:

$$\begin{aligned} &1)\, \upsilon_o = 5{\cdot}10^{-5},\ \upsilon_h = 2{,}260{\cdot}10^{-7} \\ &2)\, \upsilon_o = 5{\cdot}10^{-4},\ \upsilon_h = 1{,}849{\cdot}10^{-7} \\ &3)\, \upsilon_o = 5{\cdot}10^{-3},\ \upsilon_h = 1{,}816{\cdot}10^{-7} \end{aligned} \tag{4.5}$$

The choice is not irrelevant, because it will determine how long the bond remains at the different states (closed-GTP, closed-GDP and open-GTP) effectively affecting the bonding energies. Imagine the extreme case where hydrolysis is almost as slow as the whole cycle. This implies that as soon as the monomer is hydrolysed the bond is broken and the nucleotide recycled. In the inverse situation hydrolysis would be very fast, but the GDP-bond would take longer to break. The relative population of GDP-bonds will be much smaller in the first situation, which as a result will have a stronger average bond. The effect is somehow similar to changing the concentration of GTP in the buffer, which will also affect the GTP/GDP balance.

The basic simulations that were studied are assembly and disassembly of FtsZ filaments. Disassembly was induced by either enlarging the lattice (which is equivalent to a dilution of the system) or by not allowing open-GDP monomers to exchange their nucleotide back to GTP (which is equivalent to saturating the buffer with GDP). The FRET emulation allows mixing simulations, in a similar way to the experiments by Chen and Erickson. For these simulations we start with FtsZ filaments which are marked of kind 1 or 2. As the simulation evolves

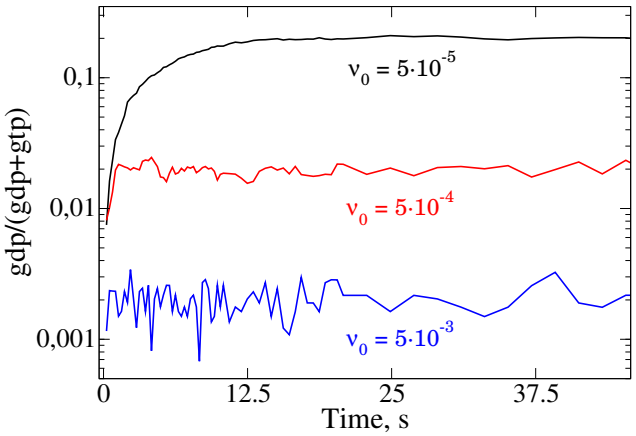

Figure 4.6: Relative fraction of bonding nucleotide as a function of the values of ν_0 or ν_h (see equation 4.5).

monomers slowly interchange between the different filaments, a process which is reflected in the simulated FRET signal. But the computational setup allows to go into further and explore detail that cannot be tackled experimentally.

For these new mixing experiments we have to override the kind-parameter of the monomers, which we use now to label filaments and clusters. In this way, if we analyse the system at given intervals, we can determine the origin of the different monomers. We can know, for example, if a filament has been rearranged, but also if the new monomers come from a filament in the same cluster or a different cluster, and even if the new monomers come from the gaseous phase (unbonded monomers).

Figure 4.11 shows how the choice of the frequencies ν_0 and ν_h has a remarkable effect on the mixing dynamics of the system. Note that the vertical lines mark regions with different intervals of analysis. (During the first part of the simulation the system is analysed every 0.26 s, then every 0.52 s and finally every 2.04 . The longer this interval is, more events will happen, as seen in the graphs.)

With $\nu_0 = 5{\cdot}10^{-3}$ most of the exchanged monomers come from filaments in the same cluster, with only a fraction of the mixing coming from other clusters. This is the result of the high condensation of the system into typically two different clusters, one vertical and other horizontal (which makes mixing between them even more unlikely). This condensation is very fast, as is reflected in the narrow peak in mixing activity that can be seen in the earliest steps of the simulation.

The situation is inversed when $\nu_0 = 5{\cdot}10^{-5}$. The final mixing frequency is very similar to the case with $\nu_0 = 5{\cdot}10^{-3}$, however, almost all of the mixing comes from other clusters. Actually, as can be seen in 4.13, this is because there is very little

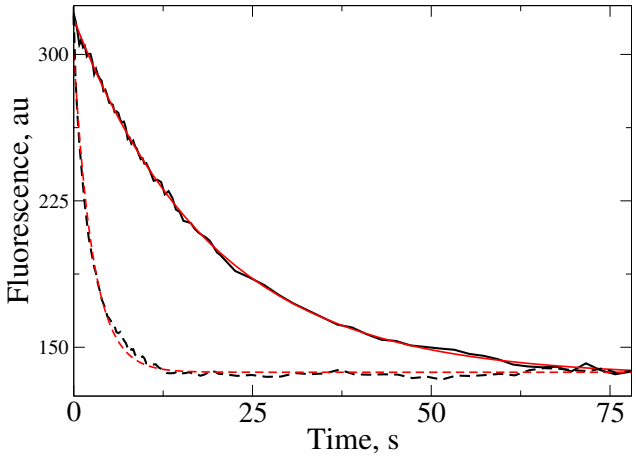

Figure 4.7: Simulated FRET results for assembly (dotted lines) and mixing simulations. Assembly starts from a random monomer distribution, while mixing starts from long filaments in clusters marked as kind-1 or kind-2. In this case $U_T = 12\,k_BT$, $U_D = 3\,k_BT$, $U_a = 0.3\,k_BT$. The results were fitted to an exponential curve ($A_0 + A_1 e^{-A_2 t}$). Compare with figures 1 and 2 from reference [29].

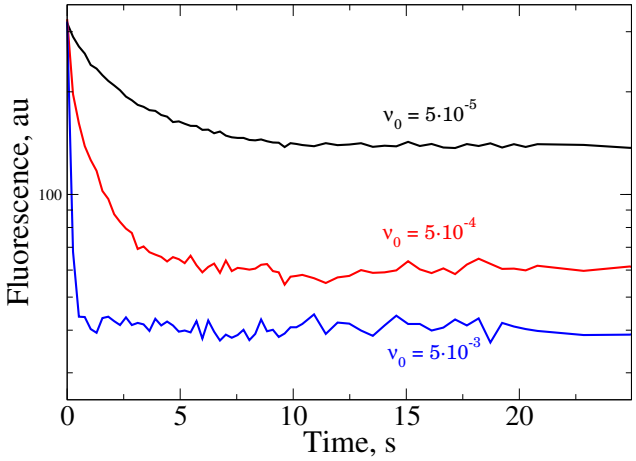

Figure 4.8: Effect of ν_0 and ν_h on assembly simulations.

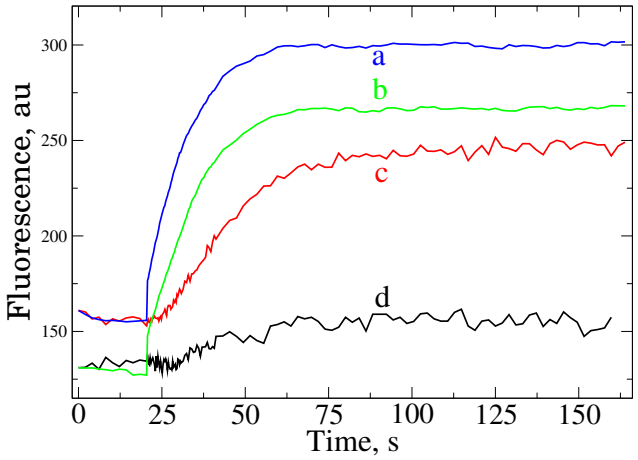

Figure 4.9: Simulated FRET signal during disassembly processes. Disassembly was induced by a 16-fold dilution (**a** and **b**) and stopping nucleotide recycling (**c** and **d**). U_D equals $3\,k_BT$ for (**a** and **c**) and $5\,k_BT$ for (**b** and **d**) respectively. Compare with figures 4 and 5 in reference [29].

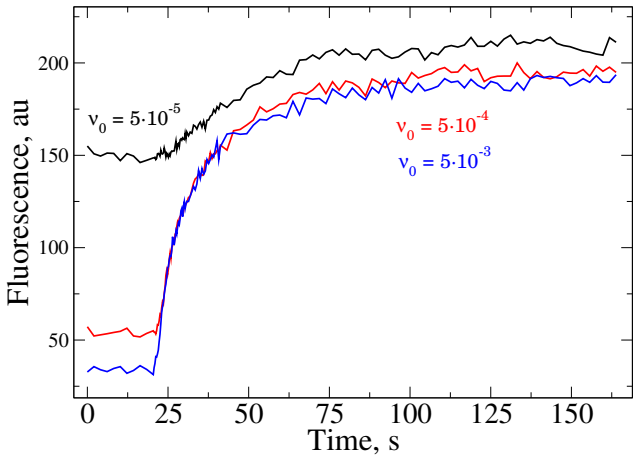

Figure 4.10: Effect of ν_0 and ν_h on disassembly simulations. Disassembly is caused by not permitting nucleotide exchange (GDP→GTP).

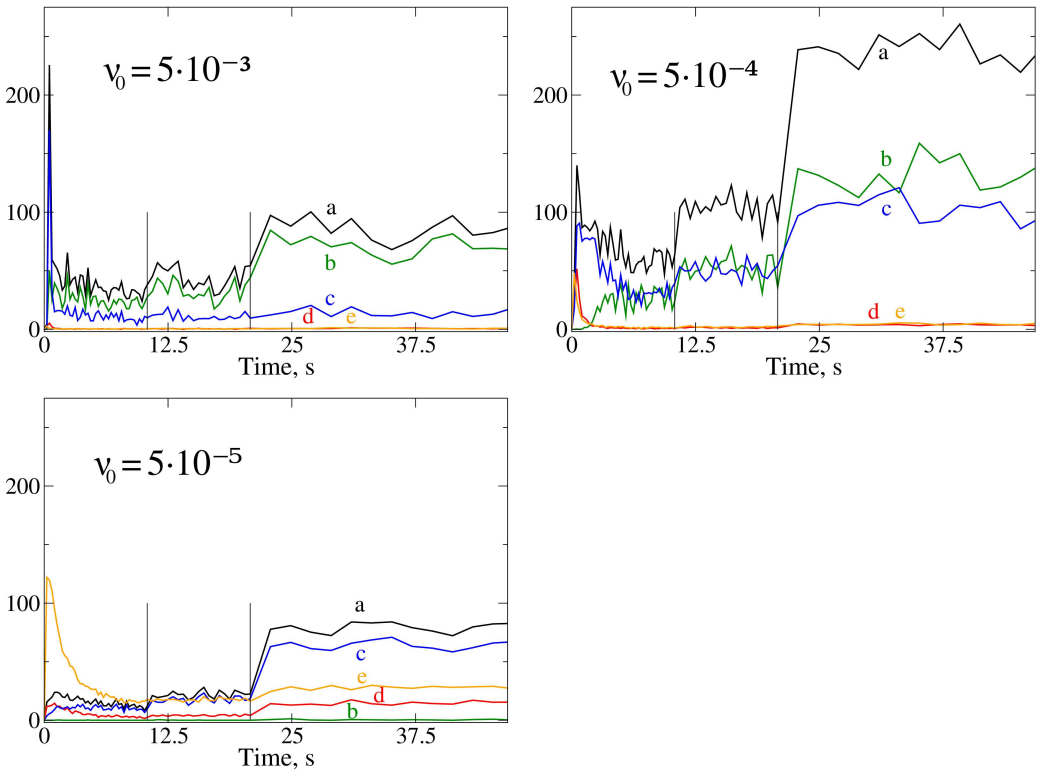

Figure 4.11: Different mixing events in number of monomers involved (for simulations of 750 monomers). The black line (**a**) shows the total number of mixing cases. Line **b** counts the monomers that come from other filaments in the same cluster, while those coming from other clusters are counted in **c**. Line **d** counts the monomers that have come to a filament from the gaseous phase, whereas **e** shows those that have gone to the gaseous phase from a filament. These last monomers (**e**) are not included in **a**. The vertical lines separate regions with different analysis intervals. In the first region the time increments are 0.26 s, in the second they are 0.52 s and in the last region the increments are 2.04 s. $U_T = 12\,k_BT$, $U_D = 4\,k_BT$, $U_a = 0.3\,k_BT$.

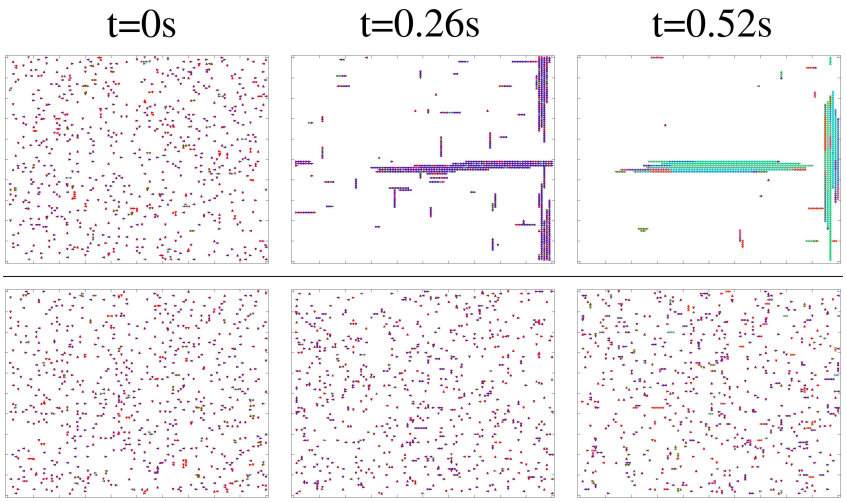

Figure 4.12: Early evolution of a simulation for $\nu_0 = 5{\cdot}10^{-3}$ (top) and $\nu_0 = 5{\cdot}10^{-5}$ (bottom). $U_T = 12\,k_BT$, $U_D = 4\,k_BT$, $U_a = 0.3\,k_BT$.

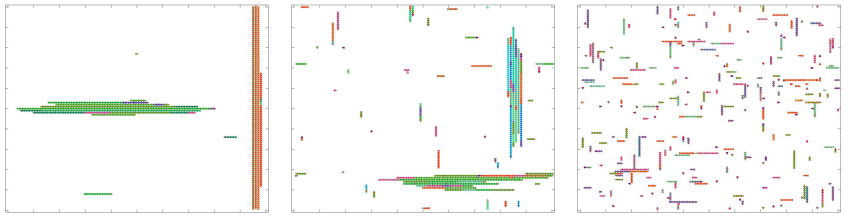

Figure 4.13: Final state of three different simulations with $\nu_0 = 5{\cdot}10^{-3}$, $\nu_0 = 5{\cdot}10^{-4}$ and $\nu_0 = 5{\cdot}10^{-5}$ respectively. $U_T = 12\,k_BT$, $U_D = 4\,k_BT$, $U_a = 0.3\,k_BT$.

aggregation in this case, with free filaments or small clusters. This also explains why there are many more events involving free monomers with this choice of frequencies. The early simulation times in the graph show a number of free monomers coming from filaments much greater than the total number of mixing events. This is because when most of the monomers in a filament come from the gaseous phase it is not considered a mixing event (it is understood as a regular assembly process).

The intermediate case $\nu_0 = 5{\cdot}10^{-4}$ produces more balanced simulations, with most monomers in two main clusters but also many others in small filaments and free monomers. The result is that there is a much higher volume of mixing in the system (almost three times more), with about half of the events coming from filaments in the same cluster and the other half from monomers in other clusters.

Finally, we can study how bonds are broken and repaired. When a bond is broken in our lattice the monomers remain as physical neighbours, so unless one of the sub-filaments is moved the monomers will have the chance to reunite.

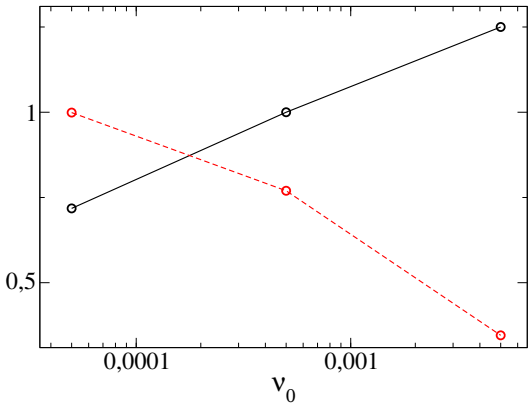

Figure 4.14: Relative number of broken bonds (back, continuous) and fraction of bonds that are NOT repaired before the separation of the fragments (red, dashed). (Multiply by 46039.5 to find the absolute number of broken bonds in the analysis interval.)

The likelihood of this repairing process will depend on the parameters of the system. A higher value of ν_0 means that a repair event will be more likely before any movement finally separates the filaments.

Evolution of filament rings

For another set of simulations a single filament ring was tested. Because the square lattice does not allow curvature rings are created taking advantage of the periodical boundary conditions. The lifetime of the ring is measured when the first fragmentation event occurs, after which fragmentation of the longest remaining filament is observed.

Depending on the specific parameters fragmentation will stall when the equilibrium length is reached. At this length (which can be as high as 40 monomers for $\nu_0 = 5{\cdot}10^{-3}$) breaking of the filament is as likely as fusion of the disperse fragments in the system. This effect could be prevented by removing the shorter fragments, which would allow to extend the results for shorter lengths.

The most remarkable effect is that bigger values of the frequency ν_0 make fusion events more likely, and allow for broken bonds to be repaired more easily (see figure 4.14) which results in longer lifetimes and a longer equilibrium length.

Longer rings have shorter lifetimes because bonds are broken randomly with a given chance. Since in a longer the ring there are more bonds there are also more chances of fragmentation by random breaking of two of these bonds. Note that

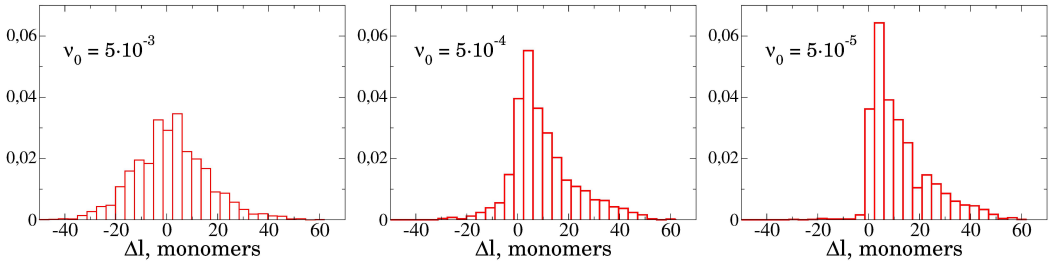

Figure 4.15: Histograms of length changes during the disassembly of filament rings. Negative values correspond to events where the length is increased by fusion of fragments.

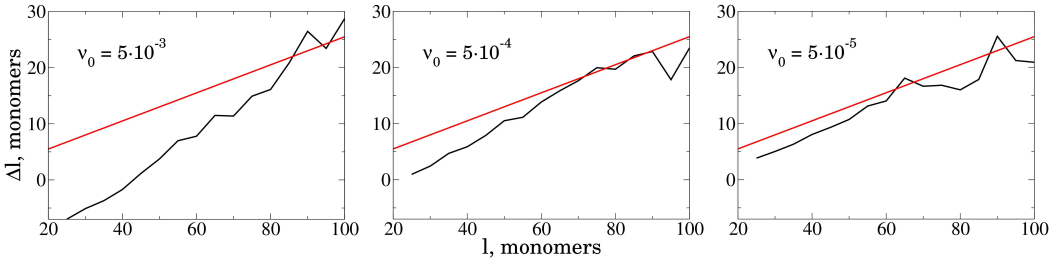

Figure 4.16: Average length of the filament fragments lost during ring disassembly as a function of the length of the filament at a given time. The red line is the expected result for random bond-breaking events. The deviation is caused by fusion of fragments.

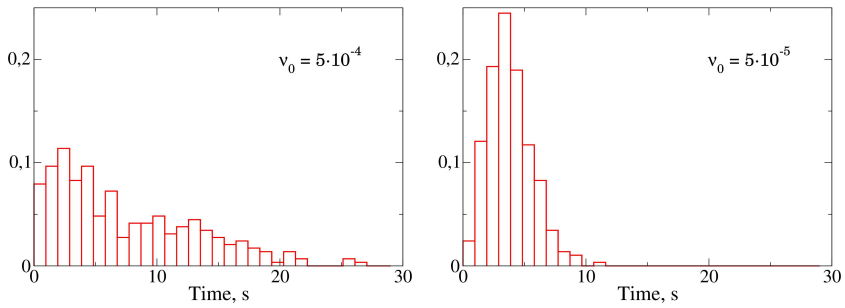

Figure 4.17: Histograms for the lifetime of the filament rings. Time is measured until the first fragment disassembles. Rings with $\nu_0 = 5{\cdot}10^{-3}$ can remain intact for much longer times, so there is no accurate data.

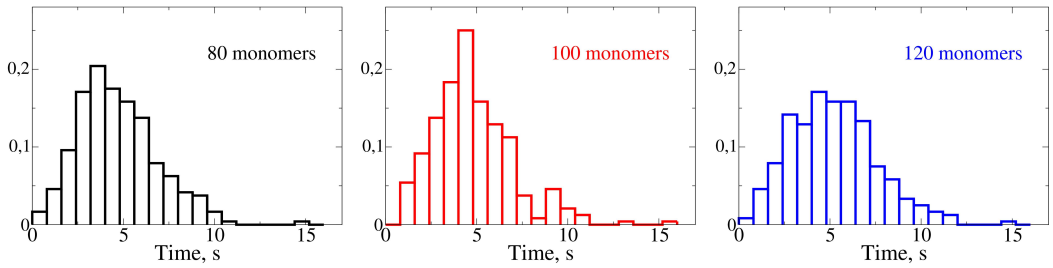

Figure 4.18: Filament rings lifetimes for three different lengths. The average values are 5.22 s for 80 monomers, 4.82 s for 100 monomers and 4.71 s for 120 monomers. $\nu_0 = 5{\cdot}10^{-3}$.

the square lattice is a big constrain when analysing ring breaking, specially for the initial fragmentation event that determines the ring lifetime. In a simulation which allows curvature a single broken bond can result in the opening of the ring (as an open filament with equal length), however, in a square lattice (where the ring is a filament which ends are connected by the boundary conditions) two bonds need to break for a fragment to separate from the ring (which results in two shorter filaments).

4.3 Discusion

This chapter presents a model for FtsZ that includes hydrolysis dynamics. The use of simulated FRET fluorescence allowed qualitative comparison with the results from reference [29]. However, the computational model makes it possible to track information that cannot be observed experimentally. A modification of the FRET labels permitted to follow the origin of the new monomers of a filament, distinguishing those coming from the same cluster of filaments and those coming from a different cluster. This also revealed the relative importance of the gaseous phase in the dynamics of the mixing of monomers.

Nevertheless, the results have to be taken with caution, since the use of a square lattice with no curvature of the filaments is a serious limitation. In principle curvature should not be too important when studying the dynamics of the bonds and monomer exchange, but it has a big influence on the mobility of the filaments and monomers, which in turn affects monomer exchange. Consider, for example, the fact that a vertical filament and a horizontal filament will not be able to bond, since whole filaments cannot change their orientation. Instead, monomers need

to break free from one of the filaments, then rotate, and then bond to the other filament.

This limitation is perhaps more evident in the experiments with filament ring disassembly. In this case the effect is even more serious since a ring can usually open after the breaking of a single bond, but this is not possible in a square lattice, where a whole fragment needs to disassemble for the filament ring to open. This processes are not equivalent, which is why more complete simulations of ring disassembly where not carried out.

Trying to allow for filament rotation is not trivial from a computational point of view—it would most likely be easier (and more interesting) trying to include hydrolysis dynamics in a fine-grained lattice model like those in chapters 3 and 5.

5

Effects of torsion in single FtsZ filaments

FtsZ filaments are often described as a chain of monomers with a preferred curvature angle and some flexibility around this bending value. Recently, the idea of a twist in the filaments started being considered by different groups [30, 31, 32]. In this chapter we will explore this possibility and see what consequences it could have in the experiments and the Z-ring dynamics.

Before the idea of torsion was adopted, there were some experimental results which could not be fully understood. A good example is given in [33]. In this paper, Hamond et al. present AFM images of FtsZ filaments on mica, and they find clear coexistence of straight and curved filaments (see Figure 5.1). At first one could interpret this as the natural flexibility of the filaments around their preferential curvature, however, when the distribution of angles is plotted the result is far from the expected Gaussian curve 5.2.

Another explanation could be that straight filaments are a consequence of GTP bonds, while GDP bonds produce curved filaments. The problem with this argument is that most filaments are either completely straight or completely curved, but in the time scales of the images (~30 s) hydrolysis can be considered "fast", so the GTP/GDP ratio should be approximately uniform in the different filaments. Because there are completely straight and completely curved filaments, it would seem like hydrolysis quickly propagates through filaments instead of happening at random in each bond, but there is no evidence to support that idea yet.

A different approach is to consider torsion and anchoring. Even on a mica surface, where there is no special anchoring technique, it is to be expected that

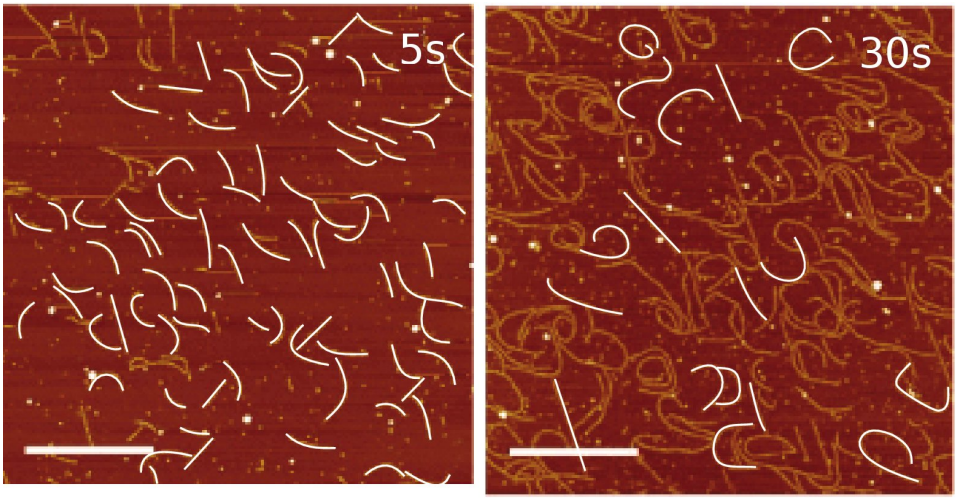

Figure 5.1: AFM images of FtsZ filaments incubated on a mica substrate using an 80 nM FtsZ polymerization buffer [33]. Individual filaments highlighted by I. Hörger.

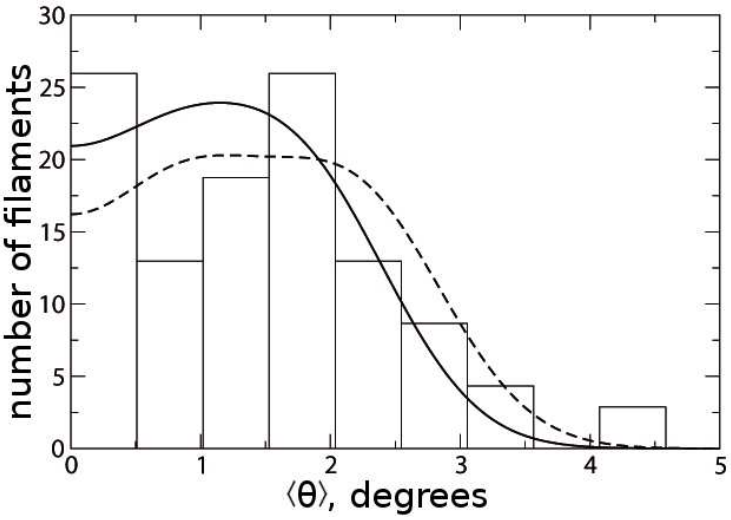

Figure 5.2: Distribution of the number of selected filaments in Figure 5.1, in terms of their mean curvature after an incubation time of 5 s. The lines represent the predictions of the physical pendulum model for a mixed population of filaments in two local minima of the torsion–anchorage free energy (described in detail in section 4 of the ESI, reference [**?**], an almost identical model to the analytical study explained here in section 5.1). Solid line assumes a mean on-plane angle $\theta = 2°$, and $\theta = 2,4°$ for the broken line. [35, 34].

FtsZ monomers will have an specific orientation that maximizes the interaction with the substrate. If this is true, every monomer on a filament should be close to this specific angle relative to the substrate, but if the filament has a natural twist, this will not be possible. There is a competence between the tendency to form twisted filaments and to form well-anchored filaments. Of course, for every length there will be an optimal configuration, but real filaments can be trapped in meta-stable options, thus explaining the coexistence of straight (in this case, well twisted) and curved (well anchored) filaments.

5.1 Analytical study of filaments with anchoring and torsion

If we use an analytic approximation for the torsion and anchoring interactions we can explore the different configurations for filaments of different lengths and their respective energies.

Taking $\varphi(x)$ to be the anchoring angle along the length of the filament (x), our anchoring potential will be

$$U_a = M\left(\varphi(x)\right) = \frac{\gamma}{2}\left[\left(\frac{\varphi(x)}{\Delta}\right)^2 - 1\right] = \frac{\gamma}{2\Delta^2}\left[\varphi(x)^2 - \Delta^2\right] \tag{5.1}$$

which is a parabola that crosses $U_a = 0$ at $\varphi(x) = \pm\Delta$. Whenever $U_a > 0$ we shall take $U_a = 0$.

For the energy of the torsion of the bond we will use

$$U_t = \frac{\kappa}{2}\left(\varphi'(x) - \psi_0\right)^2. \tag{5.2}$$

ψ_0 is the spontaneous twist. Since φ represents the anchoring angle, its derivative φ' is the difference in anchoring angle, that is, the torsion of the bond.

We then have the energy of the filament

$$U\left[\varphi(x)\right] = \int_{-L/2}^{L/2} dx\left[M\left(\varphi(x)\right) + \frac{\kappa}{2}\left(\varphi'(x) - \psi_0\right)^2\right]. \tag{5.3}$$

We derive the Euler–Lagrange equation

$$\mathscr{L} = M\left(\varphi(x)\right) + \frac{\kappa}{2}\left(\varphi'(x) - \psi_0\right)^2 = \mathscr{L}\left(\varphi(x), \varphi'(x), x\right) \tag{5.4}$$

$$\frac{\partial \mathscr{L}}{\partial \varphi} - \frac{d}{dx}\frac{\partial \mathscr{L}}{\partial \varphi'} = 0 = M'\left(\varphi(x)\right) - \frac{d}{dx}\left(\kappa\left(\varphi'(x) - \psi_0\right)\right) \tag{5.5}$$

and we find

$$\kappa\varphi''(x) = M'\left(\varphi(x)\right). \tag{5.6}$$

with the boundary condition

$$\kappa\left(\varphi'(x) - \psi_0\right)\Delta\varphi(x)\Big|_{-L/2}^{+L/2} = 0. \tag{5.7}$$

We can make the analogy with a movement equation ($x \to t$, $k \to m$) to find an "energy" which will be conserved:

$$E = \frac{1}{2}\kappa\left(\varphi'(x)\right)^2 - M\left(\varphi(x)\right). \tag{5.8}$$

If we differentiate E with respect to x, we find eq. 5.6, so E is conserved along x. Now we can use the specific function for the anchoring potential M:

$$M\left(\varphi(x)\right) = \begin{cases} M_1 = \frac{\gamma}{2\Delta^2}\left[\varphi(x)^2 - \Delta^2\right] & \left|\varphi(x)\right| \le \Delta \\ M_2 = 0 & \left|\varphi(x)\right| > \Delta \end{cases} \tag{5.9}$$

The conditions are periodic for $\varphi \to \varphi \pm 2\pi$.
For the first potential we have

$$M_1'\left(\varphi(x)\right) = \frac{\gamma}{\Delta^2}\varphi(x)\,;\,0. \tag{5.10}$$

Using this in eq. 5.6

$$\varphi''(x) = \frac{M_1'}{\kappa} = \frac{\gamma\varphi(x)}{\kappa\Delta^2} = \alpha^2\varphi(x) \tag{5.11}$$

where $\alpha = \sqrt{\frac{\gamma}{\kappa\Delta^2}}$. The solution to eq. 5.11 is

$$\varphi(x) = A\sinh(\alpha x). \tag{5.12}$$

And from eq. 5.7,

$$\varphi'\left(\pm\frac{L}{2}\right) = \psi_0 = A\alpha\cosh\left(\alpha\frac{L}{2}\right), \tag{5.13}$$

$$\frac{L}{2} = \frac{1}{\alpha}\cosh^{-1}\left(\frac{\psi_0}{\alpha A}\right) \equiv \delta(A) \tag{5.14}$$

for

$$0 \leq A \leq \frac{\psi_0}{\alpha}, \tag{5.15}$$

which covers L from 0 to ∞.

We can also use $\varphi(x)$ to find the value for E, which will be conserved along the filament (even for $|\varphi(x)| > \Delta$)

$$E = \frac{\gamma}{2}\left(\frac{A^2}{\Delta^2} + 1\right). \tag{5.16}$$

The solution given for $\varphi(x)$ is valid as long as $|\varphi(x)| \leq \Delta$, so it can cover the length of the filament provided

$$\Delta \geq \varphi\left(\frac{L}{2}\right) = A\sinh\left(\alpha\frac{L}{2}\right) \tag{5.17}$$

Dividing eq. 5.17 and eq. 5.13 we get

$$\frac{L}{2} \leq \lambda_0 = \frac{1}{\alpha}\tanh^{-1}\left(\frac{\alpha\Delta}{\psi_0}\right). \tag{5.18}$$

Where $M = M_2$ we have $\kappa\varphi''(x) = M_2'(\varphi(x)) = 0$, so $\varphi_2'(x) = B$ is constant. We know it has to satisfy

$$\varphi'\left(\pm\frac{L}{2}\right) = \psi_0$$

$$E = \frac{1}{2}\kappa\left(\varphi'(x)\right)^2 - M\left(\varphi(x)\right) = \text{constant} = \frac{\gamma}{2}\left(\frac{A^2}{\Delta^2} + 1\right).$$

Substituting eq. 5.13 in eq. 5.17 (using $\cosh^2(x) - \sinh^2(x) = 1$) yields

$$\varphi\left(\frac{L}{2}\right) = \frac{1}{\alpha}\sqrt{\psi_0^2 - (\alpha A)^2} \leq \Delta$$

$$A^2 \geq \left(\frac{\kappa\psi_0^2}{\gamma} - 1\right)\Delta^2 \tag{5.19}$$

and using this in eq. 5.16,

$$E = \frac{1}{2}\kappa\left(\varphi'(x)\right)^2 - M\left(\varphi(x)\right) \geq \frac{1}{2}\kappa\psi_0^2. \tag{5.20}$$

A smooth connection between $\varphi_1(x)$ and $\varphi_2(x)$ at $\varphi(x) = \Delta$ implies

$$\varphi(x) = \Delta = A\sinh(\alpha x) \tag{5.21}$$

$$\varphi'(x) = B = \alpha A\cosh(\alpha x), \tag{5.22}$$

and this happens for

$$x = \lambda(A) = \frac{1}{\alpha}\sinh^{-1}\left(\frac{\Delta}{A}\right). \tag{5.23}$$

Using again the fundamental relation $\cosh^2(x) - \sinh^2(x) = 1$ we get

$$B = \alpha\sqrt{\Delta^2 + A^2}. \tag{5.24}$$

From eq. 5.20 we have $\varphi_2'(x) \equiv B \geq \psi_0$ (because $M_2 = 0$). In general the filament cannot have ends while in this region ($\left|\varphi(x)\right| > \Delta$, periodic for $\varphi \to \varphi \pm 2\pi$, green in Figure 5.3). Remembering the analogy with a movement equation ($x \to t$, $k \to m$) where constant speed yields $t = s/v$, we have that the length of this plateau of constant torsion is

$$\Delta x_2 = \frac{2\pi - 2\Delta}{B}. \tag{5.25}$$

In Figure 5.3 there is an schematic representation of $\varphi'(x)$ as a function of the length, x, showing the meaning of $\delta(A)$, $\lambda(A)$, B and the plateau where M_2 applies.

With equation 5.3 in mind, we can now evaluate the energy of a filament for the different sections in Figure 5.3.

Using the boundary condition in eq. 5.7 we derive the expression for the torsion contribution:

$$\begin{aligned}\int_0^y dx\,\tfrac{\kappa}{2}\left(\varphi'(x) - \psi_0\right)^2 &= \tfrac{\kappa}{2}\left[\alpha^2 A^2\left(\tfrac{\sinh(\alpha y)\cosh(\alpha y)}{2\alpha} + \tfrac{y}{2}\right)\right. \\ &\quad \left. -2\psi_0 A\sinh\left(\alpha y\right) + \psi_0^2 y\right]\end{aligned} \tag{5.26}$$

and we will be interested in the special cases

$$y = \lambda(A)$$

$$y = \delta(A)$$

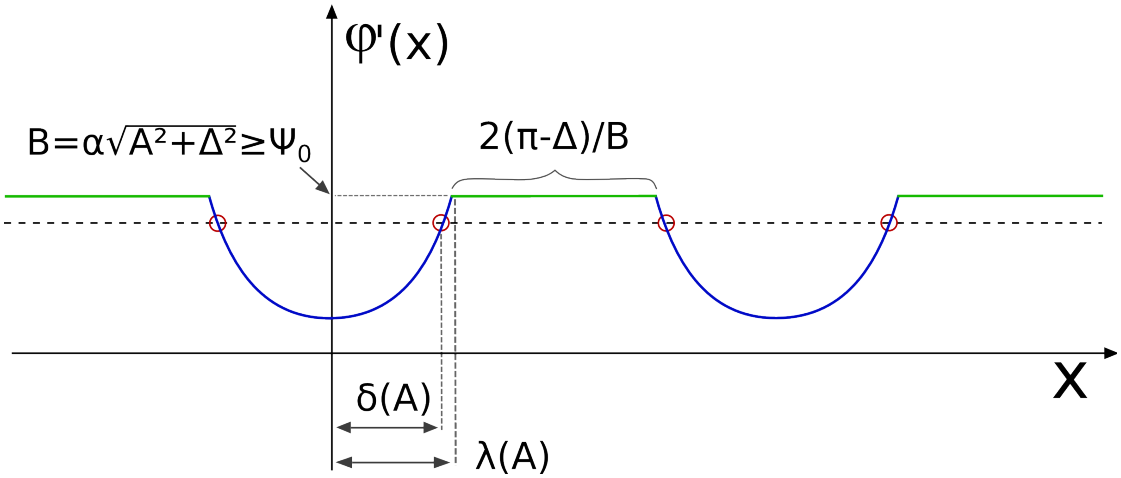

Figure 5.3: Schematic representation of the filament torsion ($\varphi'(x)$) *versus* its length (x). The red circles mark where $\varphi'(x) = \psi_0$, which are the different possible ends of the filament ($x = \pm\frac{L}{2}$).

Of course, this is only true when $|\varphi(x)| < \Delta$, otherwise we have $\varphi'(x) = B = \alpha\sqrt{\Delta^2 + A^2}$ (remember eq. 5.24), so

$$\int dx \frac{\kappa}{2}(B-\psi_0)^2 = \frac{\kappa}{2}(B-\psi_0)^2 \Delta x \tag{5.27}$$

and using eq. 5.25

$$\int dx \frac{\kappa}{2}(B-\psi_0)^2 = \kappa(B-\psi_0)^2 \frac{\pi-\Delta}{B} = \frac{\pi-\Delta}{B}\kappa\left(\alpha\sqrt{\Delta^2+A^2}-\psi_0\right)^2 \tag{5.28}$$

Similarly, we have the anchoring contribution:

$$\int_0^y dx \frac{\gamma}{2}\left(\frac{\varphi^2(x)}{\Delta^2}-1\right) = \frac{\gamma}{2\Delta^2}A^2\left(\frac{\sinh(\alpha y)\cosh(\alpha y)}{2\alpha}-\frac{y}{2}\right)-\frac{\gamma}{2}y \tag{5.29}$$

Finally, given that the ends of the filament need be at $\delta(A)$, we can consider three different general solutions:

I) $n = 0$  $= 2\delta(A)$

II) $n = 0$  $= 2(\lambda(A) - \delta(A)) + \frac{2(\pi-\Delta)}{B}$

III) $n = 1$ 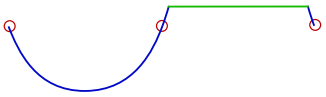 $= 1\,\text{period} = 2\lambda(A) + \frac{2(\pi-\Delta)}{B}$

and, of course, any of them plus a given number of periods.

From this analysis we obtain the graph in Figure 5.4. We can see how for each length there are different possible arrangements involving a different number of turns. But of course a more realistic scenario will involve a dynamic length (filaments break and grow), so a filament can be found in a configuration that is no longer optimal for its new length value. Because changes in configuration involve a rearrangement of all its monomers, metastable solutions arise. This may explain at a qualitative level how we can see at the same time straight and curved filaments for similar lengths.

Hörger and Tarazona worked out a similar analytical study ([35], [34] supplementary material) with a different anchoring potential—a sinusoidal curve instead of a parabola with a maximum allowed value. Although the mathematical details differ, the results are quite similar, in particular, they also find metastable solutions for different torsion turns.

5.2 MD and ideal filaments

The analytical study which opens this chapter shows how torsion could qualitatively explain the coexistence of straight and curved filaments, or how it could be involved in the ellipticity of FtsZ rings. However, the model used in the analysis did not have a strong experimental support. In this section we will develop a model for anchoring and torsion of FtsZ filaments based on Molecular Dynamics (MD) simulations of short FtsZ filaments.

MD is a powerful tool to explore the dynamic properties of big molecules or small assemblies with many atoms. Computational limitations require re-

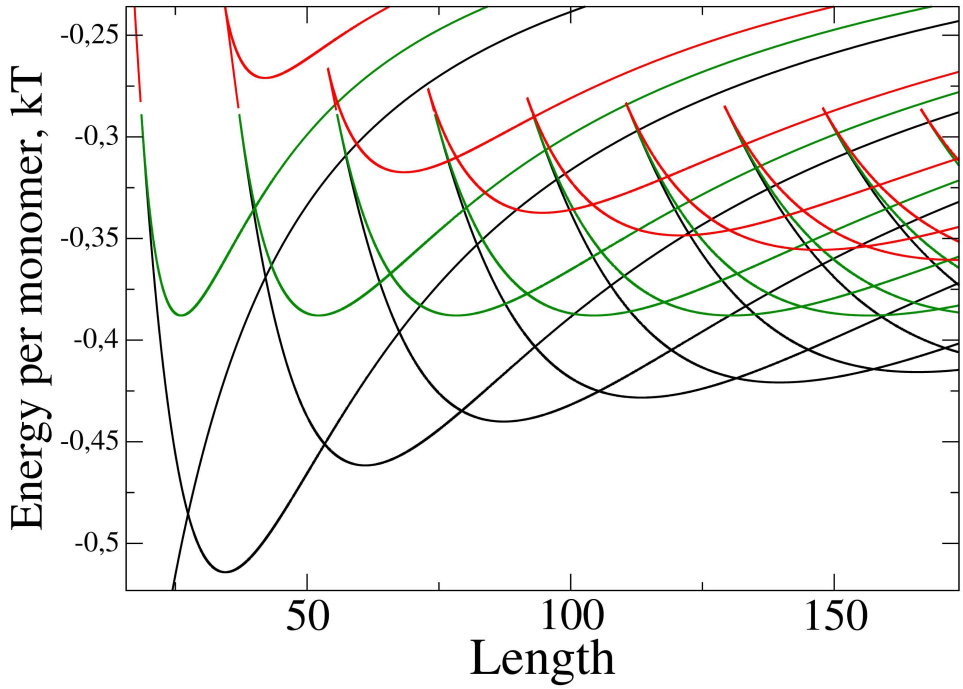

Figure 5.4: Energy per monomer as a function of the number of monomers in the filament, for solutions of kind I (black), II (red) and III (green). Lines from left to right represent increasing number of full filament turns. The first black line has a minimum at –1. $\Delta = 90°$, $\psi_0 = 15°$, $\beta\gamma = 2$, $\beta\kappa = 25/\text{rad}^2$.

searchers to look for the smaller system that captures the essence of the problem, for example, if considering the binding of a molecule to a DNA strand, it would be unintelligent, if not impossible, to include the whole DNA strand in the simulation; a shorter sequence has to be used instead.

If we are interested in the properties of a protein filament, having only two beads in the chain can be problematic, even so, computational limitations and the sacrifice of collective effects in favor of longer simulations limited FtsZ MD simulations to dimers. Luckily for us, Martín-García et al. recently conducted a series of MD simulations of very short FtsZ filaments (up to a pentamer) to explore whether the edges of a filament have a different GTPase activity [36]. Although this was not the goal of their research, they did find torsion in their simulations. Afterwards, they performed a new series of simulations specifically intended to explore the torsion and bending angles of the FtsZ bond and provide us with data upon which we could base our model. Because there is no crystal structure of a FtsZ pentamer, the three-dimensional model was constructed by successive structural alignment of the two FtsZ subunits of the previously published MD-equilibrated *Methanococcus jannaschii* FtsZ dimer [37], in the

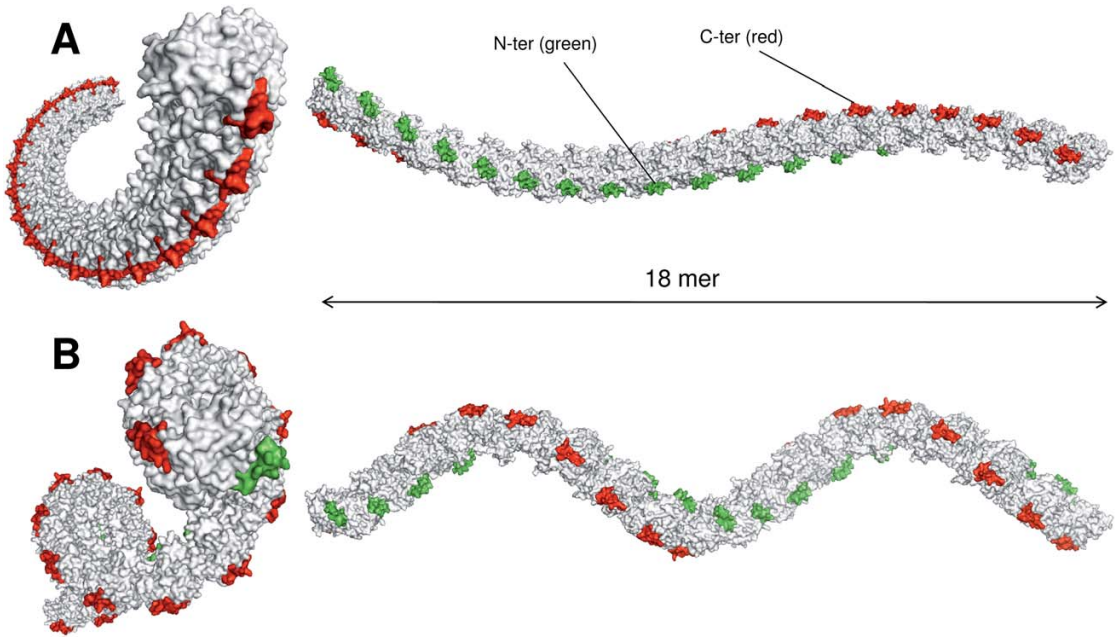

Figure 5.5: Structural models for FtsZ polymers in solution. (A) Longitudinal elongation of the crystallized structure of an FtsZ dimer. Residues located at the N-ter (green) and C-ter (red) ends of the crystal structure are highlighted. (B) Longitudinal elongation of an FtsZ pentamer after 8 nanoseconds of unrestricted molecular dynamics [34].

presence of Mg^{++}, GTP and K^{+} in the active centre (Figure 5.5 A). Unrestricted MD simulations for the pentamer covered as long as 80ns, and the filament relaxes to a more contracted structure (Figure 5.5 B). More detail on the MD procedure can be found in [34].

In order to characterize the filament we used the data from a 40ns simulation (Fig. 5.7). The first 13.3ns were not used in the analysis to account for the thermalisation of the system. The bending of the FtsZ pentamer is measured by the angle α, calculated between the directions of the lines from the first to the third, and from the third to the fifth monomer, so that it corresponds to the bending angles in two consecutive bonds $\alpha = \pi - \theta_1 - \theta_2$. The mean value was $\langle\theta\rangle \equiv \langle\theta_{1,2}\rangle \simeq 7,6°$ for the angle between neighbor monomers. The observed fluctuations of α correspond to two consecutive bonds, that we take as independent from each other, $\langle\theta_1\theta_2\rangle = \langle\theta_1\rangle\langle\theta_2\rangle$, so that $\Delta\alpha \equiv \sqrt{\langle\alpha^2\rangle - \langle\alpha\rangle^2} \simeq 3,4°$ corresponds to $\Delta\theta \equiv \sqrt{\langle\theta^2\rangle - \langle\theta\rangle^2} = \Delta\alpha/\sqrt{2} \simeq 2,4°$. The angle ψ measures the orientation mismatch between two consecutive monomers with respect to the axis joining their bonding sites.

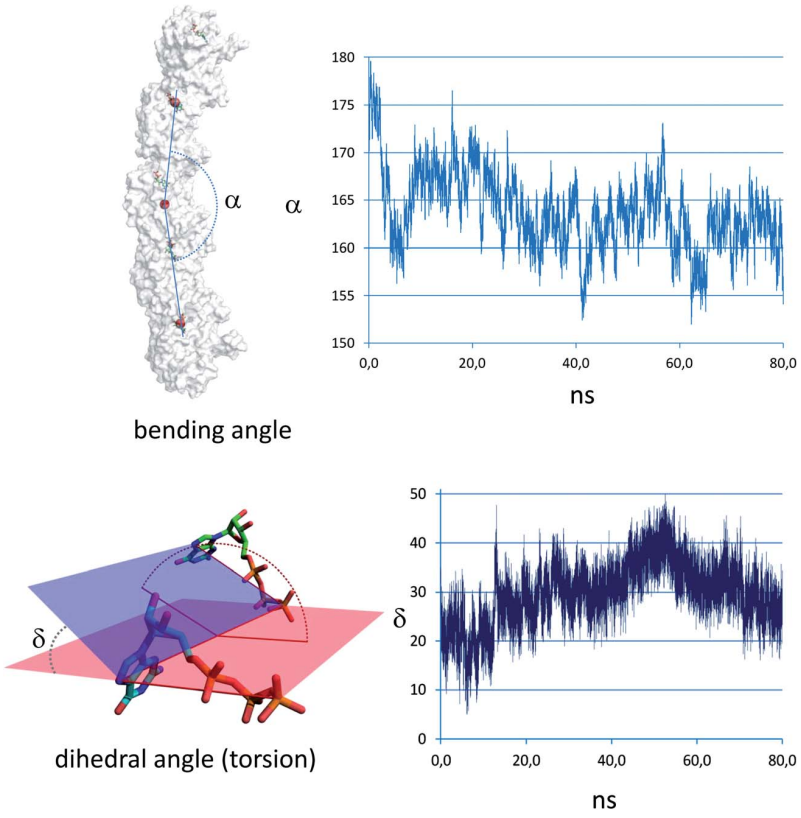

Figure 5.6: Fluctuations on the curvature and torsion angles during 80ns of unrestricted molecular dynamics. Bending angle α was measured using as references the center of masses for the third monomer and the position of the GTP molecules in the first and last interfaces. Torsion angle δ (ψ in this text) was measured using as references the position of atoms in the GTP molecule, as indicated in the lower left diagram [34].

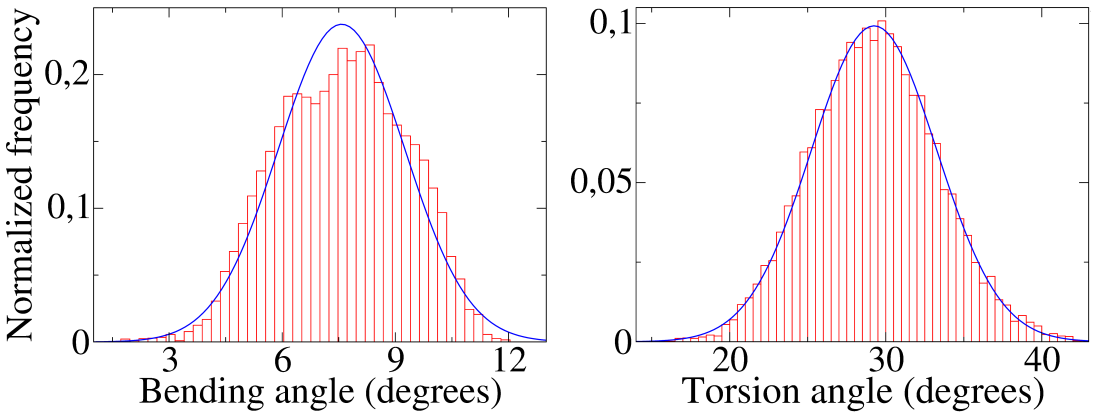

Figure 5.7: Histograms and Gaussian fits for the distribution of bending, $(\pi - \alpha)/2$, and torsion (ψ) angles obtained from a 40 ns MD simulation. The data for the first 13.3 ns is not considered, to allow for the thermalization of the system [34].

We find $\langle\psi\rangle \simeq 29°$, and $\Delta\psi \equiv \sqrt{\langle\psi^2\rangle - \langle\psi\rangle^2} \simeq 4°$. These mean values and mean fluctuations may be taken with a confidence of about $\pm 0,5°$, from the possible changes if we analyse the simulation results over time intervals with ± 1 nanoseconds. See Figure 5.6 for raw data of bending and torsion of a longer simulation (80ns), and Figure 5.7 for the histograms used to obtain the values described above.

The angular fluctuations observed in the simulation may be used to estimate the flexibility of the filaments. Assuming that the MD run is a good sample of thermal equilibrium, the elastic constants that describe the bending and the torsion of the filament, $\kappa_\theta = \kappa_B T/\Delta\theta^2$ and $\kappa_\psi = \kappa_B T/\Delta\psi^2$, can be used to describe the energy of a bond with bending and torsion angles θ and ψ close to $\langle\theta\rangle$ and $\langle\psi\rangle$:

$$U = -U_b + \sum_{i=1}^{N} \left[\frac{\kappa_\theta}{2} (\theta_i - \langle\theta\rangle)^2 + \frac{\kappa_\psi}{2} \left(\psi_i - \langle\psi\rangle\right)^2 \right], \tag{5.30}$$

where U_b is the free energy of the bond in the optimal (helical) structure. The estimated values $\beta\kappa_\theta \simeq 583/\text{rad}^2$ and $\beta\kappa_\psi \simeq 200/\text{rad}^2$ indicate that filament torsion is about three times more flexible than filament bending.

In order to estimate the persistence length of the filaments described by the MD results, we created filaments with the same bending and torsion angles distribution as the MD simulations (Figure 5.8) and analyse the correlation between the orientation of their ends, as seen in Figure 5.9. The persistence length for the helical axis of a free filament, with these elastic constants, would be about $5\,\mu$m (i.e. above one thousand monomers), which is consistent with some previously estimated values, but larger than other estimations [27, 43]. The specific value is likely to be conditioned by the experimental technique used to do the measurements: results obtained from cryoelectron microscopy give a slightly smaller value, $1,5 \pm 0,25\,\mu$m, whereas the persistence length estimated from transmission electron microscopy images is only 180 nm; it is possible that the negative stain used in the sample preparation for TEM can affect the rigidity and length of the filaments adsorbed on the carbon grid.

We can use the parametric description of a helix to acquire further insight into the filament shape described by the MD simulations.

Figure 5.8: Two different views of a filament built with the bending and torsion angles distributions from the MD simulations.

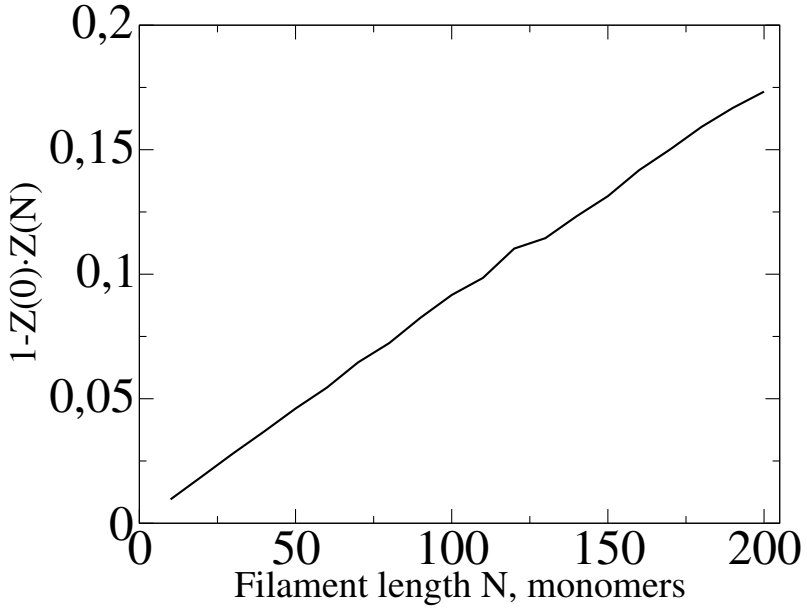

Figure 5.9: Correlation of the orientation of the ends of a free FtsZ filament as a function of its length. The results show an average of 1000 different filaments for each length.

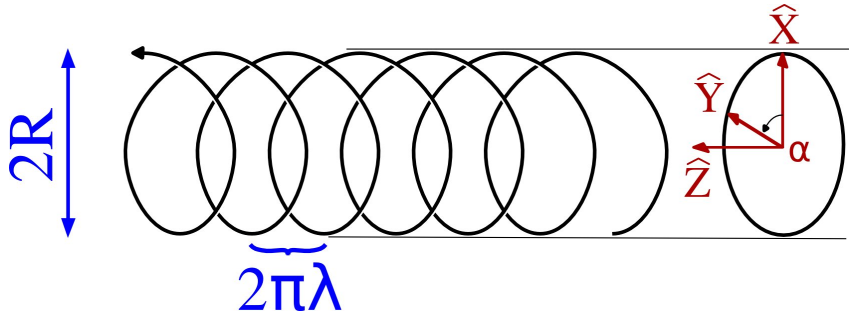

$$r(\alpha) = (R\cos\alpha, R\sin\alpha, \lambda\alpha) \tag{5.31}$$

As the picture above illustrates, the helical axis lies along the Z direction and the angle α is measured around that axis. The parameters R and λ give the cylindrical radius and the screw thread of the helix, respectively.

Because $dS = \sqrt{R^2+\lambda^2}\,d\alpha$,

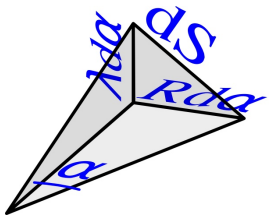

the tangent vector at any point of the helix is

$$\vec{T} \equiv \frac{d\vec{r}}{dS} = \frac{\partial\vec{r}}{\partial\alpha}\frac{d\alpha}{dS} = \frac{1}{\sqrt{R^2+\lambda^2}}(-R\sin\alpha, R\cos\alpha, \lambda)\,. \tag{5.32}$$

Another derivative gives the change in the tangent vector, i.e. the curvature of the helix:

$$\vec{T}' = \frac{d\vec{T}}{dS} = \frac{R}{\sqrt{R^2+\lambda^2}}(-\cos\alpha, -\sin\alpha, 0) = \rho\vec{N}, \tag{5.33}$$

from where the constant main curvature

$$\rho = \frac{R}{\sqrt{R^2+\lambda^2}}. \tag{5.34}$$

The change in the tangent plane will give us the torsion of the helix:

$$\vec{B} = \vec{T}x\vec{N} = \frac{1}{\sqrt{R^2+\lambda^2}}(\lambda\sin\alpha, -\lambda\cos\alpha, R) \tag{5.35}$$

$$\vec{B}' = \frac{d\vec{T}}{dS} = \frac{\lambda}{\sqrt{R^2+\lambda^2}}(\cos\alpha, \sin\alpha, 0) = -\tau\vec{N}, \tag{5.36}$$

and so the torsion is

$$\tau = \frac{\lambda}{\sqrt{R^2+\lambda^2}}. \tag{5.37}$$

We can keep track of the Z axis using the relation

$$\vec{Z} = \frac{\lambda\vec{T} + R\vec{B}}{\sqrt{\lambda^2+R^2}}, \tag{5.38}$$

which will be useful in the study of the persistence length (Figure 5.9).

Finally, we want to relate these equations to the information we receive from the MD simulations. Given the small size of the monomers ($d \simeq 4,5$ nm), we can approximate the derivative for the curvature

$$\rho = \left|\frac{d\vec{T}}{dS}\right| \simeq \left|\frac{\vec{T}(d) - \vec{T}(0)}{d}\right| = \frac{\langle\theta\rangle}{d} \simeq 0,029\,\mathrm{nm}^{-1}. \tag{5.39}$$

If we forget about torsion, this describes a ring with radius $1/\rho \simeq 34$ nm, about 50 monomers.

In a similar way,

$$\tau \simeq \frac{\langle\psi\rangle}{d} \simeq 0,11\,\mathrm{nm}^{-1}. \tag{5.40}$$

The result, as seen in Figure 5.8, is a very stretched helix. If we consider the projected radius, $R \simeq 2,2$ nm, and account for the monomer size, the FtsZ helix would fit into a cylinder of around $3d \simeq 13$ nm, quite narrow compared with the typical length of the filament, in the range of microns. A full round of the helix is completed over a distance $2\pi\lambda \simeq 51,9$ nm measured along the cylinder (Z) axis, and about 11,88 monomers or 53,45 nm measured along the helix (remember $dS = \sqrt{R^2+\lambda^2}d\alpha$). This could explain why the helicity of the filament is not obvious from the experimental point of view; with suboptimal resolution a filament like that in Figure 5.8 may not reveal its sinusoidal shape, but may rather look like a straight, somewhat wiggly filament. The gaussian fluctuations of θ and ψ produce changes in the local curvature and torsion, i.e. deformations of the helical structure. The parameters R and λ will fluctuate both with time and position. Given the stretched aspect of the helix, the most visible effect would be the fluctuation in the direction of the helical axis, i.e. in the global shape of the filament, that would fluctuate like a filament without any spontaneous curvature and showing a persistence length in the range of microns. We can

conclude that, although helicity may play a role in FtsZ dynamics, it may be difficult to find (or disprove) this helicity by direct observation of the filaments in most circumstances, so an indirect approach could be more convenient (see, for example, [32]).

Filaments on a surface: mathematical description

So far in this section we have characterized free FtsZ filaments, or filaments in a solution. But our experimental data from AFM experiments describe filaments that are attached to a surface, therefore, we have to answer the question of how this anchoring to a plane will affect the free filaments of the MD simulations, and what structures we are expecting to find in our AFM experiments.

We will consider monomers with two interfaces ("–" and "+"). These interfaces will form an angle so that a bond between two of these monomers will have a curvature $\langle\theta\rangle$. Assuming for an instant there is no torsion in the bond, the monomer would look something like this: 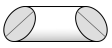

When torsion is considered, the interfaces will be shifted along the monomer long-axis, so that the bond is twisted.

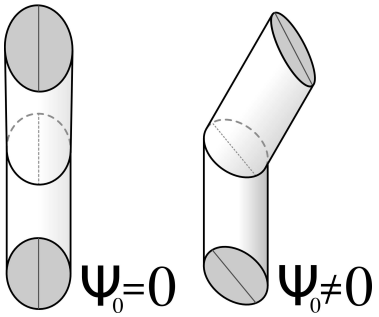

Let $\vec{t}$ be the direction of the monomer, $\vec{b}$ giving the direction of curvature (if $\langle\psi\rangle = 0$) and $\vec{n} = \vec{b}\wedge\vec{t}$, as shown in the picture:

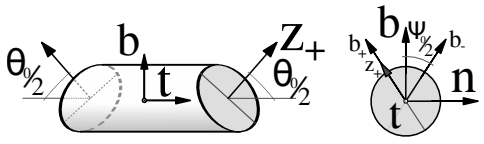

Figure 5.10: Mathematical description of a free monomer.

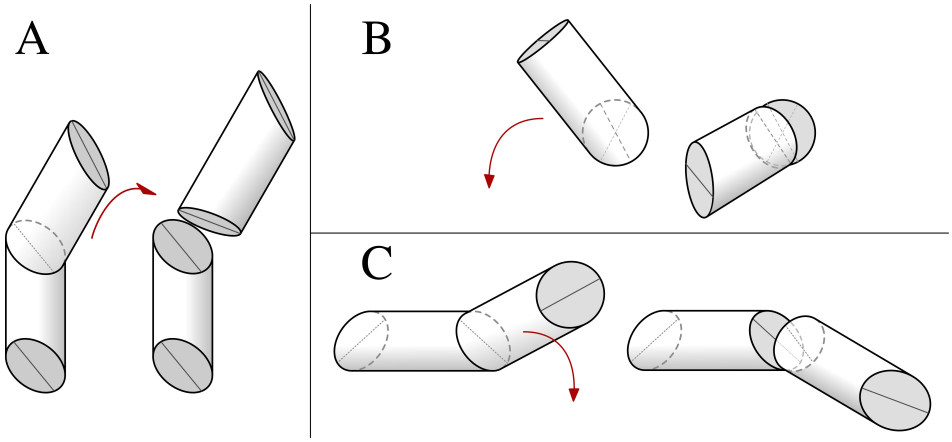

Figure 5.12: Sketch showing how a bond between free monomers has to adapt when both monomers are forced to stay on the same plane. **A** represents the top view, **B** the front view and **C** the side view.

$\vec{z}_+$ and $\vec{z}_-$ are normal to the interfaces. $\vec{b}_+$ and $\vec{b}_-$ define the orientation of the interfaces relative to $\vec{b}$. For any given bond we can say that its energy is given by

$$U = -U_b + \kappa_\delta(1 - \vec{b}_+ \cdot \vec{b}'_-) + \kappa_\theta(1 + \vec{z}_+ \cdot \vec{z}'_-). \tag{5.41}$$

Remember $\kappa_\theta = \kappa_B T/\Delta\theta^2$ and $\kappa_\psi = \kappa_B T/\Delta\psi^2$. Now all of our monomers will be attached to a surface defined by the local vectors $\vec{u}$ and $\vec{v}$, with $\vec{v}$ normal to the surface and $\vec{u} = \vec{t} \wedge \vec{v}$.

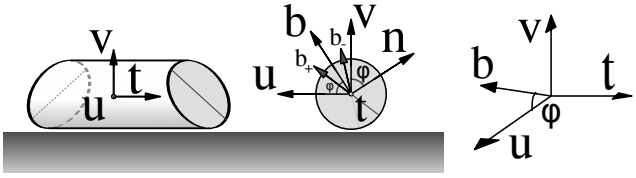

Figure 5.11: Monomer relative to a surface.

For convenience, we will consider $\langle\theta\rangle = \theta_0$, $\langle\psi\rangle = \psi_0$. We can write

$$\begin{aligned}
\vec{b} &= \cos(\varphi)\,\vec{u} + \sin(\varphi)\,\vec{v} \\
\vec{n} &= -\sin(\varphi)\,\vec{u} + \cos(\varphi)\,\vec{v} \\
\vec{b}_+ &= \cos\left(\varphi + \tfrac{\psi_0}{2}\right)\vec{u} + \sin\left(\varphi + \tfrac{\psi_0}{2}\right)\vec{v} \\
\vec{b}_- &= \cos\left(\varphi - \tfrac{\psi_0}{2}\right)\vec{u} + \sin\left(\varphi - \tfrac{\psi_0}{2}\right)\vec{v}
\end{aligned} \tag{5.42}$$

The two last vectors, $\vec{b}_+$ and $\vec{b}_-$, will be useful to express $\vec{z}_+$ and $\vec{z}_-$:

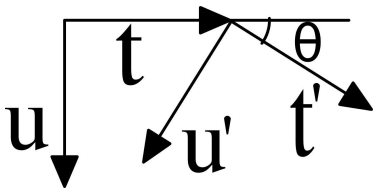

Figure 5.13: Top view of the local vectors defining the substrate plane and monomer direction in a monomer–monomer bond. Vector $\vec{n}$=$\vec{n'}$, perpendicular to both $\vec{t}$ and $\vec{u}$ is not shown.

$$\begin{aligned}
\vec{z}_+ &= \cos\left(\tfrac{\theta_0}{2}\right)\vec{t} + \sin\left(\tfrac{\theta_0}{2}\right)\vec{b}_+ \\
&= \cos\left(\tfrac{\theta_0}{2}\right)\vec{t} + \sin\left(\tfrac{\theta_0}{2}\right)\left(\cos\left(\varphi + \tfrac{\psi_0}{2}\right)\vec{u} + \sin\left(\varphi + \tfrac{\psi_0}{2}\right)\vec{v}\right) \\
\vec{z}_- &= -\cos\left(\tfrac{\theta_0}{2}\right)\vec{t} + \sin\left(\tfrac{\theta_0}{2}\right)\vec{b}_- \\
&= -\cos\left(\tfrac{\theta_0}{2}\right)\vec{t} + \sin\left(\tfrac{\theta_0}{2}\right)\left(\cos\left(\varphi - \tfrac{\psi_0}{2}\right)\vec{u} + \sin\left(\varphi - \tfrac{\psi_0}{2}\right)\vec{v}\right)
\end{aligned} \tag{5.43}$$

Remember, from eq. 5.41, we need $\vec{z}_+ \cdot \vec{z}'_-$ and $\vec{b}_+ \cdot \vec{b}'_-$ to compute the energy of a bond. The second is easy enough

$$\vec{b}_+ \cdot \vec{b}'_- = \cos\left(\varphi - \varphi' + \psi_0\right). \tag{5.44}$$

From Figure 5.13 we have

$$\begin{aligned}
\vec{t}' \cdot \vec{t} &= \cos\theta \\
\vec{u}' \cdot \vec{u} &= \cos\theta \\
\vec{v}' \cdot \vec{v} &= 1 \\
\vec{t}' \cdot \vec{u} &= \sin\theta \\
\vec{u}' \cdot \vec{t} &= -\sin\theta
\end{aligned} \tag{5.45}$$

Of course, $\vec{v} \cdot \vec{t} = \vec{v} \cdot \vec{u} = \vec{v} \cdot \vec{t}' = \ldots = 0$. With these results,

$$\begin{aligned}\vec{z}_+\cdot\vec{z}'_- &= -\cos^2\left(\tfrac{\theta_0}{2}\right)\cos\theta+\sin^2\left(\tfrac{\theta_0}{2}\right)\cos\left(\varphi+\tfrac{\psi_0}{2}\right)\cos\left(\varphi'-\tfrac{\psi_0}{2}\right)\cos\theta\\ &\quad+\sin^2\left(\tfrac{\theta_0}{2}\right)\sin\left(\psi+\tfrac{\delta_0}{2}\right)\sin\left(\varphi'-\tfrac{\psi_0}{2}\right)\\ &\quad-\cos\left(\tfrac{\theta_0}{2}\right)\sin\left(\tfrac{\theta_0}{2}\right)\cos\left(\varphi+\tfrac{\psi_0}{2}\right)\sin\theta\\ &\quad-\cos\left(\tfrac{\theta_0}{2}\right)\sin\left(\tfrac{\theta_0}{2}\right)\cos\left(\varphi'-\tfrac{\psi_0}{2}\right)\sin\theta\end{aligned}\quad , \tag{5.46}$$

and using some well known trigonometry tricks, we arrive at

$$\begin{aligned}\vec{z}_+\cdot\vec{z}'_- &= -\cos\theta\left\{\frac{1-\cos\left(\varphi+\frac{\psi_0}{2}\right)\cos\left(\varphi'-\frac{\psi_0}{2}\right)}{2}+\cos\theta_0\frac{1+\cos\left(\varphi+\frac{\psi_0}{2}\right)\cos\left(\varphi'-\frac{\psi_0}{2}\right)}{2}\right\}\\ &\quad-\sin\theta\sin\theta_0\left\{\cos\left(\varphi+\tfrac{\psi_0}{2}\right)+\cos\left(\varphi'-\tfrac{\psi_0}{2}\right)\right\}\\ &\quad+\tfrac{1-\cos\theta_0}{2}\sin\left(\varphi+\tfrac{\psi_0}{2}\right)\sin\left(\varphi'-\tfrac{\psi_0}{2}\right)\end{aligned} \tag{5.47}$$

It will be useful to substitute

$$\begin{aligned}W &= \cos\left(\varphi+\tfrac{\psi_0}{2}\right)\\ W' &= \cos\left(\varphi'-\tfrac{\psi_0}{2}\right)\end{aligned}\quad , \tag{5.48}$$

so we have

$$\begin{aligned}\vec{z}_+\cdot\vec{z}'_- &= -\tfrac{1}{2}\cos\theta\left[1+\cos\theta_0-(1-\cos\theta_0)\,WW'\right]\\ &\quad-\tfrac{1}{2}\sin\theta\sin\theta_0\left\{W+W'\right\}\\ &\quad+\tfrac{1-\cos\theta_0}{2}\sin\left(\varphi+\tfrac{\psi_0}{2}\right)\sin\left(\varphi'-\tfrac{\psi_0}{2}\right)\end{aligned}\quad , \tag{5.49}$$

which behaves as expected in easier specific situations. For example, if $\varphi=\varphi'=\psi_0=0$ we have

$$\vec{z}_+\cdot\vec{z}'_- = [...] = -\cos\left(\theta-\theta_0\right).$$

If $\varphi=\varphi'=\frac{\pi}{2}$, $\psi_0=0$,

$$\vec{z}_+\cdot\vec{z}'_- = [...] = \frac{1-\cos\theta_0}{2}-\cos\theta\frac{1+\cos\theta_0}{2}.$$

We can use the general result (eq. 5.47/5.49) to find the optimal angle that $\vec{t}$ and $\vec{t}'$ will form for an anchored bond. We will refer to this angle by θ_M, and it is found by minimizing the product $\vec{z}_+ \cdot \vec{z}'_-$.

$$\frac{d}{d\theta}\vec{z}_+ \cdot \vec{z}'_- = 0 \tag{5.50}$$

Note that $\vec{z}_+ \cdot \vec{z}'_-$ takes the form $a\cos\theta + b\sin\theta + c$, so

$$\frac{d}{d\theta}\left[a\cos\theta + b\sin\theta + c\right] = -a\sin\theta + b\cos\theta, \tag{5.51}$$

and the extreme value is given by

$$a\sin\theta_M = b\cos\theta_M \Longrightarrow \tan\theta_M = b/a. \tag{5.52}$$

With the appropriate expressions for the parameters a, b, c in eq. 5.49 we find

$$\tan\theta_M = \frac{\sin\theta_0\left\{W + W'\right\}}{1 + \cos\theta_0 - (1 - \cos\theta_0)\, WW'}. \tag{5.53}$$

Again, we can verify a known situation; for $\varphi = \varphi' = \psi_0 = 0$ eq. 5.53 yields $\tan\theta_M = \tan\theta_0$, as expected.

We noticed before that $\vec{z}_+ \cdot \vec{z}'_-$ takes the form $a\cos\theta + b\sin\theta + c$. We are now interested in transforming $a\cos\theta + b\sin\theta$ into the alternative expression $A\cos(\theta - \alpha) = A\cos\theta\cos\alpha + A\sin\theta\sin\alpha$, so

$$\left.\begin{aligned} a &= A\cos\alpha \\ b &= A\sin\alpha \end{aligned}\right\} \begin{aligned} &\rightarrow \tan\alpha = b/a \\ &\rightarrow A^2 = a^2 + b^2 \end{aligned} \tag{5.54}$$

We have already identified $\tan\alpha = b/a = \tan\theta_M$. We now substitute a and b to get A:

$$4A^2 = \left[1 + \cos\theta_0 - (1 - \cos\theta_0)\, WW'\right]^2 + \sin^2\theta_0\left(W + W'\right)^2, \tag{5.55}$$

which yields

$$A = \frac{1}{2}\left\{(1 + \cos\theta_0)^2 + \left(W^2 + W'^2\right)\sin^2\theta_0 + W^2W'^2\,(1 - \cos\theta_0)^2\right\}^{1/2}. \tag{5.56}$$

It may be useful to note the limits of A,

$$\frac{1+\cos\theta_0}{2} \leq A \leq 1. \tag{5.57}$$

Finally,

$$\vec{z}_+ \cdot \vec{z}'_- = -A\cos(\theta-\theta_M) + \frac{1-\cos\theta_0}{2}\sin\left(\varphi+\frac{\psi_0}{2}\right)\sin\left(\varphi'-\frac{\psi_0}{2}\right), \tag{5.58}$$

or

$$\vec{z}_+ \cdot \vec{z}'_- = -A\cos(\theta-\theta_M) + B. \tag{5.59}$$

For small on-plane deviations ($\theta \simeq \theta_0$, and $\cos\gamma \simeq 1-\frac{\gamma^2}{2}$ for small γ) we have the approximation

$$\vec{z}_+ \cdot \vec{z}'_- \simeq -A + B + \frac{A}{2}(\theta-\theta_M)^2. \tag{5.60}$$

$-A+B$ is the energy needed to take the second monomer of the bond to the surface, while $\frac{A}{2}(\theta-\theta_M)^2$ is the energy needed for on-plane fluctuations of the curvature.

Now we have a useful expression for the energy of a bond when both monomers are attached to the surface. Of course, we need to consider the anchoring potential, that is, the interaction that is actually forcing the monomers to remain on the surface. We will use the same potential we introduced in section 6.1.1, which specific parameter values will depend on the details of the monomer–surface interaction:

$$U_{anchoring} = \min\left[-U_a + \kappa_a\left(\varphi_i-\varphi_0\right)^2,\ 0\right]. \tag{6.1}$$

With all the ingredients we now have

$$U\left(\varphi,\varphi',\theta\right) = -U_b + \kappa_\delta(1-\vec{b}_+\cdot\vec{b}'_-) + \kappa_\theta(1+\vec{z}_+\cdot\vec{z}'_-) + U_{anc}\left(\varphi\right) + U_{anc}\left(\varphi'\right), \tag{5.61}$$

which can be written separating the different contributions:

$$\begin{aligned} U(\varphi,\varphi',\theta) &= \kappa_\psi(1-\cos(\varphi-\varphi'+\psi_0)) \\ &\quad +\kappa_\theta\left[1+B(\varphi,\varphi')-A(\varphi,\varphi')\right] \\ &\quad +\tfrac{\kappa_\theta A(\varphi,\varphi')}{2}\left(\theta-\theta_M(\varphi,\varphi')\right)^2 \\ &\quad +U_{anc}(\varphi)+U_{anc}(\varphi') \end{aligned} \tag{5.62}$$

The first line is the twist of the bond, the second the energy to keep the bond on a surface, the third is the energy for on-plane curvature ($\theta \neq \theta_M$) and the last line is just the anchoring potential for each monomer. For convenience, we will write once again the expression for the new variables we have introduced:

$$A = \frac{1}{2}\left\{(1+\cos\theta_0)^2 + \left(W^2+W'^2\right)\sin^2\theta_0 + W^2W'^2(1-\cos\theta_0)^2\right\}^{1/2} \tag{5.56}$$

$$B = \frac{1-\cos\theta_0}{2}\sin\left(\varphi+\frac{\psi_0}{2}\right)\sin\left(\varphi'-\frac{\psi_0}{2}\right) \tag{5.63}$$

$$\begin{aligned} W &= \cos\left(\varphi+\tfrac{\psi_0}{2}\right) \\ W' &= \cos\left(\varphi'-\tfrac{\psi_0}{2}\right) \end{aligned} \tag{5.48}$$

$$\tan\theta_M = \frac{\sin\theta_0\left\{W+W'\right\}}{1+\cos\theta_0-(1-\cos\theta_0)\,WW'} \tag{5.53}$$

With these equations we can describe two very different limits. On the one hand, we can have $\varphi+\frac{\psi_0}{2} \approx \varphi'-\frac{\psi_0}{2} \approx 0\,\text{rad}$. In this case, the tangential plane of the free helix matches that of the substrate, so the energy required to keep the bond on-plane goes to zero ($B(0,0)=0$, $A(0,0)=1$). The optimal on-plane curvature is, again, that of the free helix ($\theta_M(0,0)=\theta_0$). The opposite limit, $\varphi+\frac{\delta_0}{2} \approx \varphi'-\frac{\psi_0}{2} \approx \frac{\pi}{2}\,\text{rad}$, gives no curvature ($\theta_M(0,0)=0\,\text{rad}$) and the cost of forcing the bond to a substrate is maximum, because the tangential plane of the free helix is perpendicular to the substrate. With the data from MD, this energy is around $5\,k_BT$, not at all negligible. This explains why monomers avoid anchoring values around $\frac{\pi}{2}\,\text{rad}$, as can be seen in section 6.2.

Simulations

In this section we developed a mathematical model to describe how a protein-filament helix behaves when it is forced on a plane by an anchoring potential. Here we will use this model to analyse ideal filaments under different conditions. Filaments are said to be ideal because interactions between different bonds are neglected. Bonds are only required to respect the equilibrium probability distribution for torsion and curvature. This is the procedure that was followed to create the filament in Figure 5.8, where curvature and torsion values follow the distribution given by the MD simulations (see Figure 5.7). For the ideal filaments on a surface, the distribution cannot be taken directly from MD, since we are not dealing with free filaments any longer. Instead, we use the equation 5.62 for the energy of a bond to obtain the relative probability of every set of values $(\varphi, \varphi', \theta)$ (θ_0 and ψ_0 already fixed by the MD data). Monomers were added in this way to both ends of the protein chain. It is important that we add monomers to both ends because the probability distributions are not symmetrical ($P(\varphi, \varphi + \Delta\varphi, \theta) \neq P(\varphi - \Delta\varphi, \varphi, \theta)$).

Since it is not trivial that this should be so, let us imagine a particular situation as an example: consider a monomer with an ideal anchoring value $\varphi_0 < 0$ rad. The neighbour monomer can share this anchoring value, but then the bond will have a twist far from the optimal value ψ_0. Alternatively, the monomer can have the right twist and sacrifice some anchoring interaction. It is this second case that is asymmetrical. Of course, the anchoring interaction for both $\varphi_0 \pm \psi_0$ is identical, as is the energy contribution from twist

$$\kappa_\psi(1 - \cos((\varphi_0 - \psi_0) - \varphi_0 + \psi_0)) = \kappa_\psi(1 - \cos(\varphi_0 - (\varphi_0 + \psi_0) + \psi_0)) = 0$$

But the cost of keeping the bond on-plane will be lower for $(\varphi_0, \varphi_0 + \psi)$ than for $(\varphi_0 - \psi, \varphi_0)$, because the first case is closer to the ideal situation $\varphi + \frac{\psi_0}{2} \approx \varphi' - \frac{\psi_0}{2} \approx 0$ rad, where the tangent plane of the bond is on the surface. So, unless φ_0 equals 0, $\frac{\pi}{2}$, π or $\frac{3\pi}{2}$ rad, $P(\varphi, \varphi + \psi, \theta) \neq P(\varphi - \psi, \varphi, \theta)$ and we need to consider both ends of the filament when building the filaments.

As illustrated in Figure 5.14, we performed simulations for different anchoring conditions (in particular, different values for the anchoring angle φ_0 and the

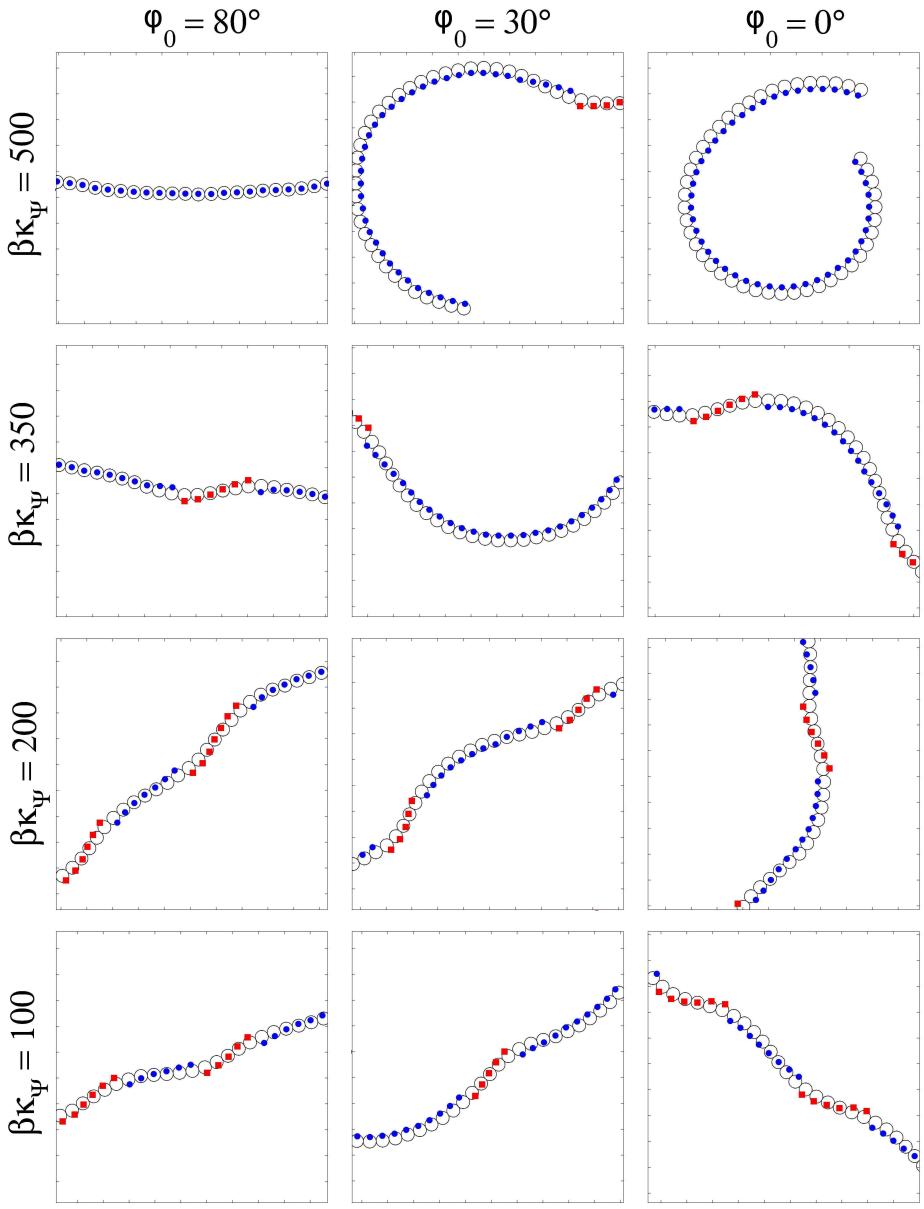

Figure 5.14: Typical shapes of FtsZ filaments on a planar substrate, obtained from the independent bond distribution model, with the helix parameter and elastic constants obtained from the MD fluctuations of the free pentamer, under different parameters for the anchoring of the protein monomers on the substrate [34].

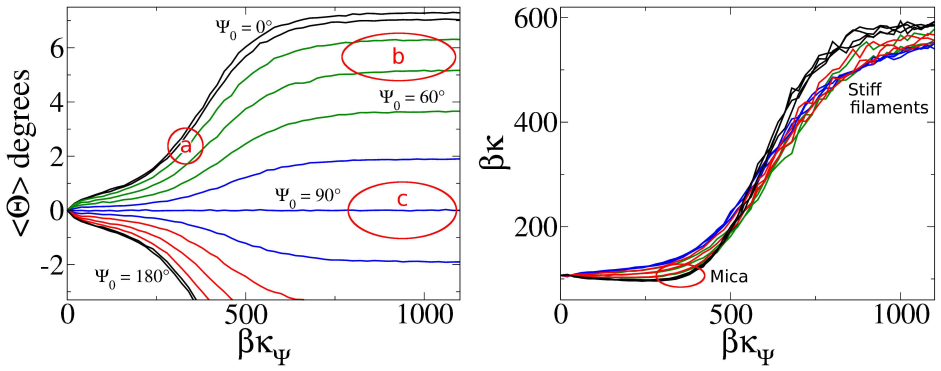

Figure 5.15: The on-plane mean angle (left) and bending rigidity (right) from our MD-based model under different parameters of the anchoring potential. Region (a) corresponds to the curvature observed on mica [27, 31]. Regions (b, c) correspond to well-anchored filaments with low and high curvature, as explained in this and next section in more detail [34].

stiffness of the anchoring, that is, the width of the anchoring potential). The resulting filaments can form rings or filaments without apparent curvature, as was expected. Changing φ_0 affects the mean on-plane curvature (θ_M) for well anchored monomers, while variations in the anchoring stiffness, κ_a, alter the balance between anchoring and twist, from filaments where anchoring seems to play no role, to filaments that show no torsion at all. The combination of these effects results in three main different filament shapes. Fist, there are rings of different radius, mainly filaments where anchoring is predominant (Figure 5.14 up-right). If these well-anchored filaments have a different anchoring angle, they will eventually form open curves and even straight filaments (Figure 5.14 up-left). Lastly, when anchoring is not strong enough to prevent the filament from twisting, wiggly filaments with no net curvature are formed (Figure 5.14 down). It is important to note that these filaments can seem very similar to genuinely straight filaments in experimental conditions, so it may be difficult to distinguish both situations. It is also interesting to see how this balance between anchoring and torsion could interfere with stiffness measurements. If we try to evaluate the stiffness of a filament on a surface by analysing its shape, those with stronger anchoring will show fewer changes in direction, and thus will seem stiffer, despite the fact that the filaments are the same in every case.

In Figure 5.15 we have the graphical description of the previous paragraph. As the width of the anchoring potential is reduced (which pulls the anchoring-torsion balance towards anchoring) curvature increases for every value of the optimal anchoring angle (except for 90°, which has no curvature). At the same

time filaments seem to be stiffer, because torsion (and its changes in curvature direction) is less frequent. The specific zones highlighted in the graph correspond to different experimental situations, as will be explained in next section. In short, they correspond to soft rings on mica (a), and stiff rings and stiff straight filaments on a lipid surface.

The basic model we have introduced here may also be used to get a rough estimate for the forces that can be exerted upon the membrane by the filaments, by means of their natural curvature and an specific anchoring orientation. In a rather simplistic approach intended to find the order of magnitude of these forces, we will consider perfectly untwisted filaments ($\varphi = \varphi'$ for every bond) with different anchoring orientations (from 0° to 180°). We know, from eq. 5.62, the energy required to hold the bond on-plane

$$\kappa_\theta \left[1 + B\left(\varphi, \varphi'\right) - A\left(\varphi, \varphi'\right)\right],$$

where $B\left(\varphi, \varphi'\right) - A\left(\varphi, \varphi'\right) = -\cos\gamma$; γ being the angle deviation from the surface for the free bond ($0 \leq \gamma \leq \theta_0$). It is a very good approximation (deviations under 0,2%) to consider

$$E\left(\gamma\right) = \frac{\kappa_\theta}{2}\left(\gamma\right)^2. \tag{5.64}$$

We also know that force is the gradient of energy

$$F = -\nabla E\left(\gamma\right) = -\frac{1}{d}\frac{\partial E\left(\gamma\right)}{\partial \gamma} = -\frac{\kappa_\theta \gamma}{d}. \tag{5.65}$$

An obvious difficulty we need to consider is the fact that the surface will not always be plain, on the contrary, it shall never be so in living bacteria, presenting a curvature that increases as the division proceeds. We have to correct the angle consequently

$$F = -\frac{\kappa_\theta\left(\gamma - \gamma_{SURF}\right)}{d}. \tag{5.66}$$

No matter how strong our force is during the initial steps of division, if it is only based on curvature (with or without hydrolysis) the mechanism will eventually fail. What is more, it will start working *against* cell division. Clearly a complementary mechanism is needed for the late steps of division, or perhaps an altogether new interpretation of the process is required.

Notwithstanding this caveat, it is interesting to consider the force that might be obtained from the natural curvature of the filaments under the best circum-

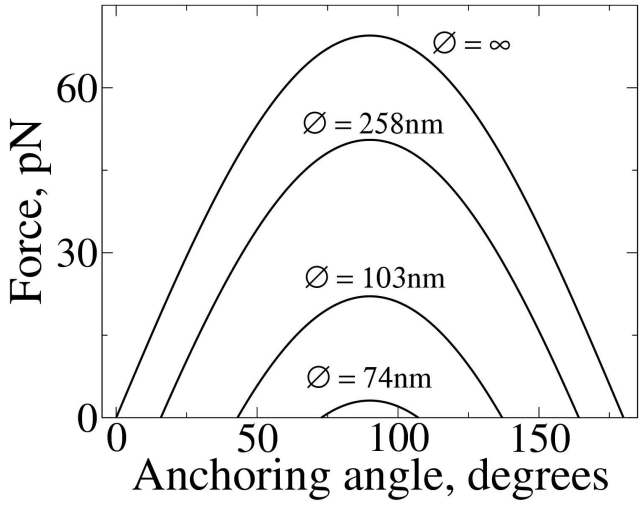

Figure 5.16: The off-plane force as a function of filament orientation on the surface. The force is maximum for preferential anchoring $\varphi_0 = 90°$. Ø indicates the diameter of the curved surface where the filament is attached.

stances. In Figure 5.16 we have the force each monomer will exert as a function of the curvature of the surface and the anchoring orientation of the filaments. These ideal, maximum values, are well above the threshold of 8 pN usually considered to be needed for division [38], even for anchoring orientation far from the optimal perpendicular attachment and even for a well advanced division (the last curve, for Ø=74 nm corresponds to about 1/7 of the diameter of *E. coli*). However, we are still far from understanding bacterial division.

It needs to be emphasized once again that our force calculations assumed perfect anchoring of the monomers to the surface, producing maximum stress. Loose attachment provides a way of releasing the filament bending strain through torsion. The possibility that twist, curvature, orientation and attachment of the filament with respect to the membrane participate in modulating the constriction force offers possible explanations to the role played by different proteins that bundle the filaments and attach them to the surface.

Any model that considers force production induced by filament curvature to be an important ingredient in cellular division needs to explain why the filaments adopt that particular orientation with respect to the surface. This ordering mechanism could be something as simple as the result of inter-filament interactions coupled with the particular geometry of the cell, or perhaps something more involved like a complex of proteins directly affecting the attachment of FtsZ to the surface. (Although special attention is given to FtsZ, we already know many other agents involved in the process, although the role of each of them is not clear

yet [14].) Furthermore, the correction of the on-plane curvature of the filaments also needs to be accounted for, because values of anchoring different from 90° will always have a natural on-plane curvature (θ_M) that will tend to produce mini-rings instead of a bigger constriction ring. Again, this might be explained by something as simple as protein–protein interactions and geometry, or perhaps attachment during division is close to 90° and this problem is of little importance. However it may be, more research needs to be done regarding these issues.

Experimental contrast

The ideal-filaments model derived from the MD data relates curvature and torsional strain, optimal anchoring and monomer orientation with the final conformation and shape fluctuations on a flat surface. Although quite simple, this model can help to understand some puzzling experiments performed with AFM in very different conditions.

When FtsZ filaments are absorbed on a mica surface there is no direct control over the orientation of the monomers on the surface. The measured height of the filaments indicates that they are in close contact with the planar substrate, but there is no information about monomer orientation and anchoring. It was recently shown that a mica surface promotes the assembly of cytoskeletal proteins. In the study which was mentioned at the beginning of this chapter [33], FtsZ was able to polymerize directly on a mica surface when incubated below their critical concentration. Imaging was performed in air after fixing the sample with 0.02 (w/v) uranyl acetate at different incubation times following the polymerization process. Longer incubation times gave long and curved filaments similar to ones previously observed under solution [39, 40]. Shorter incubation times showed coexistence between very straight and curved filaments, and their angle distribution differed from the Gaussian distributions obtained when filaments were imaged under solution [27]. Figure 5.2 presents the histogram of mean curvatures extracted from the digitalized images. As has already been mentioned, this histogram is problematic because it is clearly not a Gaussian distribution, as could be expected. A possible explanation for the dimorphism of the filaments comes from the crossed effects of the internal torsion of the bond between protein monomers and the anchoring of each monomer to the surface. According to the curvature–torsion model, when the monomers of a filament are

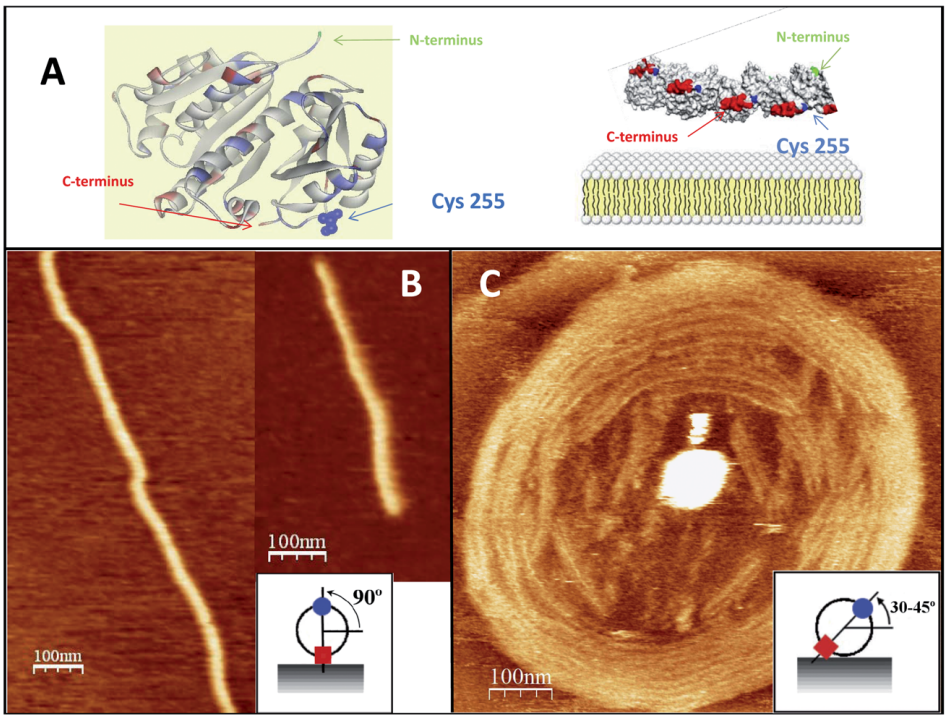

Figure 5.17: FtsZ covalently anchored to lipids. (A) shows the position of the cysteine used to anchor the protein, located near the C-terminus end. The C–N tangent plane of the untwisted filament stands at $\simeq 90°$ with respect to the surface. (B) Straight filaments on a neutrally charged lipid surface. (C) Curved filaments on a negatively charged lipid surface. From reference [34].

well anchored to the surface, they cannot have their natural twist (which would rotate the monomers preventing them from conserving their ideal orientation with respect to the surface), so the bond is weaker than the ideal free bond. In other words, nice anchoring sacrifices good torsion, which implies an energy penalty. Of course the opposite is also true: nice torsion prevents good anchoring, which results in an energy penalty.

This hypothesis leads to structures with a discrete number of torsion turns, as local minima of the torsion plus anchoring energies, so that the filament may be trapped in a sub-optimal structure for a long time before the thermal fluctuations take it over the energy barriers towards the structure of minimum global energy. (Review section 5.1.) The observed polymorphism of the filament shapes in the AFM images could therefore represent the coexistence of filaments in different twist configurations. The spontaneous curvatures observed experimentally are compatible with $30° \lesssim \varphi_0 \lesssim 45°$, indicating that the C-terminal to N-terminal plane is standing at such angles with respect to the mica plane.

In order to further test the hypothesis that the orientation of the tangent plane of the filaments with respect to the surface determines the curvature, we performed experiments anchoring a mutant form of *E. coli* FtsZ, containing a cysteine in position 255, to lipid surfaces. FtsZ monomers covalently attached to a lipid surface through a well defined position can reversibly polymerize on the surface in the presence of GTP [28]. If the cysteine (anchoring point) is located near the C-terminal region of the protein (Fig. 5.17 A), the C-terminal to N-terminal plane will be perpendicular to the surface ($\varphi_0 \simeq 90°$), giving rise to straight filaments. Figure 5.17 B shows straight filaments observed on lipid bilayers containing a zwitterionic[1] lipid head (DOPC). However, when the same proteins are attached to lipids containing a negatively charged head (cardiolipin), filaments are curved (C). Curved filaments are also observed for other negatively-charged membranes (Figure 5.18). The cysteine is located near the carboxy terminal end but surrounded by a patch of negatively charged lipids (Figure 5.19). A possible interpretation of this puzzling result is that the negative charges of the surface reorient the C-ter–N-ter plane with respect to the plane of the membrane, leaving it close to the previously estimated value for the experiments on mica, also negatively charged ($30° \lesssim \varphi_0 \lesssim 45°$). Although the attachment of the protein to the lipid is made through a covalent bond, the S9 loop region where the cysteine is located has been defined as being highly flexible [41, 42] allowing for reorientation of the tangential torsion plane with respect to the surface.

Discussion

The theoretical model we have discussed in this section includes both bend and twist angles between protein monomers as given by the analysis of the FtsZ pentamer in MD simulations. This approach has some advantages over other published models. On the one hand, the quantitative estimate of the bending and twisting rigidities are reliable, as confirmed by their agreement with experimentally estimated values of the persistence length [27, 43]. On the other hand, the angles and their fluctuations are very well defined in space with respect to the protein coordinates. These two elements allow us to obtain additional information: how the orientation of the protein monomers with respect to the

[1] A zwitterion is a neutral molecule with a positive and a negative electrical charge. Aminoacids are a well-known example.

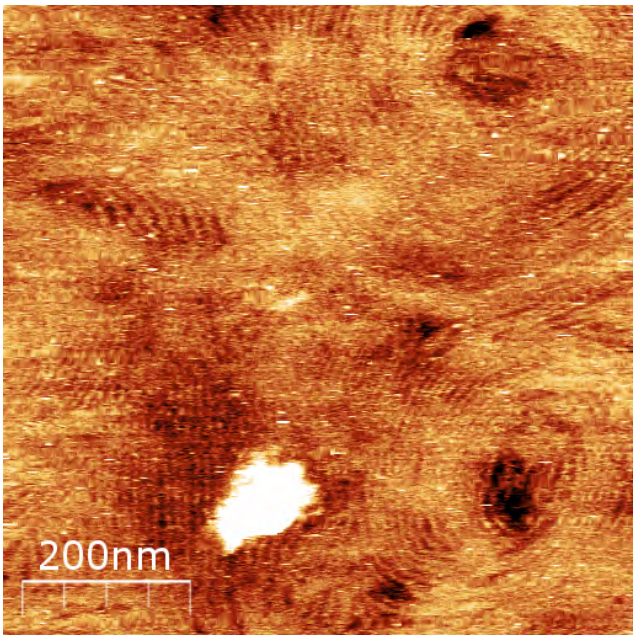

Figure 5.18: FtsZ cysteine mutant S255 anchored to the lipid bilayer through cysteine 255 to maleimide lipids. Curved filaments are formed when a negatively charged lipid is included in the membrane. Lipid membrane composition is DOPC 80%, *E coli* polar lipids 10%, DSPE-Mal 10%. From reference [34].

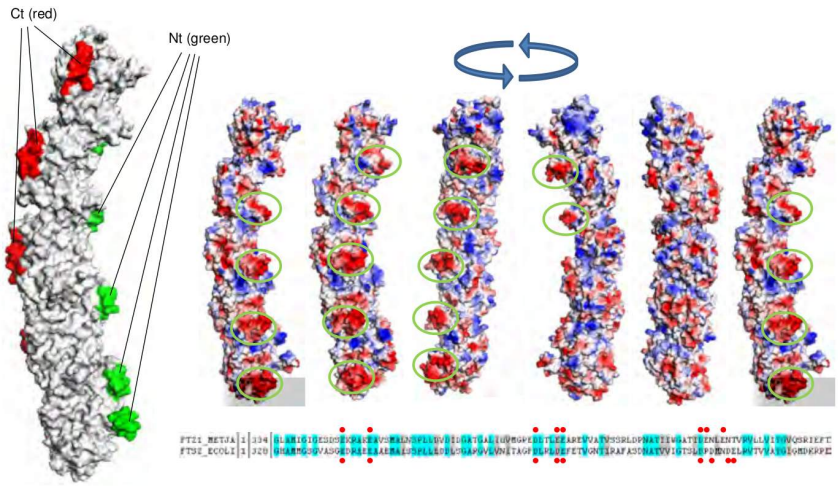

Figure 5.19: The diagram depicts in red the negatively charged aminoacids in FtsZ from *Methanococcus Jannaschii* and indicates that they are also conserved en *E. coli* FtsZ. From reference [34].

surface to which they are attached affects the overall filament shape, and how the anchoring strength can modulate both their shape and properties. The model presented here indicates that the presence of torsion and curvature, combined with the attachment to the membrane surface, provides a strategy to modulate bending rigidity and a mechanism, different from GTP hydrolysis, to produce a switch from straight to curved conformation with respect to the membrane surface.

It is known that both FtsA and ZipA, proteins that link FtsZ to the membrane, bind to the carboxy terminus end of the protein [8]. Our model indicates that this particular orientation has important consequences: it allows for the formation of straight filaments with $\varphi_0 \simeq 90^o$ that, depending on the tightness of the bonding, could transmit the tension to the underlying surface. One of the most important conclusions that can be drawn from this chapter—and perhaps the whole thesis dissertation—is that anchoring details are essential to any model that attempts to explain FtsZ dynamics and bacterial division. We have seen how anchoring can determine the on-plane curvature of the filaments or the force exerted on the surface. This is a problem common to the other models that have been proposed so far. Take, for instance, the hydrolisis-driven hypothesis. This model suggests that hydrolisis increases the natural curvature of the filaments and thus triggers division. But this will be of little help if this curvature is not carefully kept perpendicular to the surface. Otherwise filaments will curve on the membrane and there will be no force.

The information available about the orientation and surface attachment of FtsZ to the membrane are both compatible with the suggestion that these elements could be regulated *in vivo* to trigger and modulate the force generation spatially and temporally within the cell. The role of anchoring as a regulation mechanism is also hinted by the fact that FtsZ binds through its C-terminus end to the membrane through a flexible unstructured region that is well conserved in many organisms [42, 44]. Furthermore, FtsA and ZipA, the proteins that have been associated with FtsZ binding to the membrane, also contain an unstructured region [10, 9, 45]. In reconstituted systems, the distance and probably the stiffness of the membrane attachment of FtsZ through ZipA, modulated by the presence of charged lipids on the membrane, is indeed associated with the degree of curvature [46]. On top of that, other factors and proteins, like those that bundle FtsZ filaments like ZapA, ZapB and ZapC [47, 48], could play a role similar to that of a strong surface attachment: inhibiting filament torsion and fixing the

orientation of the filaments, determining the filament stiffness and the stress transmitted to the membrane. Although the results obtained here refer only the analysis of single filaments, it would be worth exploring the role that bundling plays on the properties of the polymer fibers [49].

Interestingly, very recent experiments using Polarized Fluorescence Microscopy have shown an unexpected disordered organization of the filaments [50]. It could well be that the disorder detected could reflect the different monomer orientations due to torsion. It is likely that lateral interactions and filament curvature both play important roles at different stages of the force generation process: lateral interactions between filaments could participate in condensing the filaments into a ring possibly exerting some force [23, 51], and filament curvature, once the twist is eliminated, either through filament surface attachment or bundling, could produce the final power stroke. The quantitative evaluation provided by this model contributes to refine our picture of how FtsZ structure and surface binding come together to generate force on the underlying membrane.

6

Collective effects of torsion in FtsZ filaments

6.1 Fine-grained model with torsion-I: simulations for open and closed filaments

As a preliminary exploration of the effect of introducing torsion and anchoring in the fine-grained model, the program presented in section 3.1 was upgraded to accept the new dimension, anchoring angle, which was allowed 24 different values (with 15° increments) as was the case for on-plane orientation. This would later prove not to be enough resolution, as explained in section 6.2. Monomers in the model are now defined by their position, orientation angle and anchoring angle.

Of course, the interaction between monomers had to be adapted to this new dimension. In the first place, an anchoring potential was added for each monomer. This interaction took the simple form of a parabola and was not allowed repulsive values—anchoring potential is either negative or zero. This was done to reproduce a situation where anchoring is slightly advantageous near a given value, but neutral far from it.

$$U_{anchoring} = \min\left[-U_a + \kappa_a\left(\varphi_i - \varphi_0\right)^2,\ 0\right] \tag{6.1}$$

The longitudinal interaction was modified to take its maximum value only for a torsion of 15° (one step in anchoring angle) around which the longitudinal bond weakens quadratically down to a saturation value.

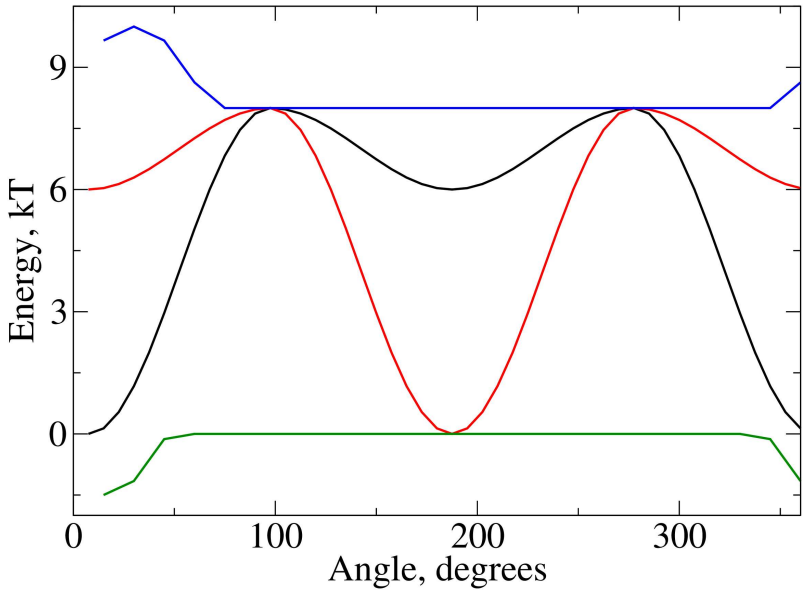

Figure 6.1: Different interactions as a function of the anchoring angle (or torsion for the case of the longitudinal bond). An arbitrary set of interaction values is shown. The blue curve corresponds to the longitudinal bond energy. Red and black are the curvature penalties (which are interchanged after 180°). The green curve is for the anchoring potential.

$$U_b = \min\left[-U_{b0} + \kappa_t \left(\Delta\varphi - \psi_0\right)^2 , -U_{bmin}\right] \tag{6.2}$$

With the new anchoring dimension the curvature energy penalties (U_-, U_+) had to be upgraded as well, which was also done aiming at the simplest solution. Filaments are assumed to be more flexible in a certain direction and much more rigid in its perpendicular one [35]. Here we assigned 0° anchoring to the flexible case (no change in U_-, U_+) and 90° anchoring for the rigid one ($U_- = U_+ = U_{stiff}$). The transition adopts a sinusoidal curve (see Figure (6.1)). Of course, in a given bond there will be two anchoring angle values (one for each monomer) so the average was considered in order to assign the curvature penalties. Note that the specific value of U_+ and U_{stiff} is of little importance as long as they are a few κ_BT greater than U_-.

Single filament simulations

The fine-grained model with torsion was used to observe single filaments. Rupture of the filaments (induced by the low density in a single-filament simulation)

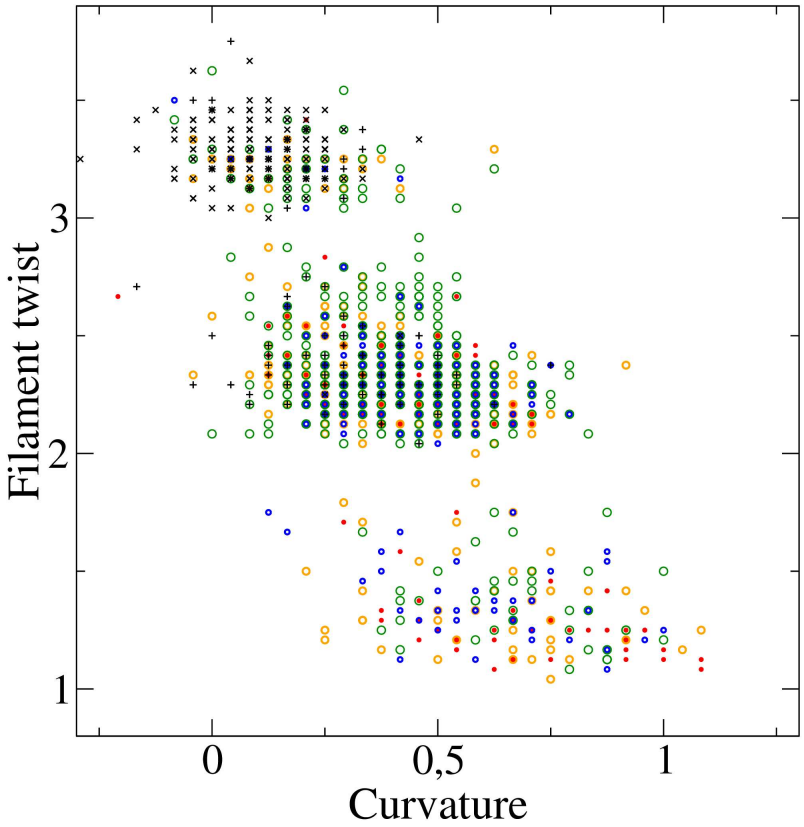

Figure 6.2: Twist *versus* curvature for filaments of 80 monomers. Different symbols correspond to different choices for the with of the parabola in the longitudinal bond interaction, κ_t (from $\kappa_t = 10$ to $\kappa_t = 30\,\mathrm{k_B T/rad^2}$). The rest of the parameters are: $\beta U_a = 1$, $\kappa_a = 0.5\,\mathrm{k_B T/rad^2}$, $\varphi_0 = 0°$, $\beta U_{b0} = 25$, $\psi_0 = 15°$, $\beta U_{bmin} = 4.2$, $\beta U_- = 0$, $\beta U_+ = 5$, $\beta U_{stiff} = 7$.

can be avoided by an increase in the longitudinal bond energy, which will only affect the filament's life expectancy, but not its dynamics. Given that the filament is already formed from the start of the simulation and that it will not be allowed to break or interact with other filaments (not even with itself forming coiled structures, because U_{lat} is set to zero) the choice of parameters will essentially shift the balance between anchoring and torsion. In this rather naive exploration of the model we play with the width of the parabola (κ_t) in the longitudinal bond energy (see Figure 6.1) to achieve the shifting effect. Filaments of 80 and 160 monomers were used.

As could be expected from the analytical study in section 5.1, filaments are distributed in different "clouds" of curvature–torsion, which would correspond to different curves in a graph like Figure 5.4. Supposing a filament had a suboptimal number of torsion turns, winding or unwinding the whole filament to add or

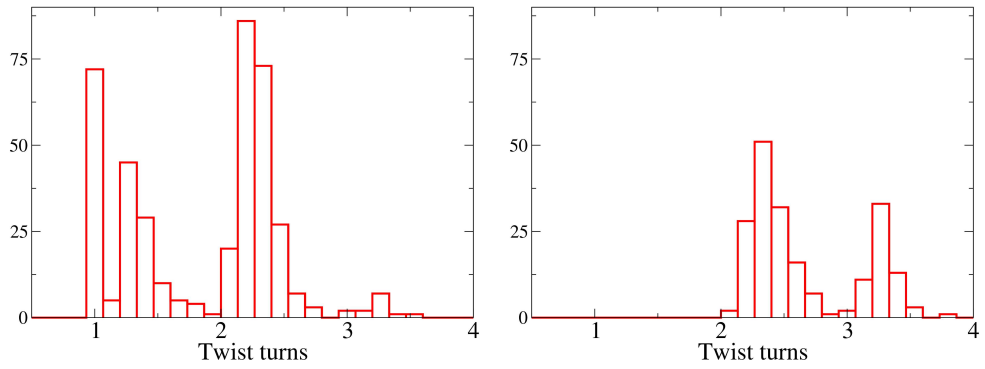

Figure 6.3: Histogram for the torsion of filaments of 80 monomers showing how changes in the interaction parameters (in this case,κ_t = 11.5 and κ_t = 14 k_BT/rad^2 respectively) can change the balance from anchoring to torsion. The peak in one turn for the first graph corresponds to filaments that closed in a ring. The rest of the parameters are the same as in Figure 6.2; $\beta U_a = 1$, $\kappa_a = 0.5\, k_BT/rad^2$, $\varphi_0 = 0°$, $\beta U_{b0} = 25$, $\psi_0 = 15°$, $\beta U_{bmin} = 4.2$, $\beta U_- = 0$, $\beta U_+ = 5$, $\beta U_{stiff} = 7$.

eliminate one complete turn would involve all or most of the monomers in the filament, so the energy barrier is important. This explains why we do not see a unique cloud for each value of the parameter κ_t in Figure 6.2. Although for each cloud the curvature distribution does not seem far from Gaussian, taking all of them together will clearly not be Gaussian, supporting the idea that torsion may be indeed present in experiments like those in Figure 5.1.

If we plot the histogram for torsion alone (figures6.3 and 6.4) for two different values of the parameter κ_t, we can clearly see how increasing κ_t changes the balance towards more torsion (in detriment of anchoring). In Figure 6.2 all filaments distribute around the same clouds regardless of κ_t, which only affects the number of filaments in each cloud.

In previous work with single FtsZ filaments, it was observed that isolated rings tended to have a greater ellipticity than should be expected for a free filament ring with a given elasticity [35]. For this reason we decided to explore whether torsion could be involved in the problem. The basic idea is that where there is a twist turn in a filament, bonds are stiffer, as seen in Figure 6.5. This is because the plane where filaments are more flexible will not match the anchoring surface along a turn. Midway through the turn the plane will again coincide with the anchoring plane but with reversed natural curvature. Therefore, twisting regions should behave in a stiffer way and may even show reversed curvature, and thus they could promote ellipticity in a FtsZ ring with twist turns (which, as we saw before, could arise in the anchoring–torsion balance).

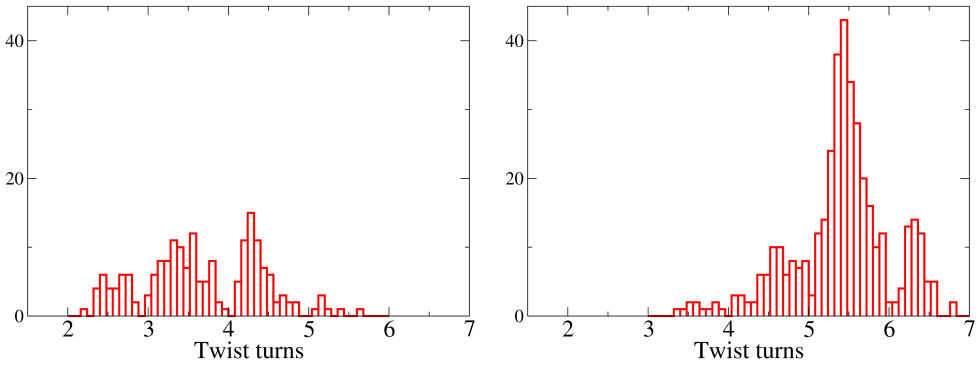

Figure 6.4: Histogram for the torsion of filaments of 160 monomers showing how changes in the interaction parameters (in this case,$\kappa_t = 11$ and $\kappa_t = 14\,k_BT/rad^2$ respectively) can change the balance from anchoring to torsion. The peak in one turn for the first graph corresponds to filaments that closed in a ring. The rest of the parameters are the same as in Figure 6.2; $\beta U_a = 1$, $\kappa_a = 0.5\,k_BT/rad^2$, $\varphi_0 = 0°$, $\beta U_{b0} = 25$, $\psi_0 = 15°$, $\beta U_{bmin} = 4.2$, $\beta U_- = 0$, $\beta U_+ = 5$, $\beta U_{stiff} = 7$.

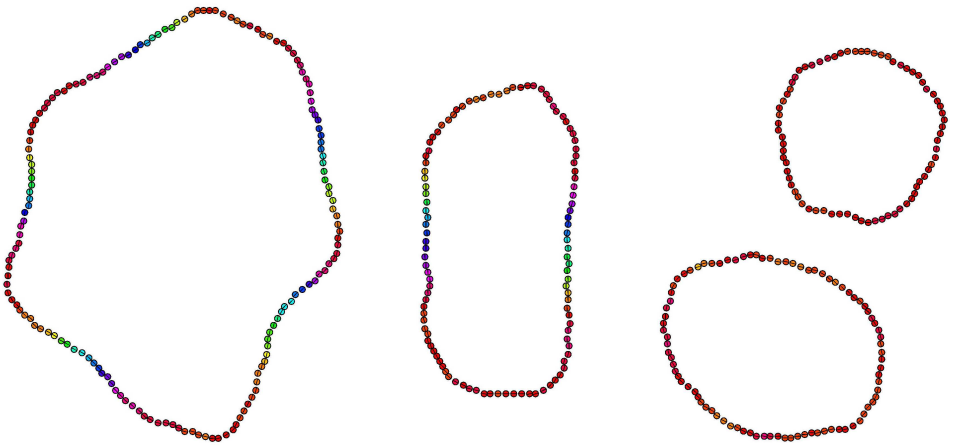

Figure 6.5: Set of rings of different length. Colour indicates anchoring angle, which is optimal in the red region in this case. Blue–green regions indicate twist turns.

Filament rings were simulated with a different number of turns (the torsion along a closed filament will always be a natural number of complete turns) and their ellipticity was measured to see if there is a relationship between both parameters. In order to measure the ellipticity of the ring we take the Fourier series for the radius of the ring. If we express this as a function of the angle, we have

$$r(\gamma) = \frac{a_0}{2} + \sum_{1}^{\infty} \left[a_n cos(n\gamma) + b_n sin(n\gamma) \right] \tag{6.3}$$

where

$$a_n = \frac{1}{\pi} \int_{-\pi}^{\pi} r(\gamma) cos(n\gamma) d\gamma. \tag{6.4}$$

Provided there are enough points (monomers) for the ring, this can be approximated by

$$a_n \approx \frac{1}{\pi} \sum r(\gamma_i) cos(n\gamma)(\gamma_i - \gamma_j) \tag{6.5}$$

$$b_n \approx \frac{1}{\pi} \sum r(\gamma_i) sin(n\gamma)(\gamma_i - \gamma_j).$$

An alternative representation is given by

$$a_n cos(n\gamma) + b_n sin(n\gamma) = A_n cos(n\gamma + \beta_n) \tag{6.6}$$

The ellipticity of the ring will be given by A_2. Analysing the ellipticity of all the rings does not help much, but if we look at the histograms for filaments with the same number of turns, we can clearly see how, as the number of turns increases from 0 to 1 and then 2, the mean ellipticity also increases (Figure 6.6). For filaments of this length (around 100 monomers) it was not easy to obtain stable filaments with many more turns, however, the few simulations that could be performed hint that ellipticity either stabilizes or even decreases as the number of turns increases further. This may be explained by the same hypothesis: when a ring has no turns (remember we are assuming turns to be less flexible) it will naturally be round on average. If we introduce one turn, that is, a rigid segment, the symmetry is broken and ellipticity will increase. Introducing yet another turn recovers some symmetry, but as we will see in a moment, different twist segments repel, so they tend to migrate to opposed regions of the ring, which

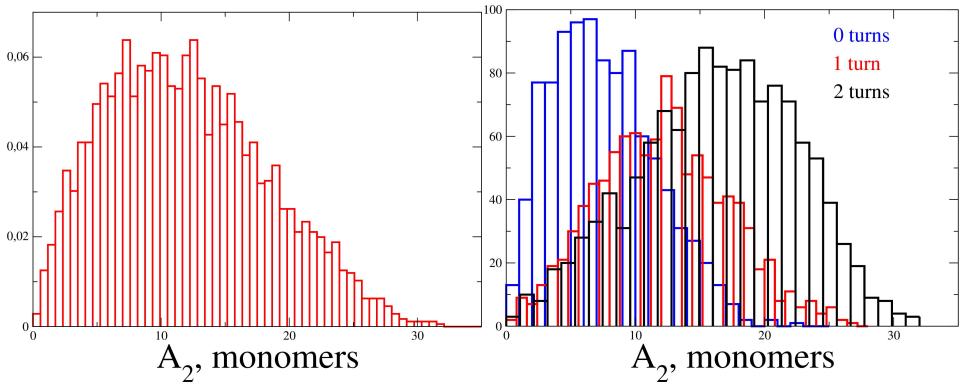

Figure 6.6: Histogram for the number of rings with a given ellipticity value A_2. In the second image there is a separate histogram for rings with a different number of twist turns, showing a correlation between torsion and ellipticity.

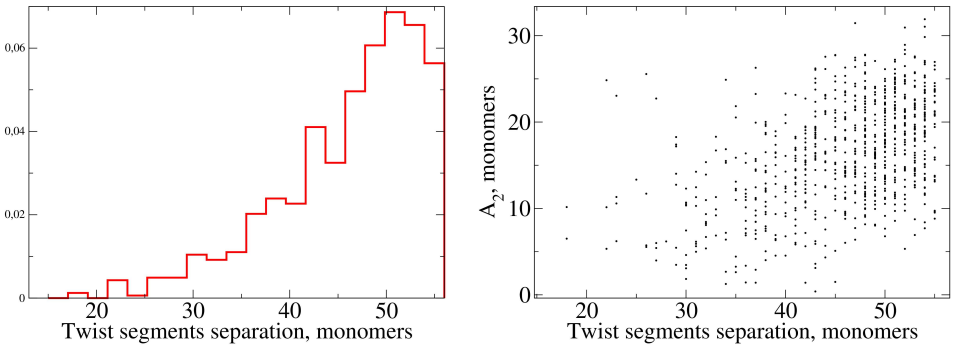

Figure 6.7: On the left side, histogram for the separation of the torsion regions in rings of 110 monomers and two twist turns. The graph on the right shows this separation *versus* the ellipticity of each ring.

is thus elongated (with an increase in ellipticity). Taking these ingredients into account, there is no good reason why ellipticity should increase further as we add more turns, on the contrary, it could be argued that uniformly distributed straight segments will converge towards a figure with circular symmetry—and so low ellipticity.

To see if the "stiff-turns and ellipticity" hypothesis has any basis, we studied with a little more detail rings with two turns, and compared some results with a very basic mathematical model for such rings. For this set of filament rings we identified the two different regions of torsion and measured the shortest distance between them (the shortest distance between the ends of the turn). The histogram in Figure 6.7 clearly shows that this distance is not random. On top of that, we see a correlation between the separation of the twist segments and ellipticity.

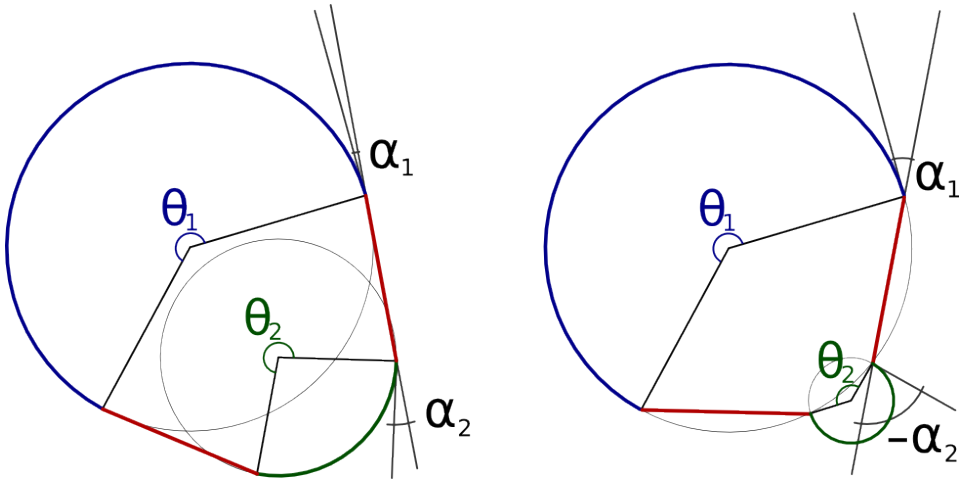

Figure 6.8: Scheme for the mathematical model representing rings with two twist segments (red).

We consider now a very simple mathematical model for the rings. We will assume the torsion regions to be perfectly straight and 12 monomers long each. The two remaining segments of the ring are considered circular arcs. In many cases the result is rather realistic, as the first example in Figure 6.8, however, extreme situations like the second ring of the figure should clearly allow for different kinds of curves.

We are interested in developing an expression for the energy of the ring, which will be related to the curvature of the different segments. Knowing the values for U_- and U_+ (0 and 5kT in this case) we can first find the ideal average curvature. We consider U_b as the reference, so the energy for a straight bond is 0kT. In order to find the average curvature we first write the partition function for curvatures, bearing in mind that there are four different positions for a straight bond but only three for bonds with curvature. Then

$$Z = 4e^{-\beta 0kT} + 3e^{-\beta U_-} + 3e^{-\beta U_+}. \tag{6.7}$$

If we remember, curved bonds form a $\pm 15^o$ ($\sim 0,262 rad$) angle. We can now evaluate $\langle\theta\rangle$:

$$\langle\theta\rangle = \frac{0\,\text{rad}\cdot 4\cdot e^{-\beta 0kT} - 0,262\,\text{rad}\cdot 3\cdot e^{-\beta U_-} + 0,262\,\text{rad}\cdot 3\cdot e^{-\beta U_+}}{Z}. \tag{6.8}$$

The value for $\langle\theta^2\rangle$ can be obtained in a similar way:

$$\langle\theta\rangle = \frac{0\,\mathrm{rad}^2\cdot 4\cdot e^{-\beta 0kT} - 0,262^2\,\mathrm{rad}^2\cdot 3\cdot e^{-\beta U_-} + 0,262^2\,\mathrm{rad}^2\cdot 3\cdot e^{-\beta U_+}}{Z}. \tag{6.9}$$

Now it is possible to find $\langle\theta^2\rangle - \langle\theta\rangle^2 = \frac{1}{\kappa}$. In our case, $\kappa \simeq 58,286\,\mathrm{J/rad}^2$. A simplified expression for the energy is thus:

$$\begin{aligned} E_l(\theta_1,\theta_2,\alpha_1,\alpha_2) &= \tfrac{\kappa}{2}\left(l_1\left(\tfrac{\theta_1}{l_1-1}-\theta_0\right)^2 + l_2\left(\tfrac{\theta_2}{l_2-1}-\theta_0\right)^2\right) \\ &\quad + \tfrac{\kappa}{2}\left(2(\alpha_1-\theta_0)^2 + 2(\alpha_2-\theta_0)^2\right) \end{aligned} \tag{6.10}$$

Remember $l_1 + l_2 + 2\cdot 12 = l_{Tot}$ and that $l = \min(l_1, l_2)$. Straight segments are 12 monomers long, and we do not consider their curvature energy because it will be the same for any ring. Note also that $\frac{\theta_1}{l_1-1}$ is the angle for the bonds in the arch l_1 (which covers θ_1 in $l_1 - 1$ bonds). Because for a fixed value of l (that is, l_1 and l_2) there are only two free parameters (θ_1 and θ_2 are enough to define the ring shape and both $\alpha_i(\theta_1,\theta_2)$ can be obtained), we can find the expression for $E_l(\theta_1,\theta_2)$, with a little geometry and patience:

$$\begin{aligned} E_l(\theta_1,\theta_2) &= \frac{\kappa}{2}\left(l_1(\theta_1-\theta_0)^2 + l_2(\theta_2-\theta_0)^2\right) \\ &\quad + \kappa\left(\left\{\arccos\left[\frac{\frac{l_2}{\theta_2}\sin\left(\frac{\theta_2}{2}\right) - \frac{l_1}{\theta_1}\sin\left(\frac{\theta_1}{2}\right)}{r}\right] - \frac{\theta_1}{2}\right\} - \theta_0\right)^2 \\ &\quad + \kappa\left(\left\{\pi - \frac{\theta_2}{2} - \arccos\left[\frac{\frac{l_2}{\theta_2}\sin\left(\frac{\theta_2}{2}\right) - \frac{l_1}{\theta_1}\sin\left(\frac{\theta_1}{2}\right)}{r}\right]\right\} - \theta_0\right)^2 \end{aligned} \tag{6.11}$$

We are interested in the relative probability of having a certain separation l. Supposing for a moment that the energy depended only on one angle θ , we could find θ_0 such that it minimizes E_l and then we can approximate the energy around this value

$$E_l(\theta) \simeq E_l(\theta_0) + \frac{1}{2}\left.\frac{d^2E_l}{d\theta^2}\right|_{\theta_0}(\theta-\theta_0)^2, \tag{6.12}$$

where $\left.\frac{dE_l}{d\theta}\right|_{\theta_0}$ vanishes because it is a minimum of the energy. The probability for the state $E_l(\theta_0)$ will be

$$P(l,\theta_0) = \frac{e^{-\beta E_l(\theta_0)}}{Z}, \tag{6.13}$$

but it is important to note that we are interested in $P(l)$, not $P(l,\theta_0)$, so we have to include the contribution of the other states with $\theta \neq \theta_0$, weighted by their Boltzmann factor. The approximation in eq. 6.12 will only be good near the value θ_0, but having a lower energy close to the minimum, these states should provide the most important contribution. Finally, if we call $\lambda = \frac{1}{2}\frac{d^2E_l}{d\theta^2}\Big|_{\theta_0}$, we get

$$P(l) \sim \frac{e^{-\beta E_l(\theta_0)}}{\sqrt{\lambda}}, \tag{6.14}$$

where we have used $\int_{-\infty}^{\infty} e^{-\beta\lambda x^2} dx = \sqrt{\frac{\pi}{\beta\lambda}}$.

We can now generalize this to two variables. First, we have the approximation for the energy (for convenience we will write $\frac{dE_l}{d\theta_i} \equiv E_i$):

$$\begin{aligned} E_l(\theta_1,\theta_2) \simeq\ & E_l(\theta_{10},\theta_{20}) + \frac{1}{2}\left[E_{\theta_1\theta_1}(\theta_1-\theta_{10})^2 + E_{\theta_2\theta_2}(\theta_2-\theta_{20})^2\right. \\ & \left. +2E_{\theta_1\theta_2}(\theta_1-\theta_{10})(\theta_2-\theta_{20})\right] \end{aligned} \tag{6.15}$$

Using the notation $\overline{\theta} = \begin{pmatrix}\theta_1\\ \theta_2\end{pmatrix}$, the previous equation can be written in a more compact form:

$$E_l(\theta_1,\theta_2) \simeq E_l(\theta_{10},\theta_{20}) + \frac{1}{2}\left(\overline{\theta}-\overline{\theta}_0\right)^T \mathscr{H}^0 \left(\overline{\theta}-\overline{\theta}_0\right) \tag{6.16}$$

where

$$\mathscr{H}^0 = \begin{pmatrix} E_{\theta_1\theta_1} & E_{\theta_1\theta_2} \\ E_{\theta_2\theta_1} & E_{\theta_2\theta_2}\end{pmatrix}. \tag{6.17}$$

If we are lucky enough that $E_{\theta_1\theta_2} = 0$, then we have a situation very similar to the one variable case, and we only need to solve the integral

$$\iint_{-\infty}^{\infty} e^{-\beta\lambda_x x^2} e^{-\beta\lambda_y y^2} dxdy = \frac{\pi}{\beta}\sqrt{\frac{1}{\lambda_x\lambda_y}}. \tag{6.18}$$

Since $\lambda_x\lambda_y = \frac{1}{2}E_{\theta_1\theta_1}\cdot\frac{1}{2}E_{\theta_2\theta_2} = \frac{1}{4}\mathrm{Det}\mathscr{H}^0$, we have found for this easier case that

$$P(l) \sim \frac{e^{-\beta E_l(\theta_{10},\theta_{20})}}{\sqrt{\mathrm{Det}\mathscr{H}^0}}. \tag{6.19}$$

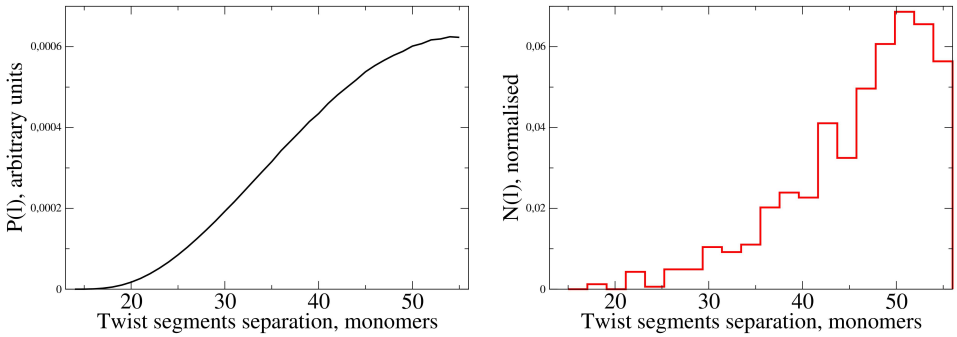

Figure 6.9: Relative probability of having the torsion segments of the ring separated a given length *versus* the histogram for the separation of the segments in computer simulations.

In general $E_{\theta_1\theta_2} \neq 0$, but because $E_{\theta_1\theta_2} = E_{\theta_2\theta_1}$, $\mathscr{H}^0$ is symmetric and a new basis $\begin{pmatrix} \tilde{\theta}_1 \\ \tilde{\theta}_2 \end{pmatrix}$ can be found where $\widetilde{\mathscr{H}^0}$ is diagonal ($E_{\tilde{\theta}_1\tilde{\theta}_2} = 0$). Since the determinant of a matrix is invariant with respect to a change of basis, eq. 6.19 will always hold. We can use this result to plot the probability of having different separations of the torsion segments according to the model and compare it with the results from the simulations, as seen in Figure 6.9.

There is a nice agreement at a qualitative level. We have seen how the torsion segments separation distribution in the simulations is quite similar to the one predicted by a model which considers these segments to be stiff and therefore tend to repel in order to minimize the curvature energy of the ring. Because there is a correlation between this separation of the torsion segments and the ellipticity of the filament ring (Figure 6.7), we can conclude that torsion may indeed explain why some rings have a greater ellipticity than expected.

6.2 Fine-grained model with torsion-II

In chapter 5 we introduced a model that describes FtsZ bonds on a surface using MD data. Although we were able to obtain some interesting results, the basic approach of studying ideal filaments misses many important features of the system. For example, we are interested in exploring the effect of the collective interactions amongst filaments—lateral attractions and excluded volume. Another important limitation of the ideal-filament approach is that it does not account

for the breaking and fusion of filaments, an essential characteristic of a dynamic system such as that of FtsZ's filaments.

We can solve these problems by using a fine-grained model like that of chapter 3, which was already tentatively explored in the previous section. Here we propose to modify the model by including the analysis from MD simulations. By doing this the longitudinal interaction and curvature properties of the bond will have a solid base related to reliable scientific evidence. The mathematical description for monomers on a surface lead to an expression for the energy of a bond in terms of the angles $U\left(\varphi,\varphi',\theta\right)$. Since θ is the on-plane angle between the monomers forming the bond, we have $U\left(\varphi_1,\varphi_2,\theta_1,\theta_2\right)$, and so we can substitute the old interaction algorithm in the fine-grained model by this new one. This substitution is rather straight-forward from the coding point of view, however, it required further modifications of the program.

In the first place, MD data is giving us information about the changes in the longitudinal bond as a function of bending and twist, but it does not provide any clues about the strength of the ideal bond, so we have to include a constant factor U_b in the longitudinal bond of the model.

The older version of the program in chapter 3 used 15° intervals for the orientation of the monomers, quite coarse but enough for the needs of the time. However, just by reviewing the mean value and fluctuations of torsion and curvature ($\langle\theta\rangle \simeq 7,6°$, $\Delta\theta \simeq 2,4°$, $\left\langle\psi\right\rangle \simeq 29°$, and $\Delta\psi \simeq 4°$), we realize we are going to need a more subtle description of the angles. In this case we set both curvature and torsion intervals to 1°. Another important difference is that, before, we only allowed longitudinal bonds for monomers with the same orientation ±15° (that is, ± one orientation step). In the new version we will allow for any orientation of the neighbour monomer provided it is located on the bonding area of the first monomer (see Figure 3.1). Curvature penalties are now part of the interaction relation $U\left(\varphi_1,\varphi_2,\theta_1,\theta_2\right)$. Yet another problem can be guessed from Figure 3.1. In the previous version every orientation had a different bonding area (in fact, the 15° intervals or 24 steps were a consequence of the hexagonal lattice being used). However, if we use 1° intervals this will not be possible. In the new program many different orientations will share bonding area, which is not really a problem, since the bonding interaction $U\left(\varphi_1,\varphi_2,\theta_1,\theta_2\right)$ will differentiate between these orientations, so the lattice does not need to be finner. What we do need to care for is the fact that some bonding areas are made up of 4 lattice points and others by 5. No matter what we do, this will always be the case.

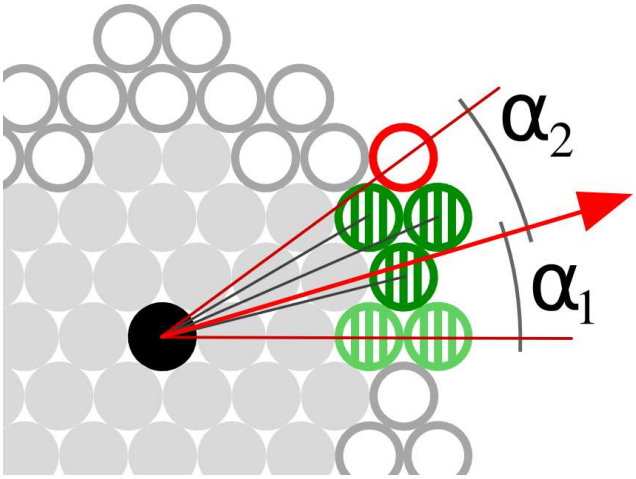

Figure 6.10: Construction of the bonding area. The red arrow shows the orientation of the monomer. Vectors from the origin to the three dark-green striped-circles are the closest to the monomer direction, followed by the vectors to the two light-green striped-circles, which have the exact same direction. There is no other site in the interaction crown with a closer match—the closest alternative is shown in red.

The bonding area is defined examining the angles the points in the interaction crown form with the centre of the monomer. If this angle is close enough to the orientation of the monomer, the site will belong to the bonding area. The problem, illustrated in Figure 6.10, is that for certain orientation angles we will have three sites closer to the orientation value and then two sites at an identical angular distance. So we can only reject both (in which case we will have orientation values with 3 or 4 sites in their bonding area) or accept both (so we have 4 or 5 sites depending on the orientation). A possible alternative is to arbitrarily choose one of the two new sites. In this way we can have equivalent bonding areas for every orientation, at the cost of having a more complex and subjective definition of the bonding area.

In order to be fully understand the consequences of the different definitions for the bonding area we performed a series of control simulations. The effect of having orientations with 4 or 5 sites in the bonding area is that orientations with larger bonding areas will be slightly privileged, since it will be easier to form bonds with them. Of course this effect is very small and can only be noticed when it is amplified in bigger aggregates. If we go back to Figure 3.6, we can see how the orientation of the aggregate in (d) and (e) and the orientation of the main component in the cluster in (g) are all exactly the same. Of course this is no accident; this is one of the privileged orientations. In that simpler case the

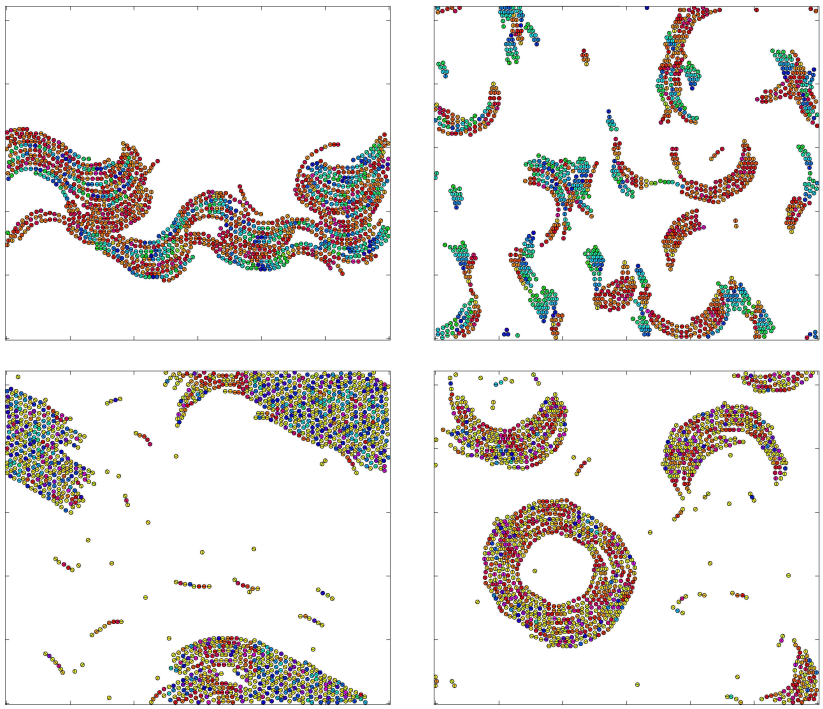

Figure 6.11: Control simulations for different bonding areas. The images in the first column correspond to monomers with four or five sites in their bonding area (depending on the orientation), whereas in the second column all of them have exactly four sites.

consequences are not really more important than that, however, the model is now more complex and will allow for more diverse aggregates where this subtle effect can have more evident consequences. In general the effect is too weak to be relevant, however, in some cases it can affect the balance between different aggregates or it can trigger clusterization at a higher level. Figure 6.11 is a good example of both effects. In conclusion, although the difference is usually small, it is better to have bonding areas of the same size so there are no privileged orientations in the system. The question still remains whether there will be any difference between having four or five sites in each bonding area—all of them being equal now. A series of comparative simulations showed no difference at all between the two alternatives. It was finally decided to have uniform bonding areas of four sites.

First results—the question of the torsion potential

Now that we have a working model for fine-grained simulations with the interaction model from MD data, we want to know what kind of aggregates we are going to find as a function of the system parameters—a phase diagram. But before we proceed we need to explain the weak spot of this model. Remember how the basic ingredient for this model was the MD data, with particular emphasis on the angular fluctuations, which we relate to the width of a quadratic potential. This approximation will be good as long as the twist of the bond is close to the ideal value of torsion, ψ_0 , as was the case for the free-filament MD simulations. However, as the twist gets farther from this ideal value, the energy of the bond rapidly decreases—we say that the energy penalty from torsion is increasing. Following the quadratic potential we soon find that the bond is, not only weak, but strongly repulsive, which is a very unrealistic situation. In short, if bonds are expected to go far from ψ_0, then the interaction model will fail.

The only good solution for this problem is to have new insight into the properties of the bond when it is under important torsion-stress. But we do not have that insight, so, instead, we will explore different refined torsion potentials so as to evaluate the importance of this problem—it could be the case that most bonds are reasonably close to ψ_0 and the model works fine after all. We will consider the simplest modification of the quadratic potential, that is, a truncated quadratic potential. This represents the case where a certain interaction saturates at a point beyond which further change in the parameters has no effect, in our case, where increasing the twist no longer weakens the bond. The specific saturation value for the torsion contribution to the bond energy will be a new variable called U_{MT} (for maximum torsion).

Although the model we have described seems very complex and with a lot of parameters, actually most of them are bound or do not have a very important impact on the structures that are found. The characteristics of the free-bond (except for its total energy) are described in the MD experiments, so their value is fixed. The total energy of the bond, U_b, will be one of the mos relevant free parameters. As has been mentioned at the beginning of this section, the anchored-bond is not guaranteed to remain close to its natural twist ψ_0, so we had to introduce the new

parameter U_{MT}, which will also have an important role. Regarding the anchoring of the filaments, the preferred anchoring angle will be the most important of the parameters. The details of the potential well are not so important for a wide range of the parameters, and its effects can be partially off-set adjusting U_{MT}. For all the simulations that follow, unless it is said otherwise, U_a and κ_a will have fixed values: $U_a = 10\,\mathrm{k_B T}$ and $\kappa_a = 150\,\mathrm{k_B T/rad^2}$.

After a few preliminary tests, the parameters U_b and U_{MT}, as well as the anchoring angle, where found to have the deepest impact in the resulting structures. In figures 6.13 through 6.17 we have a summary of the main structures produced by this model. For each anchoring value that is shown (0°, 30°, 60°, 75° and 90°) there are three columns, each with a different U_{MT} value. Remember that U_{MT} is the saturation value for the torsion contribution to the bond energy. This means that in eq. 6.20 (with the constant U_b now included), the first factor corresponding to twist will be equal to U_{MT} whenever $\kappa_\delta(1-\cos(\varphi-\varphi'+\psi_0)) \geq U_{MT}$.

$$\begin{aligned} U(\varphi,\varphi',\theta) &= U_b + \kappa_\psi(1-\cos(\varphi-\varphi'+\psi_0)) \\ &\quad +\kappa_\theta\left[1+B(\varphi,\varphi')-A(\varphi,\varphi')\right] \\ &\quad +\tfrac{\kappa_\theta A(\varphi,\varphi')}{2}\left(\theta-\theta_M(\varphi,\varphi')\right)^2 \\ &\quad +U_{anc}(\varphi)+U_{anc}(\varphi') \end{aligned} \tag{6.20}$$

It turns out this is a very relevant parameter, since well-anchored filaments will be quite far from their ideal twist (0° *versus* ~29°), so a very low value for U_{MT} ($\lesssim 5\,\mathrm{k_B T}$) will yield results close to the old model without torsion—the main differences being due to the increase in angular resolution, from 15° to 1°—because it will not be very demanding to sacrifice torsion for a better anchoring. As the value of U_{MT} increases, a compromise between anchoring and torsion is established where the anchoring angle along the filament takes a sawtooth shape. In this way one in every two bonds will have a twist closer to the ideal value ψ_0, whereas the rest will be even further from ψ_0 than 0°. This comes at low cost, since the penalty from having a twist different from ψ_0 saturates as soon as it reaches U_{MT}, which happens for $(\varphi'-\varphi)-\psi_0 \gtrsim 18°$ if $U_{MT} = 10\,\mathrm{k_B T}$—and, since $\psi_0 \simeq 29°$, saturation will necessarily occur if we are to find well-anchored filaments, so it is profitable to improve half of the bonds *via* the sawtooth angle profile. This can be better understood with the help of Figure 6.12, and can be best seen in the rings in the second column of Figure 6.14 or 6.15. Remember colour represents

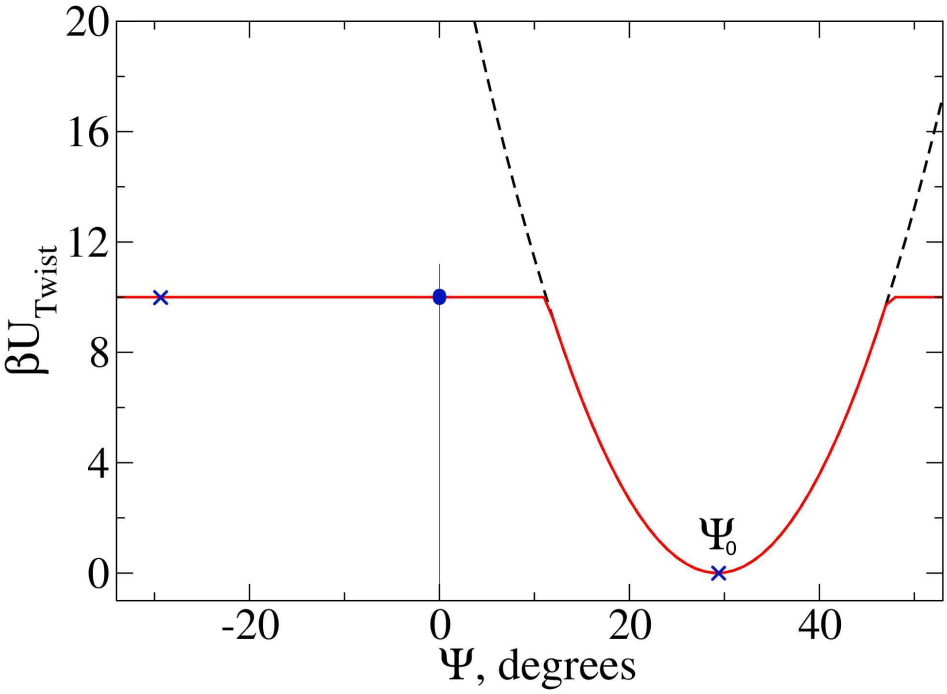

Figure 6.12: Energy contribution from the torsion of the bond ($\beta U_{MT} = 10$). Positive values weaken the bond. In a sawtooth profile for the anchoring angles one bond will have torsion $\psi = 0 + \psi_0$ rad—very low energy—and the other will have $\psi = 0 - \psi_0$ rad (so the average is zero). Because the energy contribution saturates at $10\,\kappa_B T$ for $\psi \lesssim 11°$ this has no extra cost with respect to the case with no torsion ($\psi = 0$).

anchoring angle, and these rings clearly show alternating colour, unlike those where $U_{MT} = 5\,k_B T$, low enough for the effect to be evident—although close examination will reveal it to a lesser degree. Finally, for larger values of U_{MT} ($\gtrsim 15\,k_B T$) filaments can no longer sacrifice twist without breaking and either anchoring takes a secondary role or filaments do break and are noticeably shorter than in the previous situations.

These figures also have two lines for two different values of the longitudinal bond constant ($U_b = 20\,k_B T$, $U_b = 25\,k_B T$). In this case the results are rather similar, the main difference being that for $U_b = 20\,k_B T$ aggregates do not form for $\beta U_{MT} = 15$ and that for lower U_{MT} values shorter filaments with little aggregation are found.

If we compare the figures for different anchoring value we see how the diameter of the rings that are formed for $U_{MT} = 5\,k_B T$ steadily increases as the anchoring angle is also increased. At an anchoring of around 75°the rings finally open and branching filaments take over. There is another interesting effect associated to

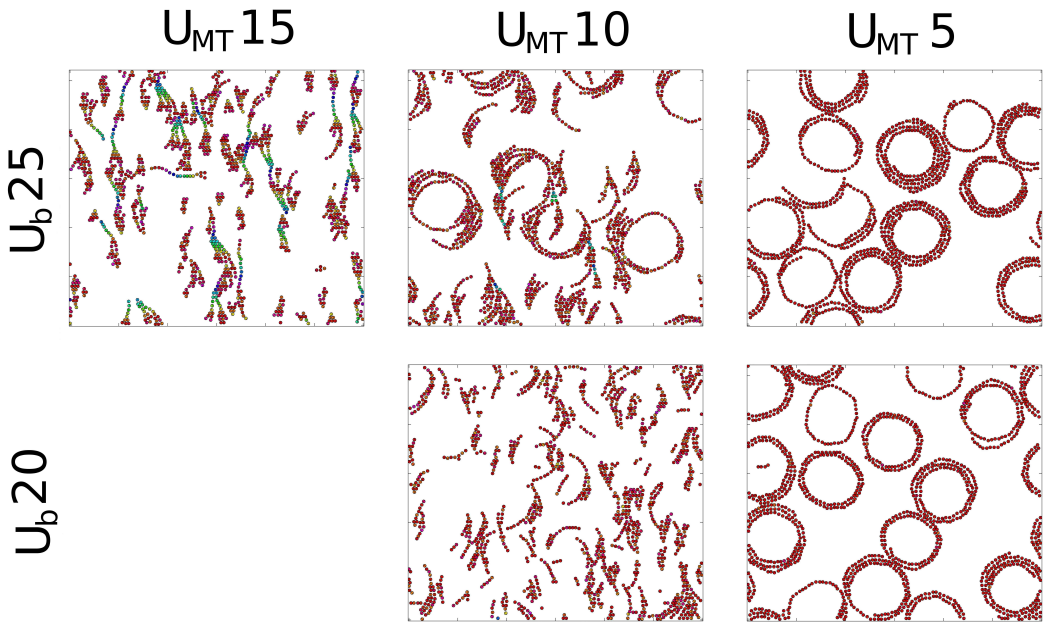

Figure 6.13: Phase diagram for anchoring angle $\varphi_0 = 0°$. Remember that colour represents the anchoring angle of the monomers.

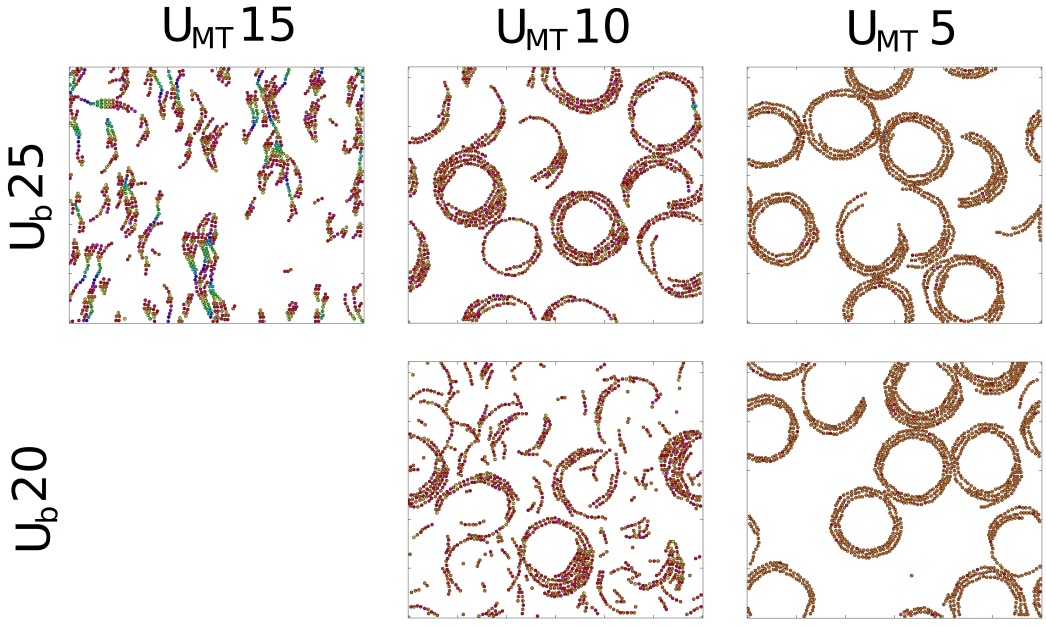

Figure 6.14: Phase diagram for anchoring angle $\varphi_0 = 30°$.

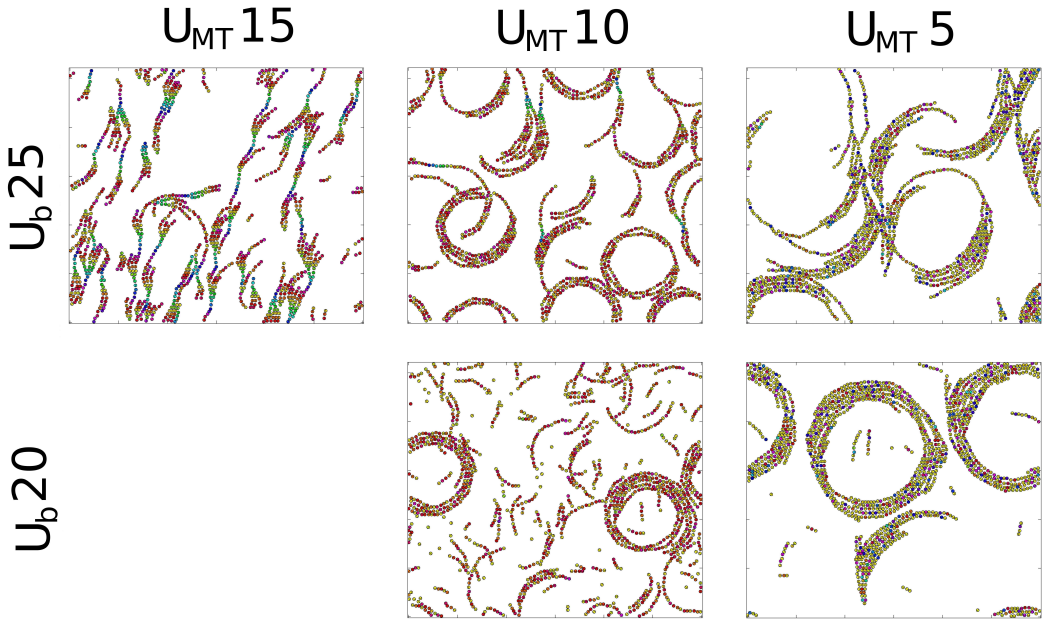

Figure 6.15: Phase diagram for anchoring angle $\varphi_0 = 60°$.

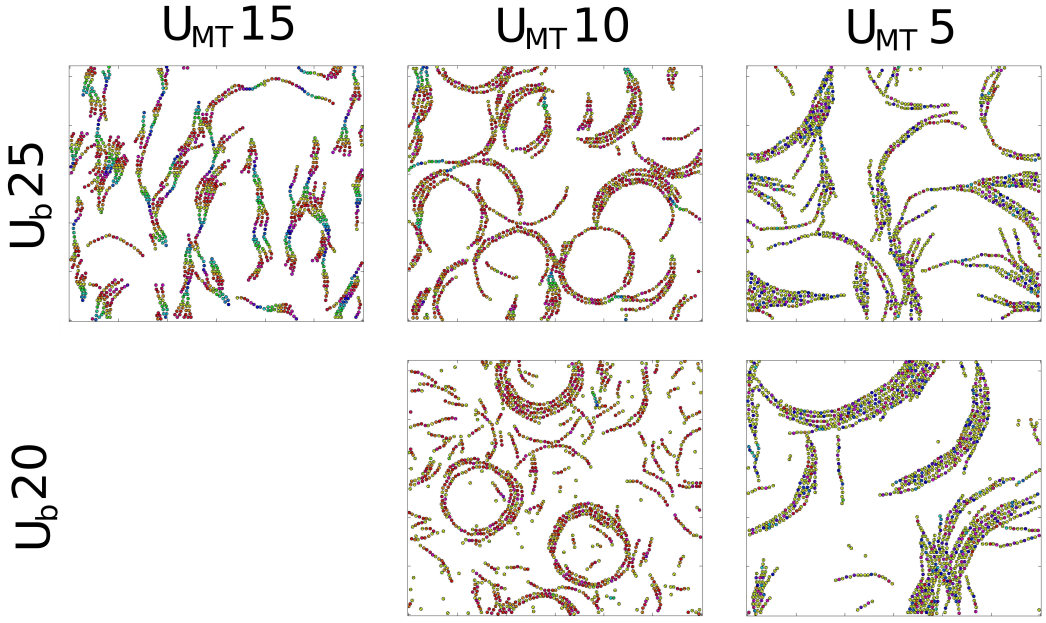

Figure 6.16: Phase diagram for anchoring angle $\varphi_0 = 75°$.

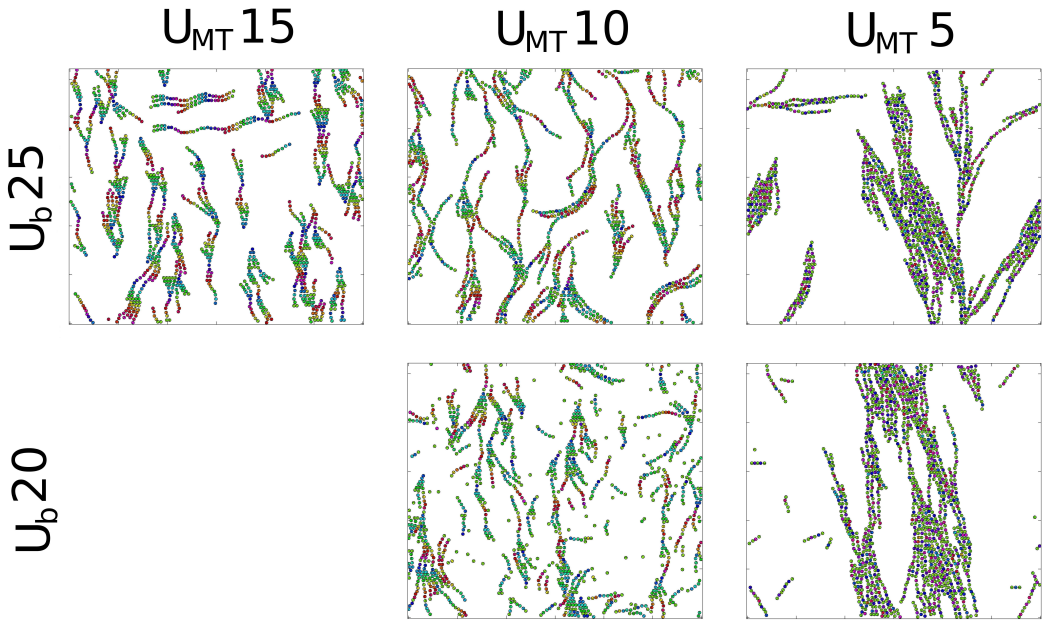

Figure 6.17: Phase diagram for anchoring angle $\varphi_0 = 90°$.

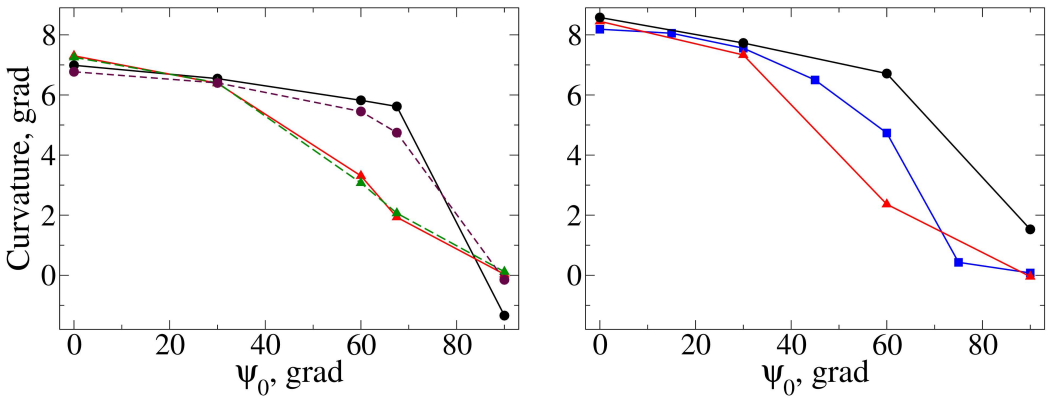

Figure 6.18: Average curvature of the filaments as a function of the preferred anchoring angle. The graph on the left uses the latest MD data (from a 40 ns simulation), while that on the right uses the first preliminary results (15 ns). Continuous lines are for simulations with $U_b = 20\,k_BT$, dashed lines for $U_b = 25\,k_BT$. Circles represent simulations with $U_{MT} = 10\,k_BT$, squares simulations with $U_{MT} = 7\,k_BT$, whereas with triangles $U_{MT} = 5\,k_BT$.

the growth of the anchoring value φ_0: for lower anchoring angles we see uniform rings of monomers with a well-defined anchoring value, but for larger values of φ_0 filaments begin to show a mixed population of well-anchored monomers and others very far from the ideal anchoring angle. This effect is different from the sawtooth anchoring explained above (see Fig. 6.12). Whereas the later was the result of a competence between anchoring and torsion, the new effect is related to the competence between torsion and the cost of keeping a bond on-plane as φ_0 grows. This energetic cost will favour large values of torsion because, as the sketch below shows, this will keep the bond close to the surface while allowing approximately half of the monomers to maintain a perfect anchoring.

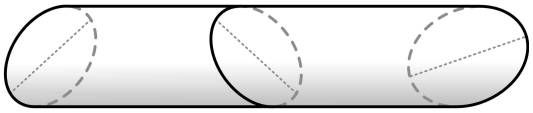

Figure 6.19: Sketch showing how torsion values of $\pi + \psi_0$ rad produce bonds that lie naturally on-plane.

In order to better understand the effects of torsion itself and separate them, from example, from the effects of having improved the angular resolution from 15° to 1°, or having changed the interaction algorithm for the bonds, we performed a series of modified simulations. There are three main ways in which we can cancel the torsion in the model: in the first place we can eliminate torsion processes altogether, that is to say, monomers will begin the simulation with a given anchoring value and they will not be able to modify it through the dynamics. This should provide a model similar to that of chapter 3 but with increased angular resolution and the new interaction model provided by the MD simulations. The results can be seen in figures 6.20 and 6.21. Of the four examples given, the case for $\varphi_0 = 60°$ and $\beta U_{MT} = 5$ is the one where monomers in the regular model are closer to the preferred anchoring value φ_0, so it is natural that the results without torsion should be more similar in this case. For $\varphi_0 = 90°$ and $\beta U_{MT} = 5$ the differences between the complete model and that with no torsion are more important, because the large *jumps* in torsion (see Fig. 6.19) induce branching and thus limit the dominant aggregation seen in the case without torsion. For $\beta U_{MT} = 10$, both $\varphi_0 = 60°$ and $\varphi_0 = 90°$ show disperse monomers and very short filaments. This is because, torsion processes not being available, bonds (with $\psi = 0$ rad) will be weakened by $U_{MT} = 10\,k_BT$, and the resulting interaction is not strong enough to promote aggregation. In the complete model filaments can

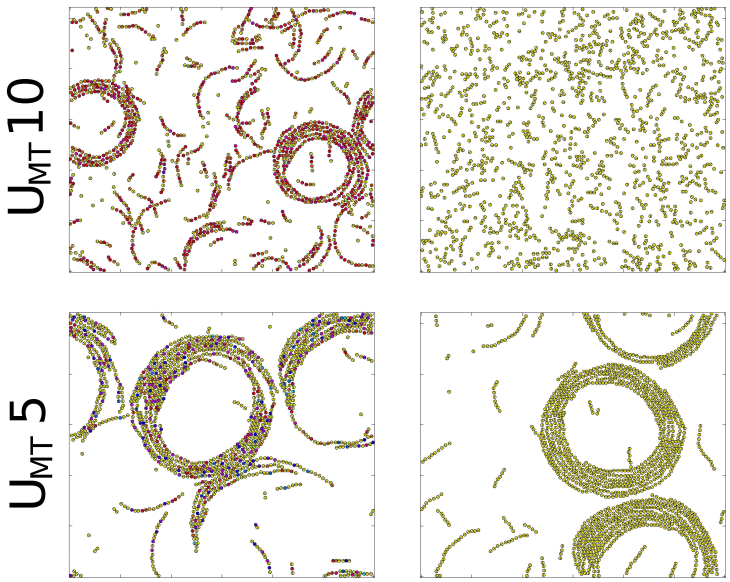

Figure 6.20: Regular simulations *versus* a modified version of the program without torsion. Preferred anchoring angle is 60° and $\beta U_b = 20$.

either sacrifice anchoring for torsion ($\varphi_0 = 90°$) or adopt the sawtooth anchoring-angle profile ($\varphi_0 = 60°$ and see figure 6.12), so aggregates and filaments are again possible with $\beta U_{MT} = 10$. Further increase of the bonding energy U_b for the model without torsion should produce results similar to those for $\beta U_{MT} = 5$.

Another way to explore the effects of having no torsion is to leave the model as it is, but assume $\psi_0 = 0°$. This should produce filaments with the same properties as those described by the MD simulations, but with no net torsion and helicity. This is specially interesting since torsion will always be possible, even when the preferred torsion is zero and thus torsion is not desirable for any given free-bond. Figure 6.22 compares these two situations, with $\psi_0 \simeq 29°$ and $\psi_0 = 0°$. The first case (for $\beta U_b = 20$ and $\beta U_{MT} = 10$) has already been commented above, however, when there is no torsion we find very unusual results: in the first instance (first line, $\varphi_0 = 30°$) we see many protein rings of two very different colours. The orange rings are well-attached rings, with $\varphi \simeq 30°$, while the blue rings have an anchoring value of $\varphi \simeq 180°$. Of course this value is very far from the optimal 30°, so these rings take no advantage of the interaction energy. Then why are they stable? In this situation ($\varphi \simeq 180°$ and also for $\varphi \simeq 0°$) bonds lie on-plane with no energy penalty, so filaments can be trapped in a meta-stable configuration. Surely the optimal states requires $\varphi \simeq 30°$ (which implies a little energy penalty to hold bonds on-plane but this is largely compensated by the anchoring interaction) but to go from $\varphi \simeq 180°$ to $\varphi \simeq 30°$ the intermediate angles provide an energy

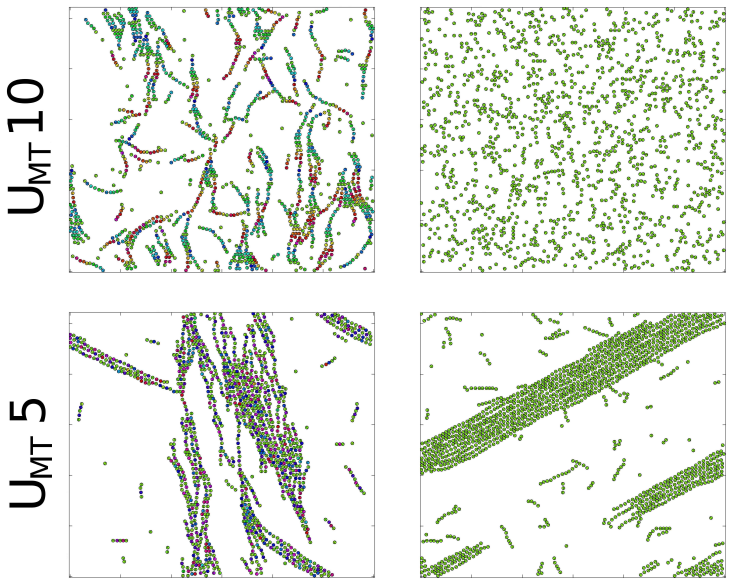

Figure 6.21: Regular simulations *versus* a modified version of the program without torsion. Preferred anchoring angle is 90° and$\beta U_b = 20$.

barrier that is enough to hold filaments in the local minimum. 30° and 0° are close enough that we do not see any rings trapped in 0°. Of course this only affects bonds, but not free monomers, which are free to rotate towards the optimal anchoring angles. This means that, for very long times, the system will eventually be formed by well-attached rings.

It is interesting to note how this situation is entirely new to the case without torsion. When $\psi_0 \simeq 29°$ the natural twist of the filaments is an efficient mechanism to avoid local minima and find the best configuration possible. The next two examples without torsion (for $\varphi_0 \simeq 60°$ and $\varphi_0 \simeq 90°$) show very similar results, but a bit different from the previous case. In these new simulations we find blue rings ($\varphi \simeq 180°$), red rings ($\varphi \simeq 0°$) and well-anchored filaments with either $\varphi \simeq 60°$ (yellow) or $\varphi \simeq 90°$ (green). Notice how these new preferred anchoring are far enough from 0° that we can now find filaments trapped in this new local minimum, unlike the case for $\varphi_0 \simeq 30°$. We can conclude that the natural torsion of the filaments helps them explore different configurations and find the optimal state, avoiding meta-stable minima.

The second figure ($\beta U_b = 25$ and $\beta U_{MT} = 15$, Fig. 6.23) yields almost identical results for $\psi_0 = 0°$, but completely different aggregates in the case with torsion. The change from $\beta U_b = 20$ to $\beta U_b = 25$ in unimportant since, in the first case, the energy was already high enough for the formation of filaments with almost no free monomers. The other parameter, βU_{MT} does not seem as relevant with $\psi_0 = 0°$,

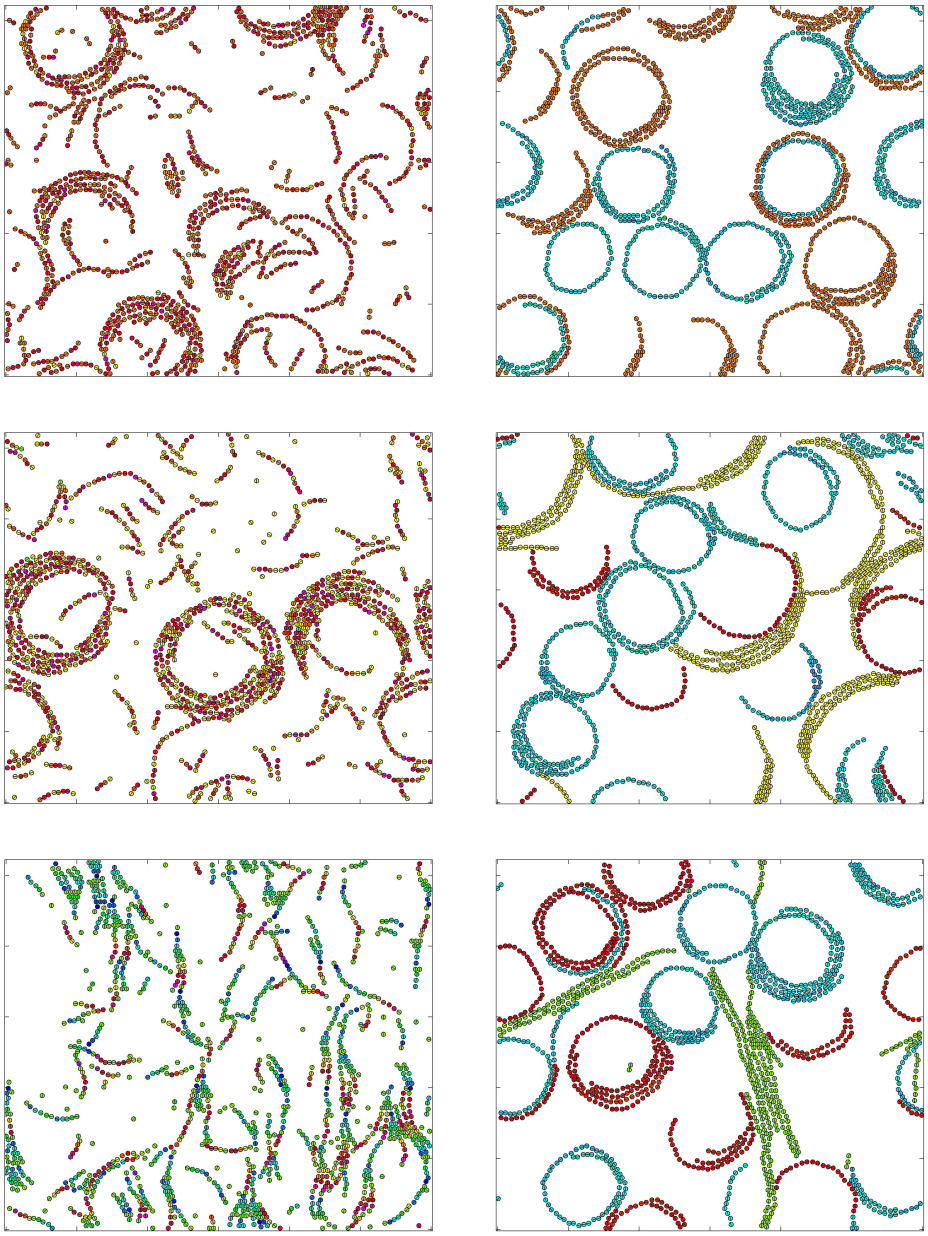

Figure 6.22: Original model—left column, $\psi_0 \simeq 29°$—*versus* $\psi_0 = 0°$. The preferred anchoring angle is $\varphi_0 = 30°$, $\varphi_0 = 60°$ and $\varphi_0 = 90°$ for each line respectively. $\beta U_b = 20$, $\beta U_{MT} = 10$.

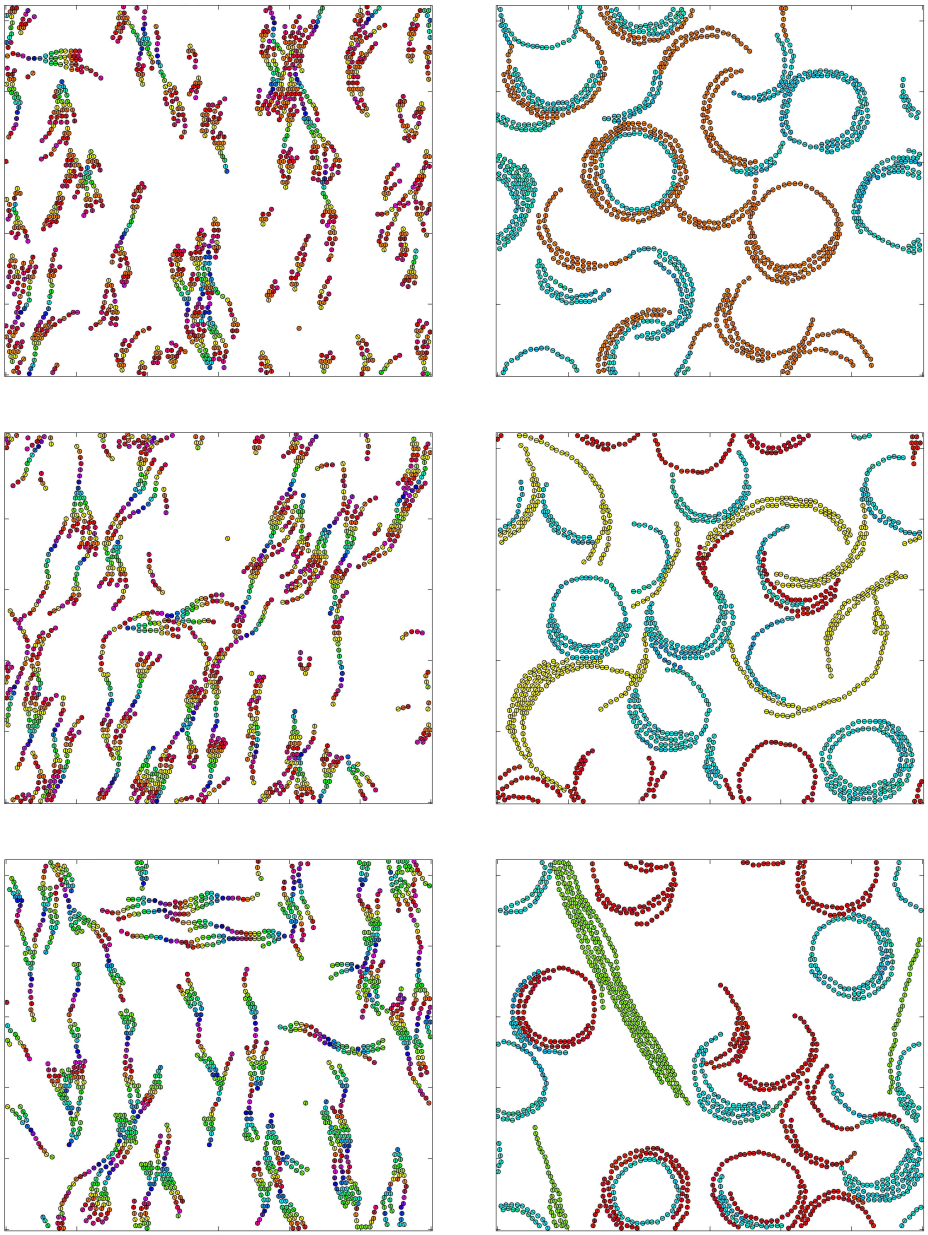

Figure 6.23: Original model—left column, $\psi_0 \simeq 29°$—*versus* $\psi_0 = 0°$. The preferred anchoring angle is $\varphi_0 = 30°$, $\varphi_0 = 60°$ and $\varphi_0 = 90°$ for each line respectively. $\beta U_b = 25$, $\beta U_{MT} = 15$.

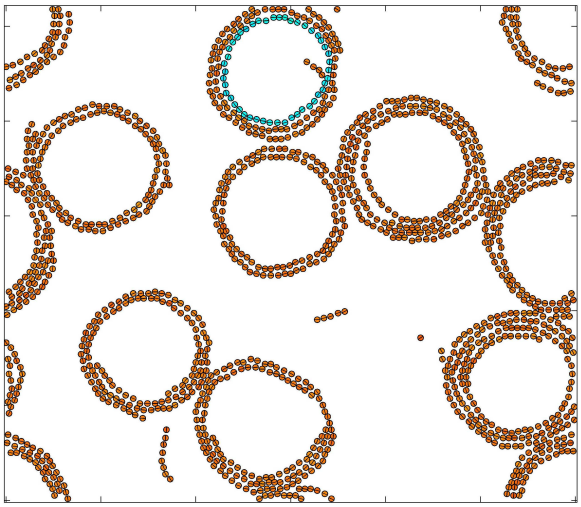

Figure 6.24: Simulations with no twist ($\psi_0 = 0°$), preferred anchoring angle $\varphi_0 = 30°$ and $\beta U_b = 15$, $\beta U_{MT} = 10$.

because there is no interaction trying to push bonds far from their natural twist. In the case with regular torsion ($\psi_0 = 29°$) we explained how anchoring—aiming for untwisted well-anchored filaments—competes with the natural torsion of the filaments. In Figure 6.22 anchoring is dominant and so we find rings, while in Figure 6.23 the new balance produces filaments that favour torsion. Filaments with torsion are more sensitive to changes in the interaction parameters, which could be good, because we know that cell-division processes are timed by weak biochemical signals—which could trigger configuration changes in sensitive FtsZ filaments.

Finally, we can see in Figure 6.24 how if the longitudinal bond is made weaker, then it is more difficult for filaments to be trapped in meta-stable configurations even if there is no torsion ($\psi_0 = 0°$). This is because more bonds will break, producing more free monomers which can explore different anchoring angles at no cost. Having weaker interactions can produce a more dynamic and adaptable system.

6.3 Some remarks on torsion and anchoring

In this chapter we have developed a model for FtsZ on a surface that considers torsion and different anchoring conditions. The main motivation behind the expansion of the model introduced in chapter 3 was to understand the new aggregates observed *in vitro* when working with FtsZ mutants on a lipid bilayer.

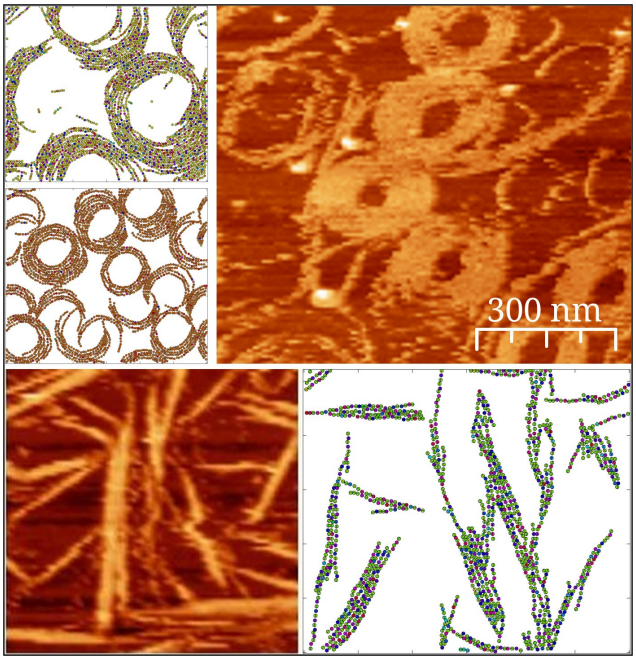

Figure 6.25: Orange images are AFM pictures of FtsZ. The image above is for protein on mica, and the snapshot below corresponds to Cys2 mutant on lipid bilayer. The computer simulations were made with $\beta U_{MT} = 5$, and anchoring angle 60°, 30° and 90° from top to bottom.

Despite some limitations (described below) our simulations capture the diversity of the new results (Fig. 6.25). The variation of only one anchoring parameter is enough to go from ring-like structures (similar to those seen on mica) to straight bundles reminiscent of mutant FtsZ Cys2 aggregates.

However, there are still experimental results that challenge the possibilities of this model. For example, under some circumstances filaments appear to bundle in layers or structures with some volume, which is clearly out of the scope of this model. In other cases we can observe complex aggregates that cannot be reproduced by this model and which seem to be related to lipid segregation in the lipid membrane. This motivated the research in chapter 7.

We have presented here evidence of torsion in FtsZ filaments, both from our group [34] and from other sources (see, for example, the compelling work by S. Arumugam et al. [32]). This torsion is, not surprisingly, disputed by other groups. For instance, D. J. Turner et al. claim to find no helicity in cryoelectron microscopy images [43]. However, the resolution of the images they present is compatible with stretched helices like those in figures 5.14 or 6.17. The group of J. Hsin support the hydrolisis-driven division model with no torsion, but they

do present results with helicity [17, 18] (they either ignore this filament twist or disregard it as a supposed artefact of the simulation).

However, even if we assume that FtsZ filaments *in vivo* had no torsion (perhaps as the result of interactions with other agents) anchoring is a key element that is routinely being overlooked. This is one of the most important points in this thesis: anchoring is essential to determine the aggregates FtsZ will form on a surface, and is also intimately related to any force applied by FtsZ on the cellular membrane. This is particularly true of models where the orientation of the filaments is important, for example if curvature is believed to produce the constriction force. Because we know that FtsZ, FtsA and ZipA attach to the surface in a flexible way [9, 10], the hypothesis that other elements in the Z-ring module the anchoring orientation of FtsZ should be considered. The other possibility is that collective interactions amongst filaments are responsible for the specific orientation of the filaments, or perhaps in the end the Z-ring will be found to be formed by short filaments or helices where there would be no need for an specific anchoring orientation, constriction forces being produced by an altogether different mechanism.

Our simulations hinted that torsion may be an efficient way to explore different configurations and find the most convenient state for FtsZ filaments. We also saw how filaments with torsion are more sensitive to the parameters than those without it, which could be exploited by the cell to switch between different aggregates and so regulate division stages. However, because we found twist values far from the optimal angle for free bonds to be of importance, we had to include the new parameter U_{MT} in the model. Changes in this parameter produced remarkably different aggregates (figures 6.13 through 6.17). One might be tempted to disregard the possibility of being so far from the optimal torsion angle ($\psi_0 \simeq 29°$), but the filament-rings observed in AFM experiments suggest that there are indeed filaments with little to no torsion on the surface. (We have seen how curvature is proof of well-anchored filaments with no torsion.) An angular deviation of 29° may seem rather too much for a bond to stand without breaking, but part of this twist can be absorbed by the monomer itself, thus distributing the stress. In either case (having torsion *in vivo* or not), the study of how the FtsZ monomer-monomer bond behaves against torsion, close and far from its optimal value, should be given priority, and is an important requirement for any model involving torsion. Identifying the importance of this issue is another of the main results of this thesis work. With that new information on hand, the model we

have presented here could surely provide new interesting and reliable insight into FtsZ dynamics and its interaction with biological substrates.

Regarding hydrolysis, it may be interesting to consider the possibility that it affects not so much the bending angle of the bond, but rather the torsional properties of the monomer-monomer system. We have seen how changes in torsion—either in the preferred twist or its flexibility—can induce transitions between different aggregates.

7

Lipid-lipid interaction

In the experimental setup with FtsZ mutants, monomers bind to Distearoyl N-(3-Maleimido-1-oxopropyl)-L-Phosphatidylethanolamine (DSPE-MAL), which is mixed in the lipid bilayer made of different mixes of Dioleoyl Phosphatidylcholine (DOPC) and *E. coli* cardiolipin (ECCL). Because monomers are much bigger than membrane lipids, and each monomer binds to a single DSPE-MAL, a small fraction of this lipid will be enough for all the protein to attach to the surface. So far we have considered that all the membrane ingredients are well-mixed in a uniform substrate, but this is not always the case experimentally. It is well known that a mix of lipids on a membrane will have a tendency to segregate as a way to minimize energy—in opposition to entropy which favours mixing. Of course the biological situation is even more complex, and the membrane is laterally segregated into protein and lipid domains of different sizes and life times, which play an important role in signaling pathways, endocytosis, cell polarity and migration, neuronal growth and a variety of disease settings [52]. Lipid rafts are a well-known example of this complexity and domain segregation of biological membranes.

Different atomistic [53, 54] and coarse-grained [55, 56] models have been used to study phase separation in lipid mixtures [57, 58, 59, 60]. It has been proposed that the presence of membrane-bound proteins can account for the differences observed *in vivo* and *in vitro* [61, 62, 63] regarding stability, size and shape distribution of lipid domains. Models for the segregation of lipid phases under the presence of cytoskeletal proteins is challenging since it is important to include the self assembling properties of these proteins. The formation of

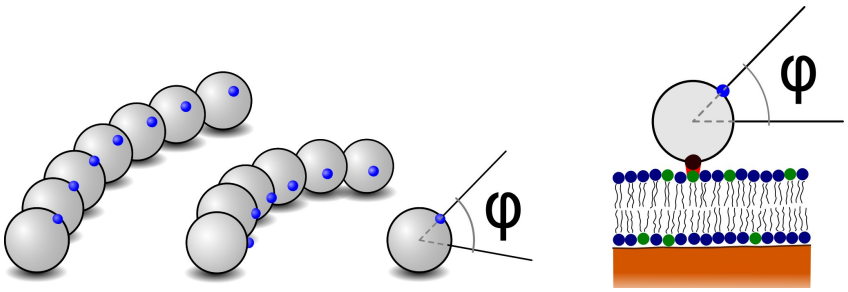

Figure 7.1: This scheme shows how the position of the cysteine (dark red) in the mutant with respect to the natural curvature of the filament (blue) defines the optimal curvature for the anchored filament. This cysteine will attach to maleimide lipids on the surface. [71]

filaments and bundles attached to the membrane with specific length, curvature and flexibility, may affect lipid segregation dynamics, and *vice versa*.

We decided to modify our fine-grained lattice model in order to study this interplay between lipid segregation and protein dynamics. The model has now two elements; a self-aggregating protein and a lipid bilayer with two lipid components. As was explained in section 6.2, the bacterial protein is bound with a known orientation to the head of one of the lipids (Fig. 7.1), which has a tendency to segregate from the other lipid component.

When experiments are performed at low temperatures (10–15° C or at linker lipid concentration ≥ 10%), we observe that protein filaments aggregate adopting unexpected surface distributions that are dependent on the orientation of the monomer on the surface. The modified fine-grained model allows us to rationalize the results observed under these special conditions. This model can also serve as a useful platform to study more complex situations in which both lipid and protein dynamics contribute to the lateral separation of membrane components.

7.1 Fine-grained model with lipid-lipid interaction

The core of the model is the same that was introduced in section 6.2. The energy between two monomers is given by

$$\begin{aligned} U\left(\varphi,\varphi',\theta\right) &= U_b + \kappa_\psi(1-\cos\left(\varphi-\varphi'+\psi_0\right)) \\ &\quad +\kappa_\theta\left[1+B\left(\varphi,\varphi'\right)-A\left(\varphi,\varphi'\right)\right] \\ &\quad +\frac{\kappa_\theta A(\varphi,\varphi')}{2}\left(\theta-\theta_M\left(\varphi,\varphi'\right)\right)^2 \end{aligned} \tag{7.1}$$

which is evaluated for all the neighbours in positions of the interaction crown, as seen in figure 3.1. A weak, non specific lateral interaction is also considered for any neighbouring monomers.

Since lipids are much smaller than monomers, proteins are not very sensitive to the precise spacial distribution of the lipids. Because of this, and also because it would be much easier to implement—and fast to execute—we decided to represent the lipids by a continuous field with a value for every lattice point. We introduce the density variable $\rho\left(\mathbf{R}\right)$, which takes values from -1 (pure DOPC, anchoring considered impossible in the model) to 1 (pure DSPE-MAL, perfect anchoring). Because DSPE-MAL is present in a smaller fraction than other lipids, we will focus on systems with $\overline{\rho}<0$.

As we mentioned in the introduction of this chapter, two opposing effects will explain the dynamics of the membrane in absence of interaction with the proteins: on the one hand, thermal fluctuations tend to mix the different lipids (maximizing entropy), while the self-affinity of the different lipids tries to segregate them (minimizing energy).

Our model will now have Montecarlo dynamics for the proteins, as usual, and also a parallel Montecarlo for the lipids. In these dynamics, the density of a random site exchanges a random density value with any of its neighbours (also chosen at random). Supposing both sites would remain within the limits $-1\leq\rho\leq 1$, the exchange is accepted or rejected according to the Metropolis algorithm, like it is done with the proteins. The energy is evaluated using

$$U_{lip} = -U_{ll}\sum_{\mathrm{nn}}\rho\left(\mathbf{R}\right)\rho\left(\mathbf{R}'\right), \tag{7.2}$$

considering the six nearest-neighbours of the two monomers involved in the process, and being careful to consider only once the interaction between the two monomers (because they are both a neighbour to the other). The factor U_{ll} will account for the strength of the lipid-lipid interaction. For a high value of U_{ll} (equivalent to low temperature) the interaction will be strong and there will be

segregation. On the other hand, a low value for U_{ll} (high temperature) will result in mixed lipids.

We have just mentioned that in this model there are two parallel dynamics; that of the proteins and the lipids dynamics. It is possible to adjust the relative speed of the two dynamics (by having one have several steps for each of the other). This could be used to model different systems with specific diffusion rates for the lipids and proteins.

The last ingredient in the model is the interaction between the lipids and the proteins through the anchoring potential. Proteins will have an anchoring potential equal to that of section 6.2, but it will be modulated by the density of DSPE-MAL in their lattice site. Remember we had this anchoring potential

$$U_{anchoring} = \min\left[-U_a + \kappa_a\left(\varphi_i - \varphi_0\right)^2,\ 0\right]. \tag{6.1}$$

We want to have no anchoring for $\rho = -1$ and regular anchoring for $\rho = 1$, so we can multiply the potential above by the factor

$$\tilde{\rho} = \frac{1}{2}\left(1 + \rho\left(\mathbf{R}\right)\right). \tag{7.3}$$

We can rearrange our factors so we have the following anchoring energy:

$$U_{anch} = U_{pl}\left(1 + \rho\left(\mathbf{R}_i\right)\right)\min\left[-1 + \kappa_a\left(\varphi_i - \varphi_0\right)^2,\ 0\right]. \tag{7.4}$$

Trying different values of φ_0 and U_{pl} will allow us to simulate different anchoring conditions for different FtsZ mutants, like we did in section 6.2. The Z93 mutant, with the cysteine in the 93 position of FtsZ, may be represented by a preferential angle $\varphi_0 \simeq 90°$, that anchors the protein filaments tightly with their natural curvature plane perpendicular to the substrate. On the other hand, the Z2 mutant is bound through the N-terminal loop, resulting in a more flexible binding which allows the protein filaments to avoid most of their elastic strain by taking their natural curvature closer to the substrate plane. We can use a value $\varphi_0 \simeq 30°$ to find filaments with a similar curvature to that observed in some AFM images for this mutant. The parameter U_{pl} measures the anchoring strength, so it should be expected to be larger for Z93 than for Z2, although we cannot aim to identify the model parameters that represent each FtsZ mutant to such precision.

Our new anchoring potential favours having DSPE-MAL under the proteins (or the proteins over their linking lipids). If there is an excess of DSPE-MAL under critical temperature, each protein may behave as a preferential nucleation site

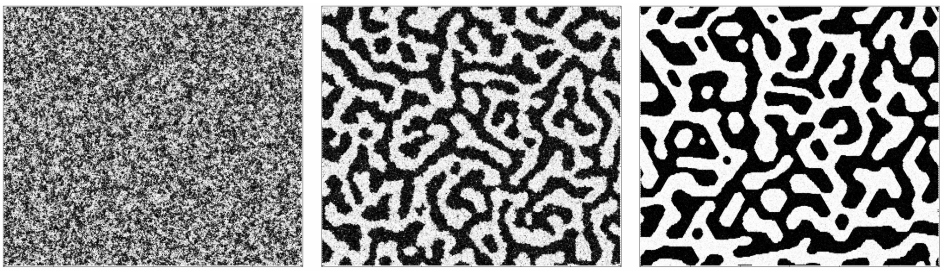

Figure 7.2: Symmetric mixture of two lipid species. From left to right, $T = 2\,U_{ll}/\mathrm{k_B}$, $T = 1\,U_{ll}/\mathrm{k_B}$ and $T = \frac{1}{3}\,U_{ll}/\mathrm{k_B}$. $T_c = 1.4\,U_{ll}/\mathrm{k_B}$.

for lipid droplets. As segregation advances the protein filaments should also try to adapt to DSPE-MAL aggregates.

Phase separation in a mixed lipid bilayer

In this section we will consider the lipid dynamics without proteins. If we have a a symmetric mixture of our two lipid species $\left(\overline{\rho} = 0\right)$ we will find segregation below the critical temperature ($T_c \simeq 1.4\,U_{ll}/\mathrm{k_B}$). The system will segregate into DSPE-MAL-rich phases with $\rho\,(\mathbf{R}) = \rho_t\,(T)$ and DOPC-rich pashes with $\rho\,(\mathbf{R}) = -\rho_t\,(T)$. Three examples are given in figure 7.2. As expected for a 2D phase transition, $\rho_t\,(T)$ increases rapidly $\left(\sim (T_c - T)^{1/8}\right)$ for T just below the critical temperature. Note that we have the condition that $\left|\rho\right| \leq 1$, so $\rho_t\,(T) \to 1$ for very low temperatures. If instead of a symmetric mixture we have $\overline{\rho} \neq 0$ we can have a homogeneous system for temperatures below the critical temperature $T_c \simeq 1.4\,U_{ll}/\mathrm{k_B}$, as long as $\left|\overline{\rho}\right| < \rho_t\,(T)$.

If we decrease the temperature of a homogeneous system we will find a spinodal decomposition into two phases. In a spinodal-decomposition segregation takes place all over the mixture, and it is driven by thermal fluctuations. This can be compared with other transitions, like crystallization, where there is an energy barrier to start the process and so the transition takes place around the initial nucleation point—this is why, if nucleation is prevented, liquid water can be found over and below boiling and freezing temperatures. The initial thermal fluctuations create clusters of density $\rho = \pm\rho_t\,(T)$, which grow in size with time. This process is increasingly slower, since it evolves through fluctuations in the boundary lines (see figure 7.4).

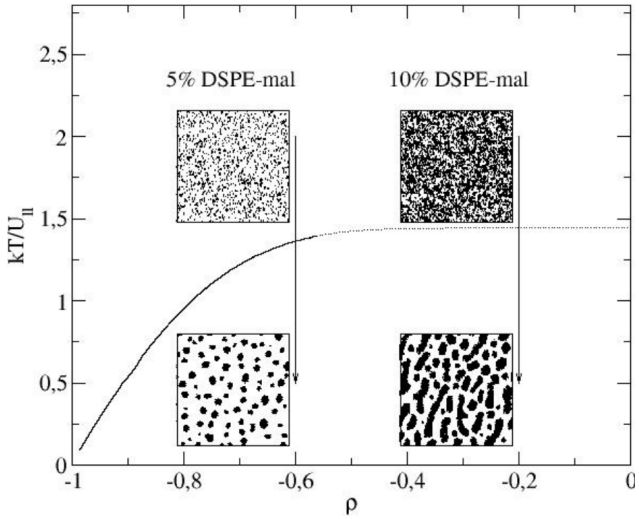

Figure 7.3: Phase diagram for the segregation of the two lipid species in our model of bilayer membrane, in absence of any protein. The lipids are mixed for temperatures above the line and they segregate in two phases below it. The mean density is only shown for negative values (i.e. where DSPE-MAL is the minority component). The MC simulations snapshots show (in grey) the local concentration of DSPE-MAL, with arrows marking a transition from $k_BT/U_{ll} = 2$ to $k_BT/U_{ll} = 0.5$. [71]

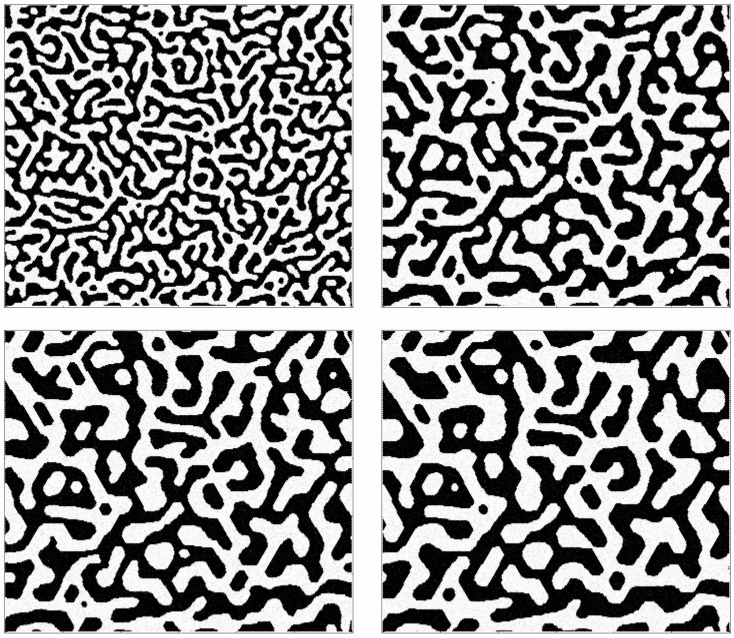

Figure 7.4: Evolution of an initially homogeneous mixture of lipids with temperature $T = \frac{1}{3} U_{ll}/k_B$. Snapshots show the system after 1, 4, 7 and 10 simulation steps.

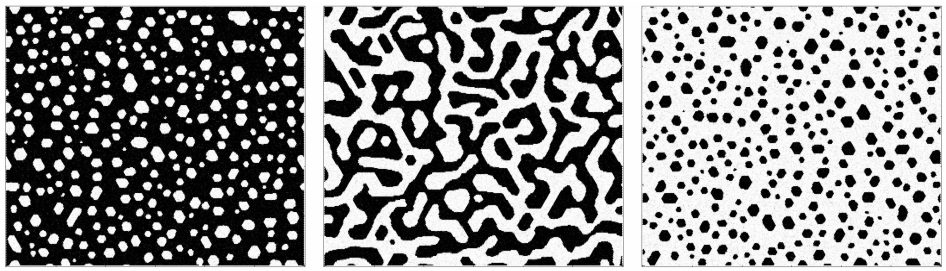

Figure 7.5: Three simulations with temperature $T = \frac{1}{3} U_{ll}/k_B$. The mean density is changed, and takes values $\overline{\rho} = -0.5$, $\overline{\rho} = 0.0$ and $\overline{\rho} = +0.5$ respectively.

This is easier to understand with non symmetric mixtures (figure 7.5), where there is one lipid in less concentration than the other. In this case, if $|\overline{\rho}| \geq \rho_t(T)$, the minority component will segregate into drops, which will slowly grow and fuse until eventually there is only one bigger drop. In this process the area of both phases is approximately constant, while the boundary line progressively decreases to its minimum when there is only one drop. This is the reason why the evolution is increasingly slower.

The AFM image in figure 7.6 shows a similar phase-transition pattern as those produced in our model (insets). The experimental image corresponds to a preparation with 10% DSPE-MAL and 90% DOPC, and it is roughly represented in our model by a value $\rho \simeq -0.2$; a 40% of the minority component. Note that the image was taken from the top to the bottom, so that time increases in that direction as well. Upon close inspection it becomes evident that the segregation domains in the AFM images are indeed growing from the top to the bottom, as predicted by the model.

Collective behaviour of the system with protein-lipid interaction

In figure 7.7 we have an example of the formation of filaments and aggregation of FtsZ on a homogeneous membrane which is above the segregation temperature. In this case the model is equivalent to that of section 6.2, where the lipid-lipid interaction was not considered. For this reason, we are interested in situations where segregation takes place. Because we want to focus on the new aspects of the model, we will use some typical interaction parameters from section 6.2

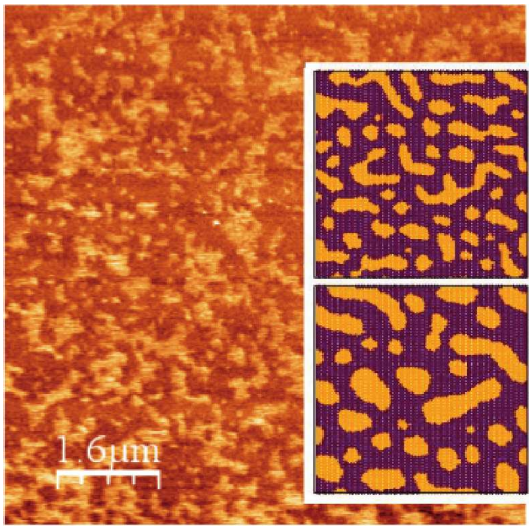

Figure 7.6: AFM image taken at 15° C of a supported bilayer membrane formed from a mixture of 90% DOPC and 10% DSPE-MAL lipids. The phase separation is observed in terms of the colour scale for the membrane thickness. The insets show snapshots of a MC simulation of our simple model for the segregation of the lipids, at $\mathbf{k_B T}/U_{ll} = 0.5$, $\overline{\rho} = -0.2$ and two different evolution times, in a ratio 1 (up) to 4 (down) from an initial random distribution. The colors correspond to local values $\rho > 0$ (orange) and $\rho < 0$ (maroon). [71]

($U_b/\mathrm{k_B T} = 20$, $U_{lat}/\mathrm{k_B T} = 0.5$, $U_{TM}/\mathrm{k_B T} = 10$). The anchoring conditions of mutant Z93 are crudely represented by $U_{pl}/\mathrm{k_B T} = 5$ and $\varphi_0 = 90°$.

When the temperature drops below the segregation point every anchored monomer will behave as a preferential nucleation site for the segregation of excess DSPE-MAL. At the same time, as segregation progresses, proteins will preferably stay within DSPE-MAL-rich domains. In figure 7.8 we can compare filaments over an homogeneous membrane (left) and over a segregated membrane (right), for two different choices of the lipid-protein anchoring strength—$U_{pl}/\mathrm{k_B T} = 5$ (top) and $U_{pl}/\mathrm{k_B T} = 15$ (bottom). The preferential anchoring orientation is set to $\varphi_0 = 30°$. The systems have evolved from initially random distributions of the lipids and proteins for up to 10^8 MC steps per protein monomer.

Once again, the results with a homogeneous substrate (left column) are very similar to those of the model without lipid-lipid interaction. Here we can see an interesting effect (that had also been observed in the previous model): the protein filaments are much shorter when we increase the anchoring strength. In this case the effect is so remarkable that FtsZ filaments have almost completely vanished in the case of strong anchoring. We can only understand this effect by taking into account the interplay between the natural torsion of the filaments and

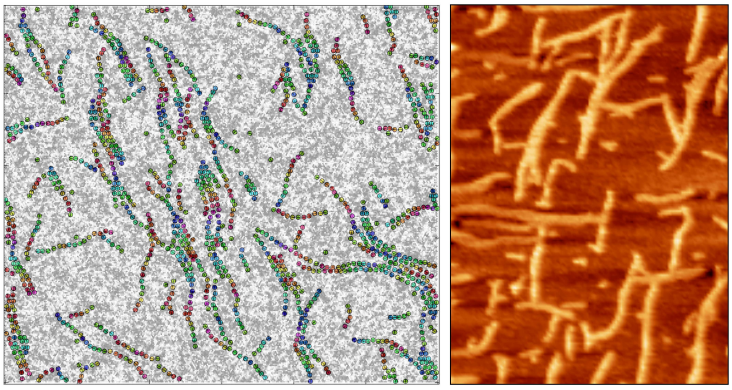

Figure 7.7: Snapshot of a MC simulation of the model (left) for $\overline{\rho} = 0$ and $k_BT/U_{ll} = 2$—above the lipid segregation temperature—and an AFM image for the Z93 mutant at room temperature and membrane composition 9:1 DOPC:DSPE-MAL, showing filaments and clustering on a uniform membrane. $U_{pl}/k_BT = 5$ and $\varphi_0 = 90°$. [71]

their preferential anchoring. When anchoring is weaker monomers have more freedom to explore different anchoring values and so they can find a balance between torsion and anchoring. If anchoring is much stronger this balance is broken and monomers have almost perfect anchoring and filaments cannot have any torsion at all (which means a weaker effective bond between monomers and thus shorter filaments). In the opposite case, where anchoring is much weaker, torsion will dominate over anchoring. The consequence is that curvature (which depends on an specific anchoring angle) disappears.

This suggests an interesting role of the FtsZ torsional structure: any molecular control on the link between the protein and the bilayer membrane may be used to enhance (looser link) or reduce (tighter link) the condensation of protein laments and bundles.

It has been shown how in figure 7.8 (left column) filaments do not form with strong anchoring. However, in the second column, filaments form both for strong and weak anchoring. This is because lipid segregation confines the proteins over reduced areas, and so the local density of FtsZ is increased. In some circumstances segregation (of the membrane) can promote aggregation (of the proteins).

Another consequence of the protein-lipid interaction is that protein filaments may provide the preferential spacial scale that was missing in the phase transition dynamics of the lipid bilayer. In section 7.1.1 it was explained how, when one of the lipid species is in lower concentration, lipid drops appear upon segregation,

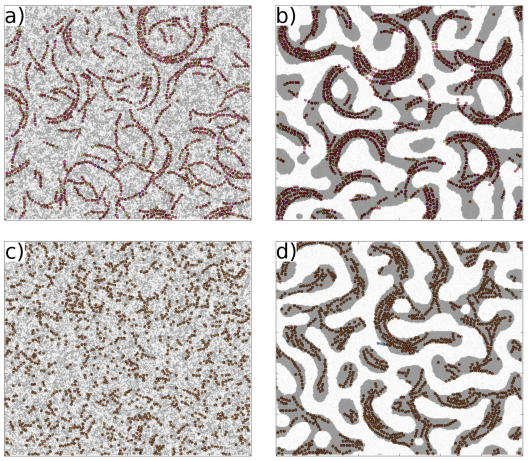

Figure 7.8: Snapshots of MC simulations for the protein-lipid model. The left column corresponds to a homogeneous membrane with $k_BT/U_{ll} = 2$, while on the right side there is segregation ($k_BT/U_{ll} = 0.5$). $U_{pl}/k_BT = 5$ (top) and $U_{pl}/k_BT = 15$ (bottom). $\varphi_0 = 90°$. [71]

and these drops grow until they are all fused into a single drop. When curved protein-filaments interact with this system they may stabilize lipid drops with a similar curvature.

Protein filaments in presence of small lipid domains, relaxation and memory effects

Different scenarios appear when the lipid segregation is first allowed to produce larger droplets of DSPE-MAL-rich lipid phase. The results observed in our MC simulations under these circumstances depend on the anchoring conditions and on the amount of protein. For protein monomers anchored with $\varphi_0 = 30°$ the preferential curvature of the filaments produce the structures shown in figure 7.9, with a concentration of the filaments in the periphery of the domain and a relative depletion of the protein at the center. We hypothesize that, on a larger system, these structures may stabilize 2D drops with a typical size similar to the spontaneous curvature of the protein filaments, as suggested by AFM images.

In contrast, MC simulations for filaments with preferential anchoring $\varphi_0 = 90°$ produce a very different pattern: a 2D nematic structure condensates in the interior of the drops, and excess FtsZ creates filaments without curvature which

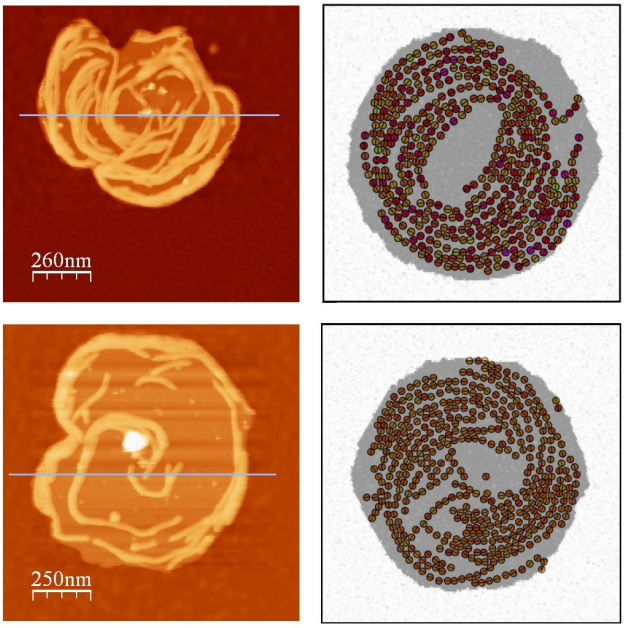

Figure 7.9: AFM images of a supported bilayer membrane formed from a mixture of 90% DOPC and 10% DSPE-MAL lipids with mutant Z2 on the bilayer after addition of GTP. Temperature 10° C. Right: Snapshots of MC simulations for the protein-lipid model at $k_BT/U_{ll} = 0.5$, below the lipid segregation temperature. The protein monomers were set randomly over the whole area, and they spontaneously concentrated and polymerized inside the pre-existing DSPE-MAL lipid-drop. Preferential angle $\varphi_0 = 30°$, and anchoring strength $U_{pl}/k_BT = 2.5$ (top) and $U_{pl}/k_BT = 5$ (down). [71]

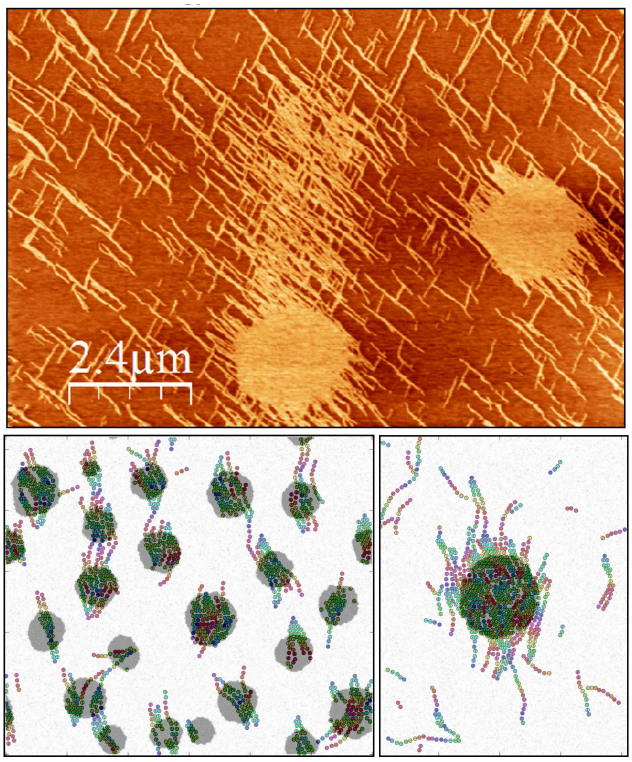

Figure 7.10: Experimental AFM image of mutant Z93 on a bilayer membrane con- taining 85% DOPC and 15% DSPE-MAL lipids. Bottom: Snapshots of the MC simulations with preferential angle $\varphi_0 = 90°$. The system with droplets (left side) was formed by increasing the lipid-lipid interaction value U_{ll} in a homogeneous system, while the single drop (right) was already formed at the beginning of the simulation. [71]

grow out of the drop among other filaments that form out of the drops. Figure 7.9 compares two MC simulations with an experimental AFM image for the FtsZ mutant Z93. Although we cannot expect our simple model to include all the complexity of the protein-protein and protein-membrane interactions, the clear similarities of the patterns in Fig. 7.9, and their contrast with those in Fig. 7.8, provide evidence that our model captures at least some of the essential aspects of these complex systems, and it may be used to explore the possible relevance of the different effects.

In the experimental setup the temperature was not always stable. In some cases it was risen over the segregation value in a system which had already formed domains like those in figures 7.8 or 7.9. We can reproduce that effect by lowering the lipid-lipid interaction parameter U_{ll}, as seen in figure 7.11. In the second column, which represents the concentration of DSPE-MAL under the monomers, we can see how the lipid-drop (black circle) disaggregates. However, the protein

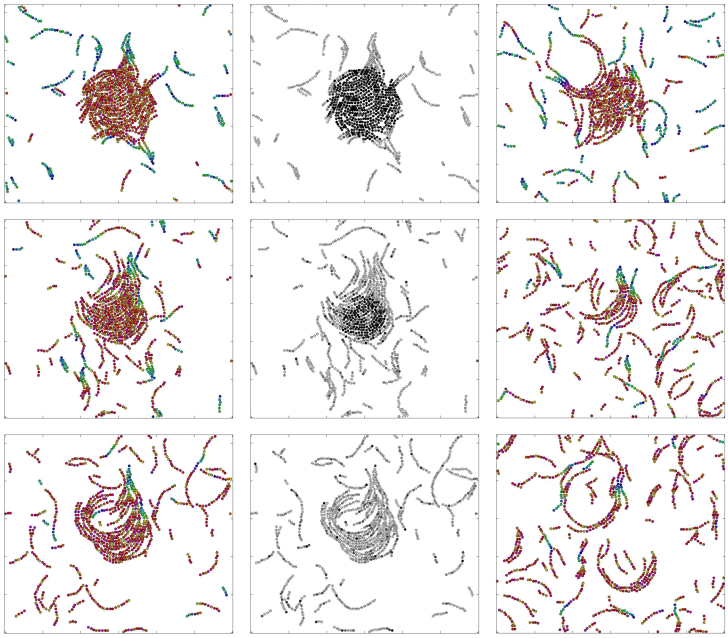

Figure 7.11: Snapshots of the MC simulations following the disaggregation of a DSPEMAL-rich drop that has nucleated a large cluster of FtsZ filaments. The temperature was set at $k_BT/U_{ll} = 0.5$ for the aggregation of the lipid drop, and $k_BT/U_{ll} = 1.43$ afterwards. The protein-membrane interactions parameters are $\varphi_0 = 90°$, $U_{pl}/k_BT = 0.5$. The first and third columns show protein monomers and their anchoring angle (colour). The middle column shows, in grey-scale, the value of the membrane composition parameter ρ (**R**) under each monomer for the simulations of the first column. From top to bottom, the DSPE-MAL drop (round cluster of black dots) shrinks and disappears. The protein filaments keep the global shape that was formed inside the drop. In the right column the dynamics of the lipids is four times faster. The first line corresponds to 10^7 MC steps after the change in temperature, the second to 4×10^7, and the last to 9×10^7 MC steps. [71]

aggregate that had gathered over the drop remains for some time after the drop has completely disappeared. This effect is much weaker if a faster lipid dynamics is assumed, as happens in the third column.

So far it has been shown how the interplay between lipid segregation and the anchored protein filaments affects their thermal equilibrium configurations. On top of that, it may also be crucial to set the time scales at which the protein filaments are assembled or disassembled. It has already been experimentaly observed that the diffusion of lipid molecules may be strongly affected by the presence of included proteins [64], and also that the lipid segregation processes may show strong out of equilibrium fluctuations [59, 61, 65]. Our model sug-

gests that the dynamics of the protein filaments may be strongly affected by the dynamics of the lipid membrane.

Who is leading whom?

The work presented so far shows that there is an interaction between proteins and lipids, however, one could ask whether it is the proteins that have to adapt to the lipids' dynamics or the lipids that are adapting their dynamics to those of the proteins. This question can be explored through the analysis of different simulations and the study of the dynamics of the proteins and lipids in each one. In particular, we studied the temporal correlation in the position of lipids and proteins.

We can keep track of the position of the proteins as a function of time for each of the typically 1350 monomers. This will allow us to know the average distance between proteins in a certain time and the same proteins at a different time. The same cannot be done for lipids, because they are represented as a continuous variable. Instead, we can evaluate the squared difference in the density value for the same lattice point at different times. For convenience, the scale of the density will be changed from $-1 \leq \rho \leq 1$ to $0 \leq \widetilde{\rho} \leq 1$.

The results of the simulations are presented in figure 7.12. For some time the simulations ran over critical temperature ($k_B T/U_{ll} = 2.5$) allowing for the formation of some FtsZ filaments. Then the temperature is reduced below this critical value. In the first case it is taken to $k_B T/U_{ll} = 1.\overline{3}$, just below the critical temperature, while in the second set of simulations the temperature is far lower; $k_B T/U_{ll} = 0.5$. Simulations were either the proteins or the lipids were not allowed to move were also carried out for both temperatures. (This was intended as control simulations for the dynamics of the lipids and proteins without crossed interaction.)

The most interesting result can already be appreciated by plain inspection of the snapshots in figure 7.12. It is clear how, when the temperature is closer to the critical value, the lipids tend to adapt to the filament-aggregates formed by the proteins. As a result, the system evolves a number of arched bundles with a curvature close to the optimal value for the proteins with this anchoring angle ($\varphi_0 = 30°$). For the lower temperature some of these arches may be found, but they are only formed and dissolved as the evolving underlying lipid substrate

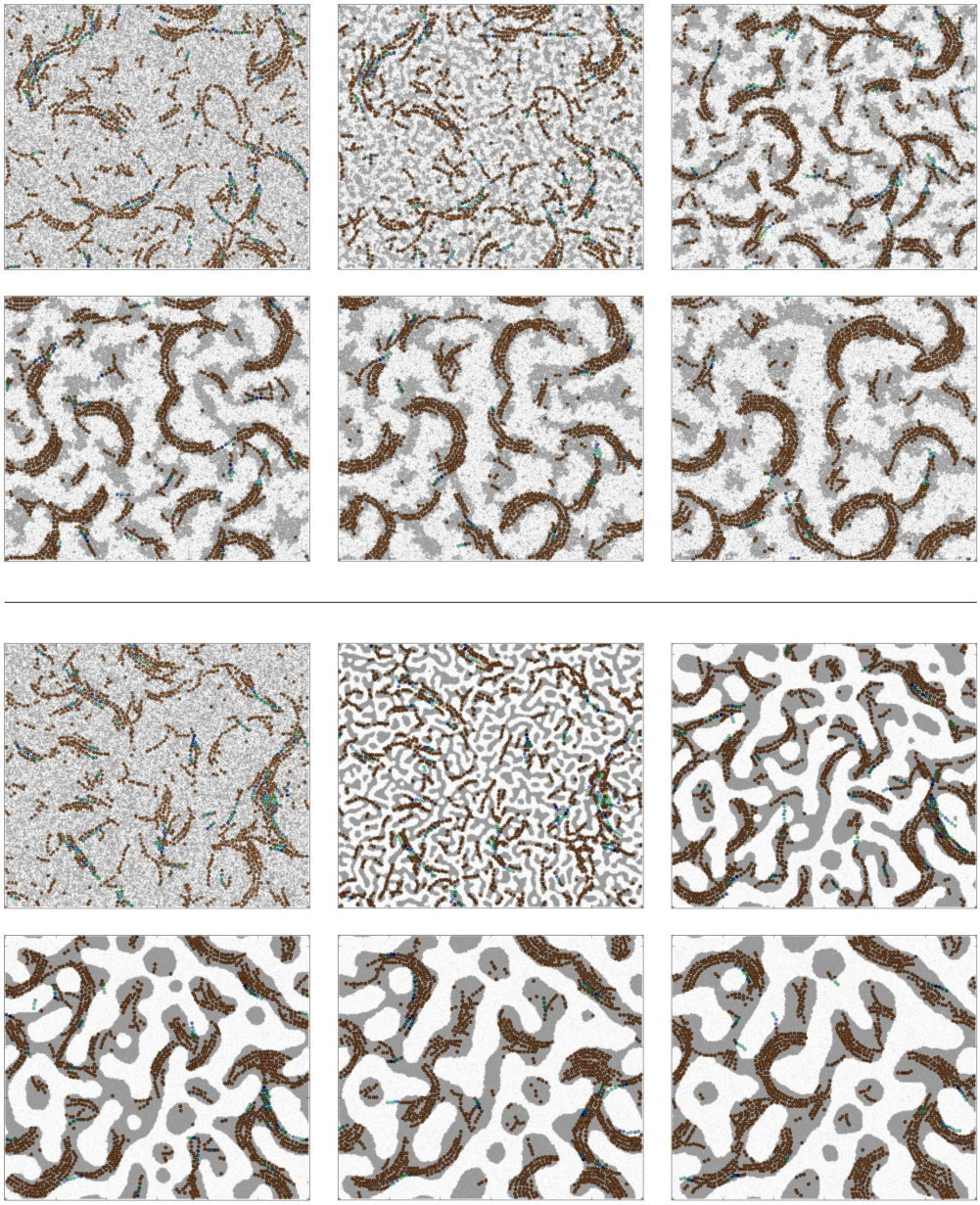

Figure 7.12: Comparative evolution of two identical systems, where only the temperature differs. A strong coupling was chosen—$U_{pl}/k_BT = 15$. In the first snapshot of both series the system had evolved over critical temperature ($k_BT/U_{ll} = 2.5$). For the rest of the snapshots the temperature was set to $k_BT/U_{ll} = 1.\overline{3}$ in the first series and $k_BT/U_{ll} = 0.5$ in the second series. The simulation times after the first snapshot are: 1, 50, 100, 150 and 200 ($\times 6.5 \cdot 10^4$ protein trials per monomer, and four times as many for the lipids).

allows, and there are many other filament aggregates where these arches do not fit.

This can be better understood with the statistical analysis of the system. In figure 7.13 we have the variation in lipid densities in time. In the first line we can see $\left\langle \left(\widetilde{\rho}_t - \widetilde{\rho}_{t+3}\right)^2 \right\rangle$ (where 3 simulation steps is a relatively short time). At $t = 50$ the temperature drops below the critical temperature. The change from a mixed lipid system to segregation domains is marked by the peak at that time (being stronger for the second column where the final temperature is lower). After that the density variations drop with time as segregation progresses, specially with $k_B T/U_{ll} = 0.5$, where the lipids are almost *frozen* in their segregation domains. The case with $k_B T/U_{ll} = 1.\overline{3}$ has more lipid mobility, so there are more variations. The value of these variations is also higher since the lipids in the first column are adapting to the evolving protein filaments, while in the second case it is the proteins that have to adapt to the lipid domains (and so the lipids do not need to alter the segregation domains and the density map is more steady).

The results when proteins are not allowed to move are also shown in figure 7.13. In the case of $k_B T/U_{ll} = 1.\overline{3}$ the fact of having protein mobility or not has an important impact on the lipid density variations, proving that proteins are indeed affecting the dynamics of the lipids. For $k_B T/U_{ll} = 0.5$ the results barely depend on protein mobility. (This can best seen for $\Delta t = 50$ and $t = 180$. The case $t = 60$ is too close to the temperature change to show significant changes due to interaction with proteins.)

Figure 7.14 show the equivalent results for protein mobility. In particular we can see the average distance a given monomer has moved in a certain time interval. In this case the differences between the simulations with different temperatures are not easy to appreciate, with the exception of the peak for $\Delta t = 3$ and $t = 50$. Nonetheless, this is a revealing result, because an important difference was the expected result.

In figure 7.12 and previous simulations we could see how with strong segregation the protein monomers were restricted to move inside the DSPE-MAL-rich domains. However, with higher temperatures and not so strong segregation, proteins are free to move all along the simulation area. For this reason we expected higher mean distances in the first column of figure 7.14 than in the second.

In contrast with the expected results, the simulations show similar protein dynamics for both temperatures, with even slightly increased mobility in the second column (lower temperature). This result can be explained by the fact that,

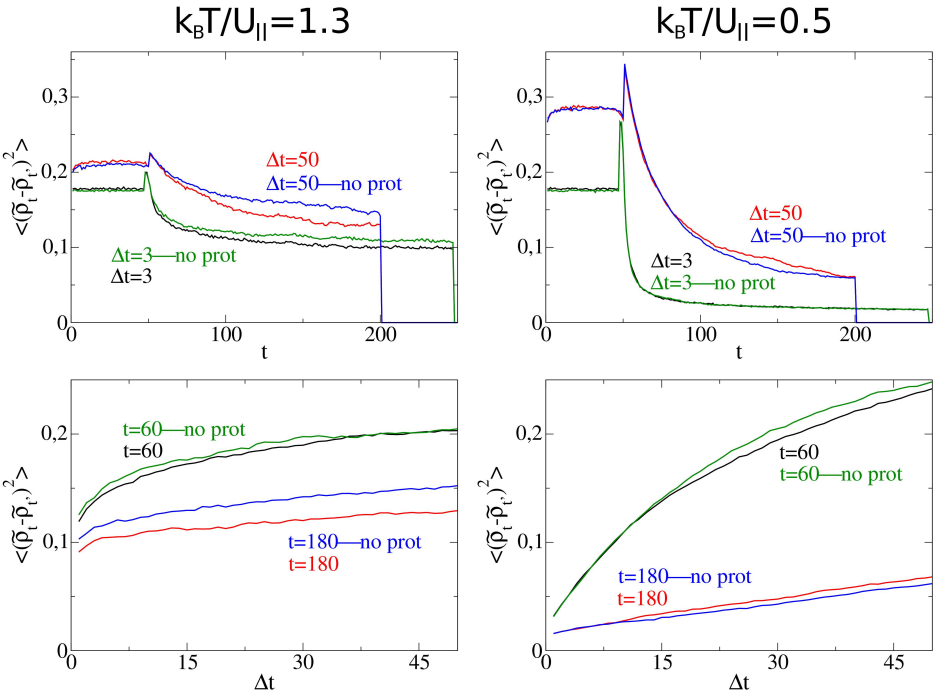

Figure 7.13: Average squared difference in the density values for the same lattice points at different times. The differences are evaluated for $t + \Delta t$, with time measured in simulation steps. In the first line $\Delta t = 3$ and $\Delta t = 50$ are shown for every value of t, while in the lower line $t = 60$ and $t = 180$ are shown for Δt up to $\Delta t = 50$. Note that at $t = 50$ the temperature drops below the critical temperature and segregation of the lipids occurs. Before $t = 50$ the temperature was $k_B T/U_{ll} = 2.5$ and then it was changed to the value shown for each column. For convenience, the scale of the density has been changed from $-1 \leq \rho \leq 1$ to $0 \leq \tilde{\rho} \leq 1$. The results correspond to a single simulation in each case.

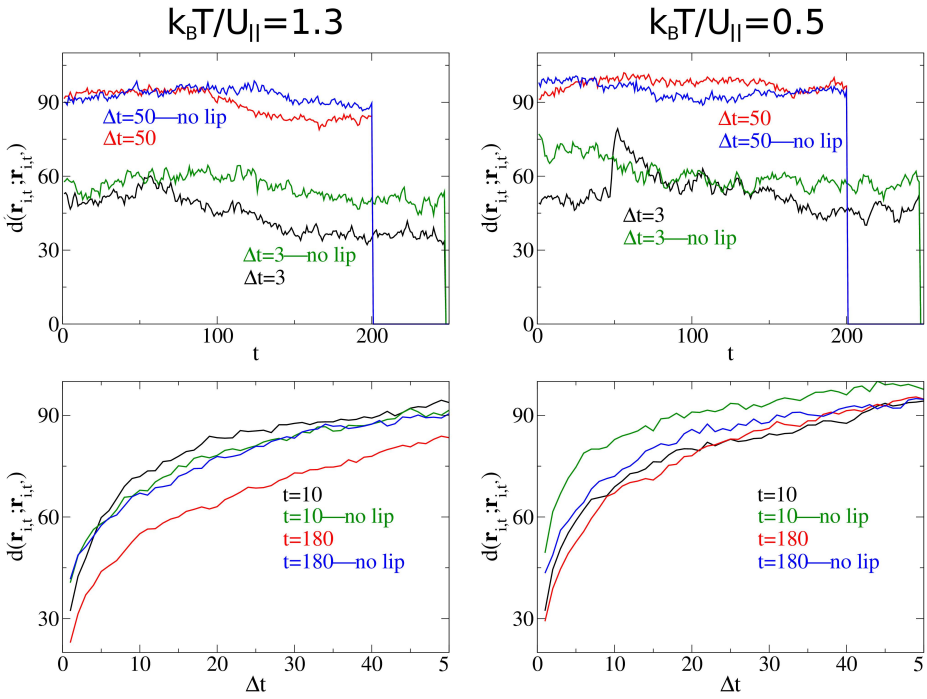

Figure 7.14: Average movement distance of the proteins between different times. The differences are evaluated for $t + \Delta t$, with time measured in simulation steps. In the first line $\Delta t = 3$ and $\Delta t = 50$ are shown for every value of t, while in the lower line $t = 10$ and $t = 180$ are shown for Δt up to $\Delta t = 50$. Note that at $t = 50$ the temperature drops below the critical temperature and segregation of the lipids occurs. Before $t = 50$ the temperature was $k_B T/U_{ll} = 2.5$ and then it was changed to the value shown for each column.. For convenience, the scale of the density has been changed from $-1 \leq \rho \leq 1$ to $0 \leq \widetilde{\rho} \leq 1$. The results correspond to a single simulation in each case.

with lower temperature, it is the proteins that are adapting to the lipid structures, while the opposite is true for higher temperatures. This means that with high temperature the proteins will simply develop their natural structures, and the lipids will adapt to them. With low temperature the filaments will have to adapt to the evolving lipid substrate.

In the centre of the last two snapshots in figure 7.12 we can see how a complete new arch has been formed when the lipid substrate allowed it. The result is that the protein monomers are indeed more restricted in their movement, but that whole filaments and aggregates are forced to adapt and dissolve as the lipid substrate dictates. These two opposed effects seem to have an almost equivalent impact and, for this reason, the protein mobility is similar to that of the simulations with higher temperature, where monomers are free to move but do not have to adapt to the lipid structures.

These simulations suggest that the temperature can control which agent will lead in the protein-lipid interaction. Lower temperatures produce a stronger segregation process where proteins will have to adapt to very rigid lipid domains, while higher temperatures produce more a dynamic lipid segregation that can adapt to the regular protein aggregates.

Discussion

In previous chapters we have discussed the rich behaviour of FtsZ aggregates when protein mutants are covalently attached to a supported lipid bilayer. Under these conditions, the monomers form the usual filaments and **I**-**C**-**O**-like aggregates 3. New elements, like the specific lateral-bond (U_{SL}) and filament torsion were introduced to explain novel behaviour induced by the new anchoring technique. However, the fine-grained lattice model was unable to reproduce the unexpected polymorphism observed when lipid segregation occurred (for low temperatures—$T \lesssim 10°\mathrm{C}$—or linker-lipid concentrations above 10% molar ratio).

There is great interest in studying lipid segregation both in model membranes and *in vivo*, as well as in exploring the role played by proteins in the reorganization of membrane lipids [56, 65, 66]. Previous studies have considered protein filaments as a fixed frame for the formation of lipid structures [62]. However, AFM images showing the formation and evolution of FtsZ filaments on a substrate presenting lipid segregation clearly indicate that these protein structures are very far from being rigid scaffolds.

These experimental results can only be reproduced by including both lipid and protein dynamics in the model, as well as an interaction between them. For this reason the lattice model was extended to include not only protein but also lipid dynamics. This model approximately reproduces the shapes of the protein aggregates observed when bound both to homogeneous lipid-bilayers and substrates presenting phase segregation.

The simulations also hint other interesting consequences of the interplay between lipid and protein aggregation. Lipid segregation can affect the length and curvature of the filaments formed on the surface. Fig. 7.8 (**c** and **d**) shows how lipid segregation can facilitate polymerization under conditions in which the tightness of the monomer anchoring to the membrane prevents the formation

of filaments, simply by increasing the local density of protein. This effect could be biologically relevant: it is known that, during bacterial cell division, the site where the Zring is located is enriched in certain lipids that can form domains [67] which could have a direct effect on the protein dynamics and the critical concentration of FtsZ.

Another interesting aspect of the lipid-protein interaction is that the dynamics of the formation and disintegration of lipid and protein aggregates are coupled to each other, but with different time scales, which may create long-term memory effects. The formation of protein filaments may be triggered or arrested through the control of GTP in the bath, while the lipid segregation on the bilayer membrane is very sensitive to changes of the temperature. Therefore, the experimental systems may be used to explore very different scenarios, in which either component may stabilize the formation of structures at the sub-micron scale driving the other one beyond their individual relaxation time.

In our model we may explore the complex time-dependent behavior that results from the coupling between lipid and protein aggregation through the change of the parameters. In section 7.1.4 we explored the effect of temperature in determining the leading role in the lipid-protein interaction, and the results in figure 7.11 illustrate how a protein cluster "remembers" the presence of a lipid domain which has already dissolved by an increase in temperature.

It is also possible to run MC simulations allowing for the segregation of the membrane in the presence of protein monomers without longitudinal bonding interaction. These bonds can be activated later to mimic the addition of GTP in the experimental system, and so we can observe the formation of protein filaments on pre-structured lipid bilayers.

Some of the lipid domains described in cell membranes, such as rafts, serve as signaling platforms [65] in which both proteins and lipids are present. The tools presented in this chapter could be useful to explore situations in which protein aggregation induced by ligand binding or changes in the local environment could affect the stabilization of rafts that trigger other biochemical responses [68].

It is clear that cell membranes and model systems including richer lipid mixtures have more complex behavior. The description we have used of the lipid membrane is the simplest model that incorporates lipid phase-segregation and protein dynamics. In our model membrane we have assumed constant and homogeneous diffusion rates for the lipids, both in the mixed and in the segregated phase. More complex dynamical patterns are expected to occur under diffusion-

limited segregation or for lipid bilayers with a more complex composition or structure.

Finally, it has been shown how the interplay between protein and lipid aggregation can give rise to an extremely rich dynamic and structural phenomenology in two dimensions. Macroscopic mechanical properties of the membrane are related to the microscopic details of membrane domain-formation and protein dynamics [69, 70], so this complexity may also have an important impact on local and macroscopic membrane mechanical properties.

8

Overview and conclusions

FtsZ and the Z-ring form a complex system, where many different proteins, lipids and other biological elements interact with each other to orchestrate the delicate division process. On top of that, the crowded, small size of prokaryotes makes it hard to explore the system from the experimental point of view. This explains why there have been many contradictory (and overconfident) research articles on the subject. Many of these (specially those concerned with hydrolysis) rely on crystallographic models of FtsZ, each of which have subtle differences that yield different conclusions if carelessly extrapolated to complete free filaments [18]. This is unsurprising, because the crystallographic models are taken from samples very far from their natural conditions (temperature, crowding...).

Molecular dynamics help to bridge these limitations by allowing monomers to reach equilibrium in a more realistic environment, but the technique has difficulties of its own; which ions should the simulation include? How long to simulate? How many monomers should be considered? Molecular dynamics is one of the best techniques to explore biological structures, but its results need to be regarded with the usual prudence in science, specially when different groups claim to find opposing results [1, 34, 36, 72].

In this context simplified experimental and theoretical approaches have been very useful, trying to isolate different aspects of the problem [16, 32] y buscar referencias en rojo...]. These isolated elements are easier to understand on their own, and the knowledge obtained about them can be applied to more complex situations where the same elements play a part. This was the motivation that started the AFM experiments by the group of Marisela Vélez. But even their

earliest, most simple experiments resulted to be too complex to understand without the help of complementary theoretical approaches [22].

The goal of our models is to extract the essential parameters governing the experimental system. For this reason, why try to reproduce the experimental results with as few elements as possible, leaving any other structural detail aside. Any interaction that can be excluded from the model, if the experimental results are still reproduced, cannot be relevant at that scale of analysis. This is crucial information for the experimental groups, who have to deal with too many parameters and interactions.

As good examples of this philosophy I would like to acknowledge the important contributions by the PhD students that preceded me in the group, Ines Hörger and Alfonso Páez. As part of their research, they helped to determine the role of weak lateral interactions in FtsZ aggregates on mica surfaces [27, 24]. This was in a time where the existence and role of this interaction was questioned [73]. Of course, such a simplified analysis cannot answer every question from the much more complex biological context. But they showed that the force is actually there and that, even if it is very small, (of the order of $0.5\,k_BT$ with longitudinal bonds of about $10\,k_BT$) it can have an important effect on FtsZ aggregates. *In vivo* this interaction could contribute to the generation of constriction force [23, 27] (which probably has no simple, unique origin) or perhaps it could work as an stabilization factor of the Z-ring.

One of the advantages of our fine-grained lattice model, at least in its latest versions, is that it is quite easy to include more detailed and non-isotropic interactions between monomers. When the experimental team of Marisela Vélez started working with FtsZ mutants, they observed more complex aggregates. This is because, working with mutants, they have some control over the anchoring orientation. If most monomers share a similar anchoring angle, this can enhance interactions that are hidden in uncontrolled attachment. We studied this effect by introducing a new orientation-dependent interaction. This new interaction is subtle and may not have a direct biological function. However, it allowed us to reproduce qualitative differences in new aggregates, which can be relevant considering the number of molecules in the division complex, any of which may affect monomer-monomer lateral interactions, an effect that can be amplified in bigger aggregates like the Z-ring.

As experimental research with FtsZ progressed, indirect evidence of torsion in FtsZ filaments started to accumulate [32], although there is still debate regarding

this question [43, 17]. With the aim of studying the bonds at the ends of FtsZ filaments, the group of Paulino Gómez-Puertas performed a series of molecular dynamics simulations with a protein pentamer. Their results did show a twist of the proto-filaments, which would elongate into rather stretched helices. We used these data to provide our model with the extra torsion dimension we needed to study the new experimental results of the experiments with FtsZ mutants.

It is easy to understand that monomers cannot have a precise anchoring angle while respecting the filament torsion. This conflict results in even richer aggregates, with many small filaments that try to balance both properties. Our simulations regarding torsion and specific anchoring have not solved the cellular division question, but they have helped to identify two of the most pressing limitations of current models:

Any model that attempts to explain the origin of constriction forces needs to address the details of FtsZ anchoring. This is specially important given the fact that FtsZ anchors through other proteins, FtsA and ZipA, in a rather flexible way [9, 8]. Consider, for example, the curvature-induced constriction models. These claim that an increase in the curvature of the filaments (usually driven by hydrolysis) will trigger the division process. However, they fail to explain why this curvature will be produced in the perpendicular plane with respect to the membrane, as opposed to forming curling filaments on the surface, which does not have to deal with the energy requirements of bending the membrane. This does not mean such models must be incorrect, only that they need to face these difficulties, which are usually taken for granted. In addition, the orientation of the bending plane is a new parameter that the cell could be using to control Z-ring dynamics, which may explain why the anchoring of FtsZ seems to be so flexible (allowing for a transition from flexible to stiff anchoring with the intervention of other proteins).

Related with the previous point is the need for a precise model of the behaviour of FtsZ bonds against torsion. Because this information is currently unavailable, we had to work with an extra free parameter in our simulations, and it turned out to be one of the most important factors that determine protein aggregates. It is essential to know whether FtsZ bonds are flexible in torsion, if they can have a weak interaction energy for large twists or whether they completely break if torsion is not close to the ideal value.

The last expansion of the model explored segregation phenomena in the lipid membrane. This was motivated by a series of experiments at lower temperatures,

which resulted in aggregates that could not be understood with the previous model. The simulations could reproduce some of these aggregates at a qualitative level, and we could also observe other interesting effects:

This model describes the mutual interaction of the dynamics of lipids and proteins, but we had to determine which was playing the most active role in this interaction. Were the proteins adapting their dynamics to the lipid segregation? Or were lipid segregation adapting to protein aggregation? Close inspection of the results prove that this depends on the conditions of the simulation. In particular, higher temperatures increase lipid mobility (even when segregation occurs) and lipids can adapt to the natural structures of the proteins. At lower temperatures segregation is too rigid and it is the proteins that need to adapt to the lipid domains.

We also observed how, when there is lipid segregation, proteins gather over linking-lipids domains, which increases the local protein density. In this way, lipid segregation can induce protein aggregation in a system that was originally below the critical density value. Since some people consider that the division region may be enriched in certain lipids [74, 75, 76], this could have a role *in vivo* helping to localize the Z-ring in space and time.

Our fine-grained lattice model has proved useful and very versatile, and it still has room for improvement. For example, we assumed in our models that the positions of the protein filaments are limited to a planar surface. However, there is some recent experimental evidence that multi-layer protein structures may also appear (not published), and this is perhaps an important effect under some circumstances.

Refining the bonding details to allow for hydrolysis processes should be an easier upgrade of the model. This would overcome most of the challenges and limitations in our research with square-lattice models and hydrolysis (see chapter 4). However, it is important to take into account that introducing more complexity in the model will not necessarily make it more useful. The main idea behind this thesis project was to include only the essential detail to reproduce the desired experimental results.

9

Conclusiones

These closing conclusions are written in Spanish as required by the Spanish Government for thesis manuscripts in a foreign language.

El trabajo presentado en esta memoria se fundamenta en los novedosos estudios experimentales con mutantes de FtsZ. Al disponer estos mutantes sobre una bicapa lipídica se consigue un imperfecto control de su orientación sobre el plano, lo que se traduce en un nuevo abanico de agregados.

En primer lugar se estudió cómo este control de la orientación sobre el plano puede amplificar pequeñas interacciones entre proteínas que resulten en variaciones de las estructuras anteriormente descritas en los experimentos sobre mica. Estas interacciones colectivas no alteran la esencia de la dinámica de FtsZ, pero ponen de relieve cómo pequeñas interacciones a escala local pueden alterar el aspecto global de los agregados, lo que podría ocurrir *in vivo* si cualquiera de las múltiples moléculas involucradas en el proceso de división modulase sutilmente las interacciones laterales de FtsZ.

También a lo largo de este proyecto de tesis se estudió, en un modelo más sencillo de red cuadrada, el efecto de introducir de forma explícita el ciclo de hidrólisis en la dinámica. Esto tiene un importante inconveniente en la necesidad de introducir nuevos parámetros en el modelo, pese a los esfuerzos por minimizar este problema. Los resultados también destacaron la importancia de no considerar la curvatura de los filamentos, ya que esto afecta de forma notable a la movilidad de los filamentos y a su capacidad de interacción. Pese a estas dificultades, el modelo ofreció información muy detallada sobre el intercambio

de monómeros entre filamentos y agregados y cómo dicho intercambio está determinado por las distintas variables del problema.

La mayor parte del trabajo se ha concentrado en la exploración del papel de la torsión en FtsZ, lo cual supuso añadir una nueva dimensión al modelo de red. La torsión se estudió en primer lugar mediante una aproximación analítica y un modelo de filamentos ideales, lo cual permitió obtener unos resultados provisionales—pero valiosos—relacionando la forma y rigidez de los filamentos con los detalles del anclaje al plano. Posteriormente se exploró este efecto en el modelo de red fina, lo cual permite tener en cuenta los efectos colectivos entre filamentos, los procesos de ruptura, etc. Los resultados son muy interesantes, y muestran cómo el ángulo de anclaje puede explicar la transición entre agregados muy diferentes, desde anillos a filamentos aparentemente rectos. Esto podría tener relevancia biológica como mecanismo de transición entre distintas fases de la división.

Durante esta fase de trabajo se identificaron dos aspectos de gran importancia. En primer lugar, quedó demostrado el papel crucial del anclaje en la dinámica de FtsZ. El anclaje debe ser, por tanto, un elemento necesario en futuros modelos que traten de explicar el origen de la fuerza de constricción en la división celular, y deben tomarse con mucha cautela los modelos actuales que no solo no lo hacen, sino que, de hecho, presuponen los efectos más ventajosos para su modelo. Las simulaciones presentadas en esta memoria también sirven para identificar la importancia del comportamiento del enlace de FtsZ frente a torsión. Los resultados de dinámica molecular ofrecen información de confianza sobre enlaces con valores de torsión cercanos al equilibrio, ¿pero qué ocurre cuando el anclaje trata de forzar esta situación? Esta incógnita, traducida en una variable libre en nuestro modelo de enlace, determina el aspecto final de los agregados. Dado que muchos modelos presuponen un anclaje sin torsión (donde el anclaje forzaría a deshacer la torsión natural de los enlaces) responder a esta cuestión es también de gran importancia para el campo.

Por último se exploró el efecto de la segregación de lípidos en el sustrato al trabajar a menores temperaturas o diferentes concentraciones. El resultado es una plataforma que podría generalizarse a otros problemas de interés biológico. En este caso en particular se pudo reproducir algunos de los nuevos agregados que se habían observado en estas circunstancias. Además, se observó cómo la segregación de lípidos podía asociarse a un aumento local de la densidad de

proteína, lo que puede favorecer la agregación en casos donde la densidad de proteínas sea baja.

En general, el trabajo presentado nos ha ayudado a profundizar en el conocimiento de FtsZ, especialmente en relación al parámetro de torsión, y se ha explorado la importancia de las condiciones de anclaje a la superficie, un aspecto que tendrá no menos relevancia en condiciones biológicas. Por supuesto aún existen aspectos que escapan al poder predictivo de los modelos tal como se han descrito en esta memoria. Por ejemplo, queda fuera del modelo la explicación de agregados multicapa, ya que no pueden ser correctamente descritos con un modelo de dos dimensiones. También se podría incluir la dinámica de hidrólisis en el modelo de red fina, que corregiría una parte importante de los problemas descritos en el capítulo 4 de esta tesis. Sin embargo, es importante recordar la filosofía descrita en la introducción, de trabajo a través de la simplificación. Introducir complejidad y realismo en este tipo de aproximaciones no aportará necesariamente más información y de mayor utilidad, acaso lo contrario. Resulta pues importante no olvidar este aspecto para saber encontrar un equilibrio, y complementar este tipo de investigación con otras aproximaciones igualmente interesantes, como el enfoque experimental o el estudio de las moléculas a un nivel más detallado, como puede ofrecer la dinámica molecular.

Bibliography

[1] Oliva MA, Cordell SC, and Löwe J. Structural insights into FtsZ protofilament formation. Nat Struct Mol Biol. 2004; 11(12): 1243–50. DOI: 10.2210/pdb1w59/pdb

[2] Bernander R. Archaea and the cell cycle. Molecular Microbiology. 1998; 29: 955–961. DOI: 10.1046/j.1365-2958.1998.00956.x

[3] Erickson H. J Cell Biol. 2000 March 20; 148(6): 1103–1106

[4] Osteryoung KW, Stokes KD, Rutherford SM, Percival AL, and Lee WY. Chloroplast division in higher plants requires members of two functionally divergent gene families with homology to bacterial ftsZ. Plant Cell. 1998; 10: 1991–2004

[5] Beech PL, Nheu T, Schultz T, Herbert S, Lithgow T, Gilson PR, and McFadden GI. Mitochondrial FtsZ in a chromophyte alga. Science. 2000; 287: 1276–1279

[6] Erickson H. Evolution of the cytoskeleton. BioEssays. 2007; 29(7): 668–77. DOI: 10.1002/bies.20601

[7] Mingorance J, Rivas G, Vélez M, Gómez-Puertas P, and Vicente M. Strong FtsZ is with the force: mechanisms to constrict bacteria. Trends in Microbiology. 2010; 18: 348–356. DOI: 10.1016/j.tim.2010.06.001

[8] Pichoff S, and Lutkenhaus J. Unique and overlapping roles for ZipA and FtsA in septal ring assembly in *Escherichia coli*. EMBO J. 2002; 21: 685– 693

[9] Pichoff S, and Lutkenhaus J. Tethering the Z ring to the membrane through a conserved membrane targeting sequence in FtsA. Mol Microbiol. 2005; 55: 1722–1734

[10] Ohashi T, Hale CA, de Boer PA, and Erickson HP. Structural evidence that the P/Q domain of ZipA is an unstructured, flexible tether between

the membrane and the C-terminal FtsZ-binding domain. J Bacteriol. 2002; 184: 4313–4315

[11] Loose M, Fischer-Friedrich E, Ries J, Kruse K, and Schwille P. Spatial regulators for bacterial cell division self-organize into surface waves in vitro. Science. 2008; 320, 5877: 789-792 DOI: 10.1126/science.1154413

[12] Bisicchia P, Arumugam S, Schwille P, and Sherratt D. MinC, MinD, and MinE drive counter-oscillation of early-cell-dvision proteins prior to *Escherichia coli* septum formation. mBio. 2013; 4(6): e00856-13. DOI: 10.1128/mBio.0085613

[13] Söderström B, Skoog K, Blom H, Weiss DS, von Heijne G, and Daley DO. Disassembly of the divisome in *Escherichia coli*: evidence that FtsZ dissociates before compartmentalization. Molecular microbiology. 2014; 92(1): 1–9. DOI: 0.1111/mmi.12534

[14] Vicente M, and Rico A. The order of the ring: assembly of *Escherichia coli* cell division components. Molecular Microbiology. 2006; 61(1): 5–8

[15] Osawa M, and Erickson HP. FtsZ from divergent foreign bacteria can function for cell division in *Escherichia coli*. J. Bacteriol. 2006; 188: 7132–7140

[16] Osawa M, Anderson DE, and Erickson HP. Curved FtsZ protofilaments generate bending forces on liposome membranes. EMBO J. 2009; 28: 3476–3484

[17] Hsin J, Gopinathan A, and Huang KC. Nucleotide-dependent conformations of FtsZ dimers and force generation observed through molecular dynamics simulations. PNAS. 2012; 109: 9432-9437

[18] Li Y, Hsin J, Cheng Y, Shang W, Huang KC, Wang H, and Ye S. FtsZ protofilaments use a hinge-opening mechanism for constrictive force generation. Science. 2013; 341, 392. DOI: 10.1126/science.1239248

[19] Mukherjee A, Saez C, and Lutkenhaus J. Assembly of an FtsZ mutant deficient in GTPase activity has implications for FtsZ assembly and the role of the ZRing in cell division. Journal of Bacteriology. 2001; 7190-7197. DOI: 10.1128/JB.183.24.7190–7197.2001

[20] Bi E, and Lutkenhaus J. Isolation and characterization of ftsZ alleles that affect septal morphology. J. Bacteriol. 1992; 174: 5414–5423

[21] Osawa M, and Erickson H. Inside-out Z rings—constriction with and without GTP hydrolysis. Mol Microbiol. 2011; 81(2): 571–579. DOI: 10.1111/j.1365-2958.2011.07716.x

[22] Páez A, Mateos-Gil P, Hörger I, Mingorance J, Rivas G, Vicente M, Vélez M, and Tarazona P. Simple modeling of FtsZ polymers on flat and curved surfaces: correlation with experimental in vitro observations. PMC Biophysics. 2009; 2(8). DOI: 10.1186/1757-5036-2-8

[23] Lan G, Daniels BR, Dobrowsky TM, Wirtz D, and Sun SX. Condensation of FtsZ filaments can drive bacterial cell division. PNAS. 2009; 106: 121-126

[24] Páez A, Tarazona P, Mateos-Gil P, and Vélez M. Self-organization of curved living polymers: FtsZ protein filaments. Soft Matter. 2009; 5: 2625–2637

[25] González de Prado Salas P, Encinar M, Vélez M, and Tarazona P. FtsZ protein on bilayer membranes: Effects of specific lateral bonds. Soft Matter. 2013; 9(26): 6072-6079. DOI: 10.1039/C3SM50590A

[26] Drye T, and Cates M. J. Chem. Phys. 1992; 96: 1367

[27] Hörger I, Velasco E, Mingorance J, Rivas , Tarazona P, and Vélez M. Langevin computer simulations of FtsZ filaments and the force generating mechanism during cell division. Phys Rev E. 2008; 77, 011902

[28] Encinar M, Kralicek AV, Martos A, Krupka M, Cid S, Alonso A, Rico AI, Jiménez M, and Vélez M. Polymorphism of FtsZ filaments on lipid surfaces: role of monomer orientation. Langmuir. 2013; 29: 9436–9446. DOI: 10.1021/la401673z

[29] Chen Y, and Erickson HP. FtsZ Filament dynamics at steady state: subunit exchange with and without nucleotide hydrolysis. Biochemistry. 2009; 48: 6664–6673. DOI: 10.1021/bi8022653

[30] Andrews S, and Arkin A. A Mechanical explanation for cytoskeletal rings and helices in bacteria. Biophysical Journal. 2007; 93: 1872–1884. DOI: 10.1529/biophysj.106.102343

[31] Hörger I, Velasco E, Rivas G, Vélez M, and Tarazona P. FtsZ bacterial cytoskeletal polymers on curved surfaces: the importance of lateral interactions. Biophys J. 2008; 94(11): L81-L83. DOI: 10.1529/biophysj.107.128363

[32] Arumugam S, Chwastek G, Fischer-Friedrich E, Ehrig C, Mönch I, and Schwille P. Surface topology engineering of membranes for the mechanical investigation of the tubulin homologue FtsZ. Angew. Chem. Int. Ed. 2012; 51: 11858–11862. DOI: 10.1002/anie.201204332

[33] Hamon L, PandaD, Savarin P, JoshiV, Bernhard J, Mucher E, Mechulam A, Curmi PA, and Pastre D. Mica surface promotes the assembly of cytoskeletal proteins. Langmuir. 2009; 25: 3331–3335

[34] González de Prado Salas P, Hörger I, Martín-García F, Mendieta J, Alonso A, Encinar M, Gómez-Puertas P, Vélez M, and Tarazona P. Torsion and curvature of FtsZ filaments. Soft Matter. 2014; 10(12): 1977–1986 DOI: 10.1039/c3sm52516c

[35] Hörger I, supervisor Tarazona P. Biophysical models for bacterial FtsZ filaments. Unpublished dissertation, 2010.

[36] Martín-García F, Salvarelli E, Mendieta-Moreno JI, Vicente M, Mingorance J, Mendieta J, and Gómez-Puertas P. Molecular dynamics simulation of GTPase activity in polymers of the cell division protein FtsZ. FEBS Letters. 2012; 586: 1236–1239.

[37] Mendieta J, Rico AI, López-Viñas E, Vicente M, Mingorance J, and Gómez-Puertas P. Structural and functional model for ionic (K+/Na+) and pH dependence of GTPase activity and polymerization of FtsZ, the prokaryotic ortholog of tubulin. J. Mol. Biol. 2009; 390: 17–25. DOI: 10.1016/j.jmb.2009.05.018

[38] Lang G, Wolgemuth CW, and Sun SX. Z-ring force and cell shape during division in rod-like bacteria. PNAS. 2007; 104(41): 16110–5. DOI: 10.1073/pnas.0702925104

[39] Mingorance J, Tadros M, Vicente M, Gonzálezz JM, Rivas G, and Vélez M. Visualization of single *Escherichia coli* FtsZ filament dynamics with atomic force microscopy. J. Biol. Chem. 2005; 280: 20909–20914. DOI: 10.1074/jbc.M503059200

[40] González JM, Vélez M, Jiménez M, Alfonso C, Schuck P, Mingorance J, Vicente M, Minton AP, and Rivas G. Cooperative behavior of *Escherichia*

coli cell-division protein FtsZ assembly involves the preferential cyclization of long single-stranded fibrils. PNAS. 2005; 102: 1895–1900. DOI: 10.1073/pnas.0409517102

[41] Chen Y, and Erickson HP. Conformational changes of FtsZ reported by tryptophan mutants. Biochemistry. 2011; 50: 4675–4684. DOI: 10.1021/bi200106d

[42] Martín-Galiano AJ, Buey RM, Cabezas M, and Andreu JM. Mapping flexibility and the assembly switch of cell division protein FtsZ by computational and mutational approaches. J. Biol. Chem. 2010; 285: 22554–22565. DOI: 10.1074/jbc.M110.117127

[43] Turner DJ, Portman I, Dafforn TR, Rodger A, Roper DI, Smith CJ, and Turner MS. The mechanics of FtsZ fibers. Biophys. J. 2012; 102: 731–738. DOI: 10.1016/j.bpj.2012.01.015

[44] Gardner KAJA, Moore DA, and Erickson HP. The C-terminal linker of *Escherichia coli* FtsZ functions as an intrinsically disordered peptide. Mol. Microbiol. 2013. DOI: 10.1111/mmi.12279

[45] Szwedziak P, Wang Q, Freund SMV, and Lowe J. FtsA forms actin-like protofilaments. EMBO J. 2012; 31(10): 2249–2260. DOI: 10.1038/emboj.2012.76

[46] Mateos-Gil P, Márquez I, López-Navajas P, Jiménez M, Vicente M, Mingorance J, Rivas G, and Vélez M. FtsZ polymers bound to lipid bilayers through ZipA form dynamic two dimensional networks. Biochim. Biophys. Acta. 2012; 1818: 806–813. DOI: 10.1016/j.bbamem.2011.12.012

[47] Galli E, and Gerdes K. FtsZ-ZapA-ZapB Interactome of *Escherichia coli*. J. Bacteriol. 2012; 194: 292–302. DOI: 10.1128/JB.05821-11

[48] Hale CA, Shiomi D, Liu B, Bernhardt TG, Margolin W, Niki H, and de Boer PA. Identification of *Escherichia coli* ZapC (YcbW) as a component of the division apparatus that binds and bundles FtsZ polymers. J. Bacteriol. 2011; 193: 1393–1404. DOI: 10.1128/JB.01245-10

[49] Dajkovic A, Pichoff S, Lutkenhaus J, and Wirtz D. Cross-linking FtsZ polymers into coherent Z rings. Mol. Microbiol. 2010; 78: 651–668. DOI: 10.1111/j.1365-2958.2010.07352.x

[50] Si F, Busiek K, Margolin W, and Sun SX. Organization of FtsZ filaments in the bacterial division ring measured from polarized fluorescence microscopy. Biophys. J. 2013; 105: 1976–1986. DOI: 10.1016/j.bpj.2013.09.030

[51] Páez A, Mateos-Gil P, Hörger I, Mingorance J, Rivas G, Vicente M, Vélez M, and Tarazona P. Simple modeling of FtsZ polymers on flat and curved surfaces: correlation with experimental in vitro observations. PMC Biophys. 2009; 2(8). DOI: 10.1186/1757-5036-2-8

[52] Head BP, Patel HH, and Insel PA. Interaction of membrane/lipid rafts with the cytoskeleton: Impact on signaling and function: Membrane/lipid rafts, mediators of cytoskeletal arrangement and cell signaling. Biochimica et Biophysica Acta (BBA)-Biomembranes. 2014; 1838: 532–545. DOI: 10.1016/j.bbamem.2013.07.018

[53] Pandit SA, Vasudevan S, Chiu SW, Mashl RJ, Jakobsson E, and Scott HL. Sphingomyelin-cholesterol domains in phospholipid membranes: Atomistic simulation. Biophysical Journal. 2004; 87(2): 1092–1100. DOI: 10.1529/biophysj.104.041939

[54] Pandit SA, Jakobsson E, and Scot HL. Simulation of the early stages of nano-domain formation in mixed bilayers of sphingomyelin, cholesterol, and dioleylphosphatidylcholine. Biophysical J. 2004; 87: 3312–3322. DOI: 10.1529/biophysj.104.046078

[55] Faller R, and Marrink SJ. Simulation of domain formation in DLPC-DSPC mixed bilayers. Langmuir. 2004; 20: 7686–7693. DOI: 10.1021/la0492759

[56] Rabinovich AL, and Lyubartsev AP. Computer simulation of lipid membranes: methodology and achievements. Polymer Science Series C. 2013; 55: 162–180. DOI 10.1134/S1811238213070060

[57] Reigada R, Buceta J, Gomez J, Sagués F, and Lindenberg K. Phase separation in three-component lipid membranes: From Monte Carlo simulations to Ginzburg-Landau equations. J. Chem. Phys. 2008; 128(2): 025102. DOI: 10.1063/1.2817333

[58] Honerkamp-Smith AR, Cicuta P, Collins MD, Veatch SL, den Nijs M, Schick M, and Keller SL. Line tensions, correlation lengths, and critical exponents

in lipid membranes near critical points. Biophysical J. 2008; 95: 236–246. DOI: 10.1529/biophysj.107.128421

[59] Gómez J, Sagués F, and Reigada R. Nonequilibrium patterns in phase-separating ternary membranes. Phys. Rev. E. 2009; 80: 011920.

[60] Fan J, Sammalkorpi M, and Haataja M. Lipid microdomains: structural correlations, fluctuations, and formation mechanisms. Phys. Rev. Lett. 2010; 104: 118101

[61] Fan J, Sammalkorpi M, and Haataja M. Domain formation in the plasma membrane: Roles of nonequilibrium lipid transport and membrane proteins. Phys. Rev. Lett. 2008; 100: 178102

[62] Ehrig J, Petrov EP, and Schwille P. Near-critical fluctuations and cytoskeleton-assisted phase separation lead to subdiffusion in cell membranes. Biophysical J. 2011; 100: 80–89. DOI: 10.1016/j.bpj.2010.11.002

[63] Witkowski T, Backofen R, and Voigt Axel. The influence of membrane bound proteins on phase separation and coarsening in cell membranes. Phys. Chem. Chem. Phys. 2012; 14: 14509–14515. DOI: 10.1039/c2cp41274h

[64] Guo L, Smith-Dupont KB, and Gai F. Diffusion as a probe of peptide-induced membrane domain formation. Biochemistry. 2011; 50: 2291–2297. DOI: 10.1021/bi102068j

[65] Lingwood D, and Simons K. Lipid rafts as a membrane-organizing principle. Science. 2010; 327(5961): 46–50. DOI: 10.1126/science.1174621

[66] Yethiraj A, and Weisshaar JC. Why are lipid rafts not observed in vivo? Biophysical J. 2007; 93(9): 3113–3119.

[67] Matsumoto K, Kusaka J, Nishibori A, and Hara H. Lipid domains in bacterial membranes. Mol Microbiol. 2006; 61(5): 1110–1117.

[68] Simons K, and Sampaio JL. Membrane organization and lipid rafts. Cold Spring Harbor-Perspectives in Biology. 2011; 3(10). DOI: 10.1101/cshperspect.a004697

[69] López-Montero I, Arriaga LR, Monroy F, RivasG, Tarazona P, and Vélez M. High fluidity and soft elasticity of the inner membrane of Escherichia coli

revealed by the surface rheology of model Langmuir monolayers. Langmuir. 2008; 24(8): 4065–4076. DOI: 10.1021/la703350s

[70] López-Montero I, Mateos-Gil P, Sferrazza M, Navajas PL, Rivas G, Vélez M, and Monroy F. Active membrane viscoelasticity by the bacterial FtsZ division protein. Langmuir. 2012; 28(10): 4744–4753. DOI: 10.1021/la204742b

[71] González de Prado Salas P, Encinar M, Alonso Á, Vélez M, and Tarazona P. Modeling the interplay between protein and lipid aggregation in supported membranes. Chemistry and Physics of Lipids: Special Issue: Membrane Mechanics. 2014. DOI: 10.1016/j.chemphyslip.2014.06.006

[72] Mateos-Gil P, Páez A, Hörger I, Rivas G, Vicente M, Tarazona P, and Vélez M. Depolymerization dynamics of individual filaments of bacterial cytoskeletal protein FtsZ. PNAS. 2012; 109(21): 8133–8138. DOI: 10.1073/pnas.1204844109

[73] Erickson HP. Modeling the physics of FtsZ assembly and force generation. PNAS. 2009; 106(23): 9238–9243. DOI: 10.1073/pnas.0902258106

[74] Mileykovskaya E, and Dowhan W. Role of membrane lipids in bacterial division-site selection. Current Opinion in Microbiology. 2005; 8(2): 135–142. DOI: 10.1016/j.mib.2005.02.012

[75] Matsumoto K, Kusaka J, Nishibori A, and Hara H. Lipid domains in bacterial membranes. Molecular Microbiology. 2006; 61(5): 1110–1117. DOI: 10.1111/j.1365-2958.2006.05317.x

[76] Margolin W. FtsZ and the division of prokaryotic cells and organelles. Nature Reviews Molecular Cell Biology. 2005; 6: 862–871. DOI: 10.1038/nrm1745